SEARCH FOR GRAVITATIONAL WAVES FROM MAGNETARS DURING ADVANCED LIGO'S SECOND OBSERVING RUN

by

PAUL SCHALE

A DISSERTATION

Presented to the Department of Physics
and the Graduate School of the University of Oregon
in partial fulfillment of the requirements
for the degree of
Doctor of Philosophy

June 2019

DISSERTATION APPROVAL PAGE

Student: Paul Schale

Title: Search for Gravitational Waves from Magnetars During Advanced LIGO's Second Observing Run

This dissertation has been accepted and approved in partial fulfillment of the requirements for the Doctor of Philosophy degree in the Department of Physics by:

James Brau	Chair
Ray Frey	Advisor
James Imamura	Core Member
Michael Kellman	Institutional Representative

and

Janet Woodruff-Borden	Vice Provost and Dean of the Graduate School

Original approval signatures are on file with the University of Oregon Graduate School.

Degree awarded June 2019

DISSERTATION ABSTRACT

Paul Schale

Doctor of Philosophy

Department of Physics

June 2019

Title: Search for Gravitational Waves from Magnetars During Advanced LIGO's Second Observing Run

We explore magnetar activity as a source for gravitational waves, and present the results of a search for short and intermediate-duration gravitational-wave signals from four magnetar bursts in Advanced LIGO's second observing run. We find no evidence of a signal and set upper limits on the root sum squared of the total dimensionless strain (h_{rss}) from incoming intermediate-duration gravitational waves ranging from 1.1×10^{-22} at 150 Hz to 4.4×10^{-22} at 1550 Hz at 50% detection efficiency. From the known distance to the magnetar SGR 1806-20 (8.7 kpc) we can place upper bounds on the isotropic gravitational wave energy of 3.4×10^{44}erg at 150 Hz assuming optimal orientation. This represents an improvement of about a factor of 100 in energy sensitivity from the previous search for such signals, conducted during Initial LIGO's sixth science run. The short duration search yielded upper limits of 2.1×10^{44} erg for short white noise bursts, and 2.3×10^{47} erg for 100 ms long ringdowns at 1500 Hz, both at 50% detection efficiency. We also analyze GW170817, the first detection of gravitational waves from a binary neutron

star system, and search for a signal following the merger with a novel semi-modeled approach using principle component analysis.

This dissertation contained previously published co-authored material.

CURRICULUM VITAE

NAME OF AUTHOR: Paul Schale

GRADUATE AND UNDERGRADUATE SCHOOLS ATTENDED:

University of Oregon, Eugene, OR
Seattle Pacific University, Seattle, WA

DEGREES AWARDED:

Doctor of Philosophy, Physics, 2019, University of Oregon
Bachelor of Science, Physics, 2013, Seattle Pacific University
Bachelor of Science, Applied Mathematics, 2013, Seattle Pacific University

PUBLICATIONS:

B. P. Abbott et al. Search for transient gravitational-wave signals associated with magnetar bursts during Advanced LIGO's second observing run. *The Astrophysical Journal*, 874(2):163, April 2019.

Cabero, Miriam; Lundgren, Andrew; Nitz, Alex H.; Dent, Thomas; Barker, David; Goetz, Evan; Kissel, Jeff S.; Nuttall, Laura K.; Schale, Paul; Schofield, Robert; Davis, Derek. Blip glitches in Advanced LIGO data. *arXiv e-prints* arXiv:1901.05093, Jan 2019.

Quitzow-James, R., Brau, J., Clark, J., Coughlin, M, Coughlin, S., Frey, R., Schale, P. Talukder, D. & Thrane, E. Exploring a search for long-duration transient gravitational waves associated with magnetar bursts. *Classical and Quantum Gravity*, 34(16):164002, 2017.

Abbott, B. P. et al. Observation of gravitational waves from a binary black hole merger. *Physical Review Letters*, 116:061102, Feb 2016.

Abbott, B. P. et al. GW170817: Observation of gravitational waves from a binary neutron star inspiral. *Physical Review Letters*, 119:161101, Oct 2017.

ACKNOWLEDGEMENTS

This work would not have been possible without generous support from many people, including Professors Raymond Frey, Robert Schofield, and James Brau. I also gratefully acknowledge other collaborators within the University of Oregon and the broader LIGO collaboration, including Jordan Palamos, Vincent Roma, Ryan Quitzow-James, Sudarshan Karki, Michael Coughlin, Scott Coughlin, and James Clark. Finally, I thank my wife Rachael for her patience through this long process, and my parents for their encouragement from the beginning.

TABLE OF CONTENTS

Chapter Page

LIST OF FIGURES

Figure Page

LIST OF TABLES

Table Page

CHAPTER I

INTRODUCTION

In 1610, the Italian astronomer Galileo Galilei pointed his newly-made telescope to the sky and changed the world. The telescope was a revolutionary tool, immediately leading to the discovery of Jovian moons and later countless celestial objects. Later breakthroughs in telescope technology, like the radio telescope, opened up new frontiers in physics and allowed for observations that had not been possible. From radio pulsars to the cosmic microwave background, these phenomena have been critical to our understanding of how the universe works.

Gravitational waves (GWs) first entered scientific consciousness shortly after Einstein published his Theory of General Relativity[1]. Due to the difficulty in detecting the very faint effects of GWs, they remained a theoretical prediction until 1982. That year, Taylor and Weisberg presented indirect evidence of the emission of GWs: a binary neutron star system (PSR 1913+16), discovered by Russell Hulse and Joseph Taylor in 1974, was slowly losing energy at precisely the rate predicted by Einstein [3]. But direct detection remained out of reach.

The first attempts at directly observing GWs were done with resonant bar detectors called Weber bars (named for Joseph Weber, the pioneer of the technique) [4]. When a GW whose frequency matches the resonant frequency of the bar passes through, the bar will vibrate. If the GW is strong enough, the vibrations can be measured, allowing detection of GWs. Though Weber himself claimed to

[1]This discovery was not without complication. After Einstein had convinced the broader scientific community of the existence of GWs, he began to doubt their existence and attempted to publish a paper with this conclusion. This resulted in his first experience with American peer review, and he was eventually convinced that he was in error and never published his attempted refutation.

have made a detection, scientists who attempted to replicate the experiment found no evidence for any signal (see, e.g., [5]).

In 2015, the Laser Interferometer Gravitational-wave Observatory (LIGO) [6, 7] opened a new era of astronomy with the first detection of gravitational waves, enabling the use of gravity itself to study the cosmos. For the first time, the merger of black holes was directly observed. Not only did this directly confirm the existence of gravitational waves, a key part of Einstein's theory of gravity, it allowed precision measurements of the dynamics of strong gravitational fields. In cosmology, direct observation of binary black hole mergers allow population and spin measurements, constraining models of galaxy and star formation.

This was followed by the detection of several more binary mergers, including a binary neutron star (BNS) merger in 2017. This signal was accompanied by a burst of γ-rays and a long-lived multi-band electromagnetic afterglow [8]. A wealth of information can be found by studying this light. For example, it shows that many heavy elements were produced during the merger. These elements cannot be produced in large quantities by supernovae, and so their natural abundances had been ascribed BNS mergers. This event, named GW170817, confirmed that theory.

The observation of compact binaries is only the beginning for the new field of gravitational wave astronomy. Countless processes are theorized to produce significant GW emission. Some sources, like rotating neutron stars, are known to produce GWs, but the amount is uncertain. Others, like cosmic strings (topological defects left over from the early universe) are theoretical objects whose existence is uncertain.

GW astronomy sets itself apart from electromagnetic astronomy in the difficulty of detection. For reasons that are not currently, and may never be,

known the constants of nature dictate that waves in the electromagnetic field are easy to generate and detect while waves in spacetime are not. Even after twenty-five years of work, only the brightest sources of gravitational radiation have become detectable, and this has required achieving a level of sensitivity considered unthinkable before this project began. Countless advances, from the extremely stable laser to the advanced seismic isolation system and sophisticated software analysis pipelines, were required to achieve this result. And the process is ongoing, with hundreds of scientists currently working to boost the sensitivity of the detectors in preparation for the third observing run of Advanced LIGO.

Since GW signals are so weak, simply proving the existence of a signal is a difficult task, and the unique characteristics of each potential source dictate the ideal way for a search to be conducted. Matched filtering works well to detect well-modeled signals (like binary black hole mergers), but cannot be used when there is significant uncertainty in the source's dynamics (such as supernovae). Sources vary widely in frequency and timescale, with each signal presenting unique challenges. Short signals may be easily mistaken for a class of detector noise artifacts known as glitches, and so require careful data quality control. Longer signals require more computational resources, and must be careful of narrowband 'lines' in the detector noise spectrum.

Once detected, GWs enable measurements that cannot be made with electromagnetic observations. Any astronomical body that emits detectable GWs must be extremely compact, making it appear as a single point to EM observers. But since GWs are produced by oscillations in the distribution of mass and energy, those distributions are encoded in the GW signal. While these distributions are known for black holes, the makeup and structure of neutron stars is still uncertain.

The burst of GWs from the merger of a BNS system is extremely energetic, visible by LIGO from distances up to and exceeding 50 Mpc. Neutron stars are expected to radiate GWs through other mechanisms as well. Since these mechanisms are predicted to produce much weaker GWs, nearer sources are required.

This dissertation is primarily concerned with the detection of GWs from magnetars, neutron stars thought to have an extremely strong magnetic field, during Advanced LIGO's second observing run. To that end, Chapter II contains an overview of Einstein's Theory of General Relativity, including the propagation and generation of GWs. Chapter III is concerned with the interaction of those GWs with matter, the theory of their detection, and the construction of the LIGO instruments. Chapter IV lays out the current understanding of magnetars, both as astronomical objects and potential emitters of GWs. Chapter V outlines the method for the search for GWs from magnetars during LIGO's second observing run, the limits of the sensitivity for that search, and the implications for astronomy. In Chapter VI, we revisit the first binary neutron star merger, GW170817, using the methods of the previous chapter, and discuss the prospects of, and a search for, signals following that merger. Finally, Chapter VII contains some concluding remarks.

Previously published co-authored material is found in chapters III and V. Previously unpublished co-authored material is found in Chapter VI.

CHAPTER II

MATHEMATICAL BACKGROUND

Building on Special Relativity, Einstein added one more big idea: the equivalence principle. Noting that gravitational mass was identical to inertial mass, he reasoned that acceleration is indistinguishable from the pull of a gravitational field (neglecting tidal effects). This principle shows the way to unify a theory of gravitation with Special Relativity: we replace the inertial frames of Special Relativity with freely falling frames. However, we quickly run into mathematical trouble, as these reference frames can now accelerate with respect to each other. Luckily for Einstein, the mathematics needed to deal with this, differential geometry, had been invented the previous century. Below is an overview of the concepts needed to understand the basics of General Relativity, with an eye to gravitational waves (GWs).

2.1. Overview of Differential Geometry

2.1.1. Vectors, Tensors, and One-Forms

A vector is often thought of a set of numbers: a velocity vector is defined by specifying the components v_x, v_y, and v_z. This notion of a vector is wholly dependent on a coordinate system, and a change of coordinate system can be accomplished by defining a new vector $v' = (v'_x, v'_y, v'_z)$. However, these are really the same vector expressed in different coordinate systems. So instead, we can identify the vector as $\vec{\mathbf{v}}$ whose components are only defined once we have specified a coordinate system. We can then write $\vec{\mathbf{v}} = v^a \mathbf{e}_a$, where we sum over all values of a,

and $\{\vec{\mathbf{e}}_a\}$ is the set of basis vectors in our chosen coordinate system. Note that, for a particular choice of a, v^a is a number, while $\vec{\mathbf{e}}_a$ is a (unit) vector.

It is easy to see how to find the components in a different coordinate system: $\vec{\mathbf{v}} = v^a\vec{\mathbf{e}}_a = v'^a\vec{\mathbf{e}}'_a$. Thus we can see that the old components v^a and the new components v'^a are related by a transformation matrix: $v'^a = \Lambda^a{}_b v^b$.

Vectors now have a counterpart, called covectors or one-forms. Covectors are written with a tilde over them rather than an arrow, the basis covectors are $\widetilde{\boldsymbol{\omega}}^a$ (note the raised index for noting which basis covector), their components are written with a lowered index, and they transform with the inverse transpose of the vectors' transformation matrix: $w'_b = \big((\Lambda^{-1})^T\big)_b{}^a w_a$.y

With this construction, we can see that the product $v^a w_a$ is invariant under a change of coordinate system:

$$\begin{aligned} v'^a w'_a &= \Lambda^a{}_b v^b \big((\Lambda^{-1})^T\big)_a{}^c w_c \\ &= \big(\Lambda^{-1}\big)^c{}_a \Lambda^a{}_b v^b w_c \\ &= \delta^c_b v^b w_c \\ &= v^a w_a \end{aligned} \tag{2.1}$$

Thus covectors can be thought of as functions, invariant of coordinate transformations, that map vectors into real numbers. Similarly, vectors can be thought of a functions on covectors. We can combine vectors and covectors into an object called a tensor, for example $\mathbf{T} = \vec{\mathbf{x}} \otimes \widetilde{\mathbf{w}}$ ($\otimes$ is called the tensor product). Here, $\mathbf{T}$ is a tensor that takes a covector and a vector and returns a number. Writing this in index notation ($T^a{}_b = x^a w_b$) we can clearly see how the tensor acts

on the inputs: $\vec{\mathbf{x}}$ acts on the input covector, $\widetilde{\mathbf{w}}$ on the input vector, and the result is multiplied together.

The notation in this dissertation will be as follows: numbers, whether they be a single variable x or a component of a vector, covector, or tensor x^μ, w_μ, or $T_{\mu\nu}$, respectively, will be written in normal typeface. Vectors will be bold with an arrow, $\vec{\mathbf{x}}$, (three vectors will not be bold) covectors bold with a tilde $\widetilde{\mathbf{w}}$, and tensors will be bold with no diacritic, $\mathbf{T}$. With Einstein summation notation, any time the same letter is used twice in a term (e.g. $x^\alpha w_\alpha$), it is being summed over. When that letter is Greek, it sums over four dimensions; when Latin, over only three (excluding time).

2.1.2. Manifolds, Derivatives, and Curvature

A manifold is a set a points with a sense of points being near each other in a way that looks like ordinary Euclidean space locally. Globally, the space can be curved in ways that violate Euclid's axioms, and connected in unusual ways (such as the surface of a sphere or torus). On top of the structure of a manifold, we can impose a definition of infinitesimal distance between nearby points with an object called the metric, a tensor field denoted $\boldsymbol{g}$, which may vary on the manifold. At every point $p \in \mathcal{M}$, there is a metric tensor $\boldsymbol{g}(p)$ associated with that point. We can then use the metric to measure any vector $\mathbf{x}$ with $L^2 = g_{\mu\nu}x^\mu x^\nu$.

The metric also defines the correspondence between vectors and covectors. Thus, the metric $g_{\mu\nu}$ and its inverse $g^{\mu\nu}$ can be used to lower and raise the index, respectively. We can write the previous equation as $L^2 = g_{\mu\nu}x^\mu x^\nu = x_\nu x^\nu$, where x_ν are the components of the covector dual to $\vec{\mathbf{x}}$. In flat Euclidean space, the metric

is simply the identity matrix, so vectors and covectors are identical and these equations are equivalent to the Pythagorean Theorem.

Note that a manifold is not required to have a metric (a Newtonian spacetime manifold is one such example[1]), but such manifolds are mostly in the interest of mathematicians. Properties of the metric in general relativity will be discussed in the next section.

Since manifolds can have complicated global structure, it is not necessarily possible to find a single mapping that takes the entire manifold into Euclidean space. For example, no two-dimensional map can accurately depict the surface of the Earth. For the purposes of general relativity, this is mostly irrelevant outside of cosmology (regarding the global topology of the universe) and black holes (due to the singularities, both as a mathematical artifact in some coordinate systems and the real singularity at the center). Mathematically, the compatibility of different maps over the same patch gives rise to the concepts of differentiable and smooth manifolds. The manifolds of general relativity are smooth manifolds, which are differentiable in the respects that physicists want.

Manifold curvature is apparent in a number of ways, though to discuss this we must let go of some assumptions used in flat space. First, vectors no longer point from one location to another; associated with each point we define a vector space called the tangent vector space. A vector exists in a tangent vector space associated with a specific point on the manifold. Since we can only compare members of the same space, vectors can only be compared if they are defined at the same location.

[1]This is because an invariant spacetime distance cannot be defined. An observer traveling from one event to another would see no spatial distance between the events, only a time difference. A different observer would observe the same time difference, but may also see a spatial displacement. Treated without time, Newtonian space is simply Euclidean 3-space, which is a manifold equipped with a flat metric.

A curve can be measured by integrating the infinitesimal length of its tangent vectors along the the curve. Next, we allow the basis vectors to vary along the manifold. Now consider the derivative operator. Previously, for some vector field $\vec{\mathbf{x}}$, the derivative taken along the μth direction would simply be $\nabla_\mu \vec{\mathbf{x}} = \vec{\mathbf{e}}_\rho \partial_\mu x^\rho$. Just as in three dimensions, this derivative can be easily converted to a directional derivative. In three dimensions, we have $(\vec{y} \cdot \vec{\nabla})\vec{x}$. In four dimensions with Einstein summation notation, this can be written as $y^\mu \nabla_\mu x^\nu$. However, in curved space the unit vectors change, so the derivative can be expanded:

$$\begin{aligned} \nabla_\mu \vec{\mathbf{x}} =& \nabla_\mu \big(x^\rho \vec{\mathbf{e}}_\rho \big) \\ =& \vec{\mathbf{e}}_\rho \partial_\mu x^\rho + x^\rho \nabla_\mu \vec{\mathbf{e}}_\rho \end{aligned} \tag{2.2}$$

By multiplying by $\widetilde{\boldsymbol{\omega}}^\nu$ and applying some index gymnastics, we can find the component form, where the covariant derivative is denoted by a semicolon, and the partial derivative by a comma:

$$\begin{aligned} x^\nu{}_{;\mu} =& \widetilde{\boldsymbol{\omega}}^\nu \vec{\mathbf{e}}_\rho x^\rho{}_{,\mu} + \widetilde{\boldsymbol{\omega}}^\nu x^\rho \nabla_\mu \vec{\mathbf{e}}_\rho \\ =& \delta^\nu{}_\rho x^\rho{}_{,\mu} + \big(\widetilde{\boldsymbol{\omega}}^\nu \nabla_\mu \vec{\mathbf{e}}_\rho \big) x^\rho \\ =& x^\nu{}_{,\mu} + \Gamma^\nu{}_{\rho\mu} x^\rho \end{aligned} \tag{2.3}$$

where $\Gamma^\nu{}_{\rho\mu} = \widetilde{\boldsymbol{\omega}}^\nu \nabla_\mu \mathbf{e}_\rho$, and are called Christoffel symbols, and their presence in the equation accounts for the changes in the basis vectors across the manifold. This can be visualized with the surface of the earth, taking the coordinates to be latitude and longitude: stand at a point north of the equator, face west, and walk in a straight line. Eventually, you will find that you are no longer traveling due

west, but south of west; the unit vector indicating which direction "west" is has changed along your path.

Following the same reasoning, we can see that the covariant derivative of a covector will be similar:

$$w_{\nu;\mu} = \partial_\mu w_\nu - \Gamma^\rho{}_{\nu\mu} w_\rho \tag{2.4}$$

And this is easily generalized to the covariant derivative of tensors: for each vector (up) index, we add the proper Christoffel; for each covector (down) index, we subtract the proper Christoffel. For example:

$$T^{\mu\nu}{}_{\sigma;\rho} = T^{\mu\nu}{}_{\sigma,\rho} + \Gamma^\mu{}_{\gamma\rho} T^{\gamma\nu}{}_\sigma + \Gamma^\nu{}_{\gamma\rho} T^{\mu\gamma}{}_\sigma - \Gamma^\gamma{}_{\sigma\rho} T^{\mu\nu}{}_\gamma \tag{2.5}$$

In this dissertation, the semicolon will be used for this covariant derivative, and a comma for the ordinary partial derivative.

Though the metric does not explicitly appear in the definition, the Christoffel symbols are in fact derived from the metric: recall that the metric defines correspondence between vectors and one-forms. The set of basis vectors (or the basis one-forms) may be chosen arbitrarily (as long as they span the whole space), but the metric will then define the corresponding basis one-forms (or basis vectors).

With vectors only defined locally, we have lost the usual sense of how to define a straight line. However, with this covariant derivative, we can define straight lines using the idea of parallel transport. First, let the curve S, parameterized by λ, be defined as a mapping from $\mathbb{R}$ into $\mathcal{M}$, which is then mapped into $\mathbb{R}^n$ by some mapping ψ. Thus, at any particular value of λ, we have a corresponding $p(\lambda) \in \mathcal{M}$, and $\xi^\mu(\lambda) \in \mathbb{R}^n$. The tangent vector to the curve is then

$u^\mu = \frac{d\xi^\mu}{d\lambda}$. Now suppose there is another vector defined at every point along this curve, y^μ. This vector is said to be parallel transported along the curve if and only if it does not change as you travel along the curve:

$$u^\nu \nabla_\nu y^\mu = 0 \tag{2.6}$$

In words, the left side of the equation asks how the vector $\vec{\mathbf{y}}$ changes as one moves in the direction of the vector $\vec{\mathbf{u}}$ – the directional derivative along the curve. This concept can be used to define a straight line (remember, we no longer have the notion of a vector traveling from one point to another). This is done by demanding that the tangent vector parallel transport itself:

$$u^\nu \nabla_\nu u^\mu = 0 \tag{2.7}$$

By equation 2.3, we can expand this expression:

$$\begin{aligned} 0 =& u^\nu \partial_\nu u^\mu + u^\nu \Gamma^\mu{}_{\nu\rho} u^\rho \\ =& \frac{du}{d\lambda} + \Gamma^\mu{}_{\nu\rho} u^\rho u^\nu \\ =& \frac{d^2\xi^\mu}{d\lambda^2} + \Gamma^\mu{}_{\nu\rho} \frac{d\xi^\nu}{d\lambda} \frac{d\xi^\rho}{d\lambda} \end{aligned} \tag{2.8}$$

The result is four second order differential equations. Note that, in flat space, all Christoffel symbols are zero and the equations reduce to $\frac{d^2\xi^\mu}{d\lambda^2} = 0$, or straight lines in the Euclidean sense.

Another important property of vectors is commutativity, $u^\mu \nabla_\mu y^\nu = y^\mu \nabla_\mu u^\nu$.[2] This property is so named because a vector defines a directional derivative; thus the action of u^μ on y^ν is $u^\mu \nabla_\mu y^\nu$.

To find an explicit formula for the Christoffel symbols in terms of the metric, we demand that vectors not change length as they are parallel transported along a curve. Thus:

$$\begin{aligned} 0 =& u^\alpha \nabla_\alpha \big(g_{\mu\nu} x^\mu x^\nu\big) \\ =& u^\alpha x^\mu x^\nu \nabla_\alpha g_{\mu\nu} + 2u^\alpha x^\mu g_{\mu\nu} \nabla_\alpha x^\nu \end{aligned} \tag{2.9}$$

Because the vector is being parallel transported, $u^\alpha \nabla_\alpha x^\nu = 0$. Since the equation is true for all curves, we must have $\nabla_\alpha g_{\mu\nu} = 0$. This can be expanded:

$$\begin{aligned} 0 =& \nabla_\alpha g_{\mu\nu} \\ =& g_{\mu\nu,\alpha} + \Gamma^\sigma{}_{\mu\alpha} g_{\nu\sigma} + \Gamma^\sigma{}_{\nu\alpha} g_{\mu\sigma} \end{aligned} \tag{2.10}$$

After an algebra trick, we have:

$$\Gamma^\sigma{}_{\mu\nu} = g^{\sigma\alpha}\big(g_{\mu\nu,\alpha} + g_{\mu\alpha,\nu} - g_{\alpha\nu,\mu}\big) \tag{2.11}$$

To connect this to physics, we go back to Newton's first law, which requires that an object that experiences no forces cannot change its motion. Relativity demands the same, but in four dimensions. Since time is already included in the definition of the path followed, we no longer have to specify anything about the

[2]This property only holds in a coordinate basis, where the unit vectors can be expressed as the partial derivative of a coordinate, $\vec{\mathbf{e}}_\mu = \partial_\mu$. All bases in this dissertation will be coordinate bases.

velocity. Instead, it suffices to insist that objects in free-fall follow straight lines: the geodesics described above. And, as we shall see later in this chapter, the concept of "gravity" that Newton studied is simply a consequence of the curvature of spacetime. The path of a free-falling object, which looks like a parabola in three dimensions, is actually a straight line on the four dimensional spacetime manifold.

2.2. Minkowski Spacetime

Before discussing how this curvature manifests itself in general relativity, we must take a step back and discuss how flat space operates. Newtonian mechanics held that space and time were separate, and thus the universe could be thought of as a set of manifolds with three spacial dimensions, with the manifolds labeled by time. Partly due to the apparent incompatibility of Maxwell's electromagnetism with Galilean relativity applied to such a spacial structure, Einstein was led to unify the time and space dimension into a single manifold. To preserve the invariance of electromagnetic laws, and particularly the speed of light, upon transformation to any inertial reference frame, the manifold is equipped with a metric of signature $(-1, 1, 1, 1)$ (this is a free choice of sign; some literature flips all of the signs). In the absence of any curvature, this is called Minkowski Spacetime. Setting the speed of light set to 1, the metric for Minkowski Spacetime can be represented with the matrix:

$$\eta_{\mu\nu} = \begin{bmatrix} -1 & 0 & 0 & 0 \\ 0 & 1 & 0 & 0 \\ 0 & 0 & 1 & 0 \\ 0 & 0 & 0 & 1 \end{bmatrix} \tag{2.12}$$

We can see that this metric recovers the familiar spacetime interval from special relativity:

$$\eta_{\mu\nu}x^\mu x^\nu = -(x^0)^2 + (x^1)^2 + (x^2)^2 + (x^3)^2 \tag{2.13}$$

The laws of electromagnetism are much easier to express in 4 dimensions. For example, the conservation of charge in three dimensions is $\vec{\nabla} \cdot \vec{J} + \frac{d\rho}{dt} = 0$. In 4 dimensions, we instead use the current density as $\mathbf{J} = (\rho, J_i)$, and the equation becomes $\boldsymbol{\nabla \cdot J} = \nabla_\mu J^\mu = 0$. Likewise we define a four-potential $\mathbf{A} = (V, A_i)$. Gauge transformations are then $A_\mu \to A_\mu + \xi_{,\mu}$.

The metric of special relativity, shown above, corresponds to a flat manifold. However, the equivalence of gravitational mass and inertial mass led to the idea that gravity is not a force, but a manifestation of the geometry of the spacetime manifold. A simple explanation of the interaction is this: "Space acts on matter, telling it how to move. In turn, matter reacts back on space, telling it how to curve." [9, p. 5]

Though globally spacetime is curved, the structure of a manifold requires that it looks flat locally. Thus, it is always possible to find a coordinate system at any point p such that $g_{\mu\nu}(p) = \eta_{\mu\nu}$. It is only when we inquire about the relationship between two separated objects that the geometry of spacetime enters our calculations.

2.2.1. Riemann Curvature Tensor

As a starting point, the Christoffel symbols defined above look like a good way to quantify curvature. Unfortunately, though they look like tensors, they are not tensors because they do not transform as tensors—they identify how the partial

derivatives in a particular coordinate system differ from the covariant derivative, so they must be identified with a particular coordinate system. On the other hand, vectors, scalars, etc transform properly by definition, so any equation between such objects that involves curvature will be suitable.

We define the Riemann Curvature Tensor through its action on vectors and covectors. The following equations are equivalent:

$$\begin{aligned}(\nabla_\alpha \nabla_\beta - \nabla_\beta \nabla_\alpha) w_\gamma &= R_{\alpha\beta\gamma}{}^{\delta} w_\delta \\ (\nabla_\alpha \nabla_\beta - \nabla_\beta \nabla_\alpha) x^\gamma &= R_{\alpha\beta}{}^{\gamma}{}_{\delta} x^\delta\end{aligned} \tag{2.14}$$

At first glance, this does not seem to be a tensor at all—it's a second order differential operator, but tensors are supposed to be linear machines. Surprisingly, the action of the Riemann tensor on a covector field only depends on the value of the covector at the point being evaluated [10, p.36], and thus is a tensor. This comes from the fact that covariant derivatives, acting on scalars, are simply partial derivatives, and thus commute.[3]

One place the Riemann tensor shows up is in geodesic deviation. In the presence of curvature, the distance between initially parallel geodesics can change. This effect, which is also known as tidal acceleration, can be modeled in the following way:

Consider a family of geodesics $\mathscr{P}(\lambda, n)$, each labeled by n and parameterized by the same parameter λ, which are parallel at $\lambda = 0$. Now, consider one such geodesic and label the tangent vector u^α. Then, since it's a geodesic, we know:

[3]The proof from [10] involves multiplying a vector field by a smooth scalar field whose value is 1 at the point in question and arbitrary everywhere else. It is then shown that, after operating on the vector field with the Riemann tensor, the scalar field drops out.

$$u^\beta \nabla_\beta u^\alpha = 0 \tag{2.15}$$

We can then consider how this changes as we move to a nearby geodesic, identifying this as the covariant derivative with respect to n^γ, the vector that points in the direction of the next geodesic. This is still zero, but we can manipulate it:

$$\begin{aligned}
0 =& n^\gamma \nabla_\gamma (u^\beta \nabla_\beta u^\alpha) \\
=& (n^\gamma \nabla_\gamma u^\beta)(\nabla_\beta u^\alpha) + u^\beta n^\gamma \nabla_\gamma \nabla_\beta u^\alpha \\
=& (u^\beta \nabla_\beta n^\gamma)(\nabla_\gamma u^\alpha) + u^\beta n^\gamma \nabla_\gamma \nabla_\beta u^\alpha \\
=& u^\beta \nabla_\beta (n^\gamma \nabla_\gamma u^\alpha) - u^\beta n^\gamma \nabla_\beta \nabla_\gamma u^\alpha + u^\beta n^\gamma \nabla_\gamma \nabla_\beta u^\alpha \\
=& u^\beta \nabla_\beta (u^\gamma \nabla_\gamma n^\alpha) + R_{\gamma\beta}{}^\alpha{}_\sigma u^\sigma u^\beta n^\gamma
\end{aligned} \tag{2.16}$$

For the second line we used the product rule, commutation of vectors and relabeling of summed over indices for the third, inverse product rule for the fourth, and the definition of the Riemann tensor along with vector commutation for the last line. Now let us make sense of the first term, $u^\beta \nabla_\beta (u^\gamma \nabla_\gamma n^\alpha)$. The piece inside parenthesis asks how the separation between geodesics changes as we move along one, so we can identify this as the relative velocity of nearby geodesics. Since we then take the covariant derivative again along the geodesic, this term represents the relative acceleration of nearby geodesics. Thus, we can use the Riemann tensor to calculate geodesic deviation, an important facet of curvature.

Similarly, if a vector x^μ is parallel transported around a small square defined by the vectors u^α and v^β, the change will be given by

$$(\delta x)^\nu = R^\nu{}_{\mu\alpha\beta} x^\mu u^\alpha v^\beta \tag{2.17}$$

We can also write the Riemann tensor explicitly in terms of the Christoffel symbols [9, Equation 11.12]:

$$R^\alpha{}_{\beta\gamma\delta} = \Gamma^\alpha{}_{\beta\delta,\gamma} - \Gamma^\alpha{}_{\beta\gamma,\delta} + \Gamma^\alpha{}_{\mu\gamma}\Gamma^\mu{}_{\beta\delta} - \Gamma^\alpha{}_{\mu\delta}\Gamma^\mu{}_{\beta\gamma} \tag{2.18}$$

This form makes it apparent that the Riemann tensor is not a differential operator. This definition also allows us to prove the Bianchi identity

$$0 = R_{\rho\mu\sigma\nu;\eta} - R_{\rho\mu\sigma\eta;\nu} + R_{\rho\mu\nu\eta;\sigma} \tag{2.19}$$

We note the symmetries of the Riemann tensor

$$\begin{aligned} R_{\mu\nu\rho\sigma} &= -R_{\mu\nu\sigma\rho} \\ R_{\mu\nu\rho\sigma} &= R_{\rho\sigma\mu\nu} \\ R_{\mu\nu\rho\sigma} &= -R_{\nu\mu\rho\sigma} \end{aligned} \tag{2.20}$$

Finally, the contractions of Riemann:

$$\begin{aligned} R_{\mu\nu} &= R^\sigma{}_{\mu\sigma\nu} \\ R &= R^\mu{}_\mu = g^{\mu\nu} R_{\mu\nu} \end{aligned} \tag{2.21}$$

The first, $R_{\mu\nu}$ is called the Ricci curvature tensor, and the second, R, is the scalar curvature. Note that all other possible contractions of the Riemann tensor are either zero or equal to Ricci up to a sign.

2.3. General Relativity

The overarching goal of General Relativity is to identify gravity as the manifestation of the curvature of spacetime. In the previous section we explored what curvature means and how it becomes apparent. In this section, we will see how curvature is produced by mass and energy and how the laws of General Relativity give rise to gravitational radiation. But if we are to construct a tensor equation relating mass and energy to geometric curvature, we need a tensor that describes them.

2.3.1. Stress-Energy Tensor

The stress-energy tensor, denoted as $T^{\mu\nu}$ is a second rank tensor which, when cast into a particular coordinate system, indicate the location and movement of momentum and energy. In particular, $T^{\mu\nu}x_\nu = p^\mu$ is the four-momentum density traveling through a hypersurface perpendicular to x_ν. Examining the individual components in a particular coordinate system, we can see where the name comes from: if x_ν is timelike, then p^μ is simply the static four-momentum (or the four-momentum traveling through time). Thus we can identify T^{00} as the energy density in that coordinate system. Similarly, T^{k0} is the k component of the three-momentum density. We can then see that T^{11} will be the x-momentum density traveling in the x-direction, with the same holding for T^{22} and T^{33}. These terms are generally known as pressure. The rest of the terms, T^{jk} are called shear

or stress, and quantify the linear momentum density being carried in a different direction. For a swarm of particles, the stress-energy tensor at a point can be easily by examining the particles in a small volume around that point:

$$T^{\mu\nu} = \sum_A m_A u_A^\mu u_A^\nu \tag{2.22}$$

Here, we are summing over the particles in the small volume, were m_A is the mass of particle A, and u^μ is its four-velocity. If these particles form a perfect fluid (and thus have a well-defined density and pressure), this can be simplified:

$$T^{\mu\nu}_{\text{fluid}} = pg^{\mu\nu} + (\rho + p)u^\mu u^\nu \tag{2.23}$$

Now, u^μ is the four-velocity of the fluid (since the volume is small, this is a single value). In the rest frame in flat space, $u^0 = 1$ and $u^j = 0$, so this reduces to what we expect: mass density and pressure with no stresses or linear momentum:

$$T^{\mu\nu} = \begin{bmatrix} \rho & 0 & 0 & 0 \\ 0 & p & 0 & 0 \\ 0 & 0 & p & 0 \\ 0 & 0 & 0 & p \end{bmatrix} \tag{2.24}$$

But if we boost into a frame which is moving with respect to the fluid—for example, if $u^\mu = (\gamma, \beta\gamma, 0, 0)$:

$$T^{\mu\nu} = \begin{bmatrix} \gamma^2\rho + (\gamma^2 - 1)p & (\rho + p)\gamma^2\beta & 0 & 0 \\ (\rho + p)\gamma^2\beta & p + \gamma^2\beta^2(\rho + p) & 0 & 0 \\ 0 & 0 & p & 0 \\ 0 & 0 & 0 & p \end{bmatrix} \tag{2.25}$$

Finally, we wish to find a conservation of mass/energy expression equation. This is done the same way as conservation of charge, by insisting that the integral over a four-volume be constant. This may raise the question of why we cannot have a bit of energy enter the four-volume from outside of it and remain there; however because time is one of the four dimensions this is impossible. Just as we united the divergence of the volume current density and the time derivative of the charge density into $\nabla_\mu J^\mu = 0$, the conservative of stress-energy can be written as:

$$\nabla_\mu T^{\mu\nu} = T^{\mu\nu}{}_{\mu} = 0 \tag{2.26}$$

2.3.2. Einstein's Equations

Finally we come to the Einstein field equations, which relate the distribution of mass, energy, momentum, stresses, and pressures to the geometry of spacetime. The equations take the following form:

$$G_{\mu\nu} = 8\pi T_{\mu\nu} \tag{2.27}$$

where $G_{\mu\nu}$ is the Einstein tensor, defined as

$$G_{\mu\nu} = R_{\mu\nu} - \frac{1}{2} R g_{\mu\nu} \tag{2.28}$$

Since Einstein's equations are an axiom of the theory, there is no way to prove its truth from any other principles. However, we can justify it in several ways. First the spacetime terms are derived only from the metric. Next, it satisfies

the same conservation law as the stress-energy tensor, so, $G^{\mu\nu}{}_{;\nu} = T^{\mu\nu}{}_{;\nu} = 0$. The only first-order equation matching this constraint is $G^{\mu\nu} = aR^{\mu\nu} + bRg^{\mu\nu}$.[4]

The ratio of a to b can be found by applying the conservation law. We start with the Bianchi identity for the Riemann tensor and contract twice with the metric, finding that two of the terms reduce to the Ricci tensor, and the second to the scalar curvature R:

$$\begin{aligned} 0 =& R_{\rho\mu\sigma\nu;\eta} - R_{\rho\mu\sigma\eta;\nu} + R_{\rho\mu\nu\eta;\sigma} \\ =& R_{\mu\nu;\eta} - R_{\mu\eta;\nu} + R^{\sigma}{}_{\mu\nu\eta;\sigma} \\ =& R_{\mu\nu;}{}^{\mu} - R_{;\nu} + R^{\sigma}{}_{\nu;\sigma} \\ =& 2R_{\mu\nu;}{}^{\mu} - R_{;\nu} \end{aligned} \tag{2.29}$$

Next, we raise the ν index, use the fact that $g_{\mu\nu;\alpha} = 0$ to distribute the covariant derivative, and change by a numerical factor to match convention:

$$\begin{aligned} 0 =& 2R^{\mu\nu}{}_{;\mu} - g^{\mu\nu}R_{;\mu} \\ =& \left(R^{\mu\nu} - \frac{1}{2}g^{\mu\nu}R\right)_{;\mu} \end{aligned} \tag{2.30}$$

Thus, in order to match the conservation of mass-energy is expressed in the equation $T_{\mu\nu}{}^{;\nu} = 0$, we must have, up to a constant factor, $G^{\mu\nu} = R^{\mu\nu} - \frac{1}{2}Rg^{\mu\nu}$.

[4]One other term is allowed: a constant multiplied by the metric, $\Lambda g^{\mu\nu}$, the cosmological constant term. If it is nonzero, spacetime far from any mass will not be flat. The measured upper limit for the value of Λ is about $1 \times 10^{-43}\mathrm{m}^{-2}$ [11], small enough that it can be safely neglected for our purposes. When used, it is not included in the Einstein tensor but rather added as another term to Equation 2.27

So here we have a mathematical representation of how matter and energy (whose information is contained in $T_{\mu\nu}$) affects the geometry of spacetime. We have already seen how this geometry affects matter. So here we have a complete description of the theory of general relativity. There's one problem remaining: to simultaneously solve Einstein's equations, a set of 10 coupled nonlinear second order partial differential equations of four variables, together with the geodesic equation for each object involved, which is a second order nonlinear ordinary differential equation. Few full solutions have been found, and they have all involved a large degree of symmetry. Even the case of a binary black hole system has not been solved; only numerical simulations are possible.

The difficulty in solving Einstein's equations comes partly from the fact that the definition of coordinates is bound up in the solution. So, unlike in electromagnetism, it is not possible to calculate the field based on the distribution of mass since the distribution of mass cannot be known with knowing the field.

2.4. Linearized Theory

When curvature is small, we can use an approximation to neglect the higher order terms that make the equations so difficult to solve. We begin by writing the metric as $g_{\mu\nu} = \eta_{\mu\nu} + h_{\mu\nu}$ where $\eta_{\mu\nu}$ is the metric of flat spacetime and $h_{\mu\nu}$ is a small perturbation. We calculate the Ricci curvature tensor and scalar curvature assuming that $h_{\mu\nu}$ is small in the sense that we can discard quadratic terms. Next, define the "bar" operation, $\bar{h}_{\mu\nu} = h_{\mu\nu} - \frac{1}{2}\eta_{\mu\nu}h$. Note that then $\bar{h}_{\alpha}^{\ \alpha} = 0$. Then, since $Rg_{\mu\nu} = R\eta_{\mu\nu}$ to first order in $h_{\mu\nu}$, the Einstein tensor becomes $G_{\mu\nu} = \bar{R}_{\mu\nu}$. Using the definition of the Riemann tensor from [12]:

$$
\begin{aligned}
R_{\mu\nu} = R^{\alpha}{}_{\mu\alpha\nu} =& g^{\alpha\beta} R_{\alpha\mu\beta\nu} \\
\approx& \frac{1}{2}\eta^{\alpha\beta}\Big(h_{\alpha\nu,\mu\beta} - h_{\alpha\beta,\mu\nu} + h_{\mu\beta,\alpha\nu} - h_{\mu\nu,\alpha\beta}\Big) \\
=& \frac{1}{2}\Big(h_{\alpha\nu,\mu}{}^{\alpha} - h_{\alpha}{}^{\alpha}{}_{,\mu\nu} + h_{\mu}{}^{\alpha}{}_{,\alpha\nu} - h_{\mu\nu,\alpha}{}^{\alpha}\Big)
\end{aligned}
\tag{2.31}
$$

Then,

$$
\begin{aligned}
G_{\mu\nu} =& \bar{R}_{\mu\nu} \\
=& \frac{1}{2}\Big(\bar{h}_{\alpha\nu,\mu}{}^{\alpha} - \bar{h}_{,\mu\nu} + \bar{h}_{\mu}{}^{\alpha}{}_{,\alpha\nu} - \bar{h}_{\mu\nu,\alpha}{}^{\alpha}\Big) \\
=& \frac{1}{2}\Big(\bar{h}_{\alpha\nu,\mu}{}^{\alpha} + \bar{h}_{\mu}{}^{\alpha}{}_{,\alpha\nu} - \bar{h}_{\mu\nu,\alpha}{}^{\alpha}\Big)
\end{aligned}
\tag{2.32}
$$

The last term is the d'Alembertian, and the other terms vanish if $\bar{h}_{\mu\nu,}{}^{\nu} = 0$. Next we make the gauge transformation that will ensure that. Gauge transformations are infinitesimal coordinate transformations $x^{\mu}(\mathscr{P}) \rightarrow x^{\mu}(\mathscr{P}) + \xi^{\mu}(\mathscr{P})$, where the functions ξ^{μ} are small in the same sense as $h_{\mu\nu}$. Effectively, these are small wiggles in the coordinate system. The only quantity that changes is the metric, particularly: $h_{\mu\nu} \rightarrow h_{\mu\nu} - \xi_{\mu,\nu} - \xi_{\nu,\mu}$. The gauge that eliminates the unwanted terms can then be found. This gauge is called the transverse traceless gauge, and we indicate that with a superscript TT. With the correct choice of functions ξ_{ν},

$$
\bar{h}^{\mathrm{TT}}_{\alpha\nu,}{}^{\alpha} = \bar{h}_{\alpha\nu,}{}^{\alpha} - \xi_{\alpha,\nu}{}^{\alpha} - \xi_{\nu,\alpha}{}^{\alpha} = 0 \tag{2.33}
$$

Thus we find the elegant equation:

$$
\Box \bar{h}^{TT}_{\mu\nu} = -16\pi T_{\mu\nu} \tag{2.34}
$$

2.4.1. Gravitational Waves in Free Space

In empty space, this becomes $\Box\bar{h}^{TT}_{\mu\nu} = 0$, the wave equation. Thus, in the limit of weak gravity, disturbances in the spacetime propagate as waves. Note, however, that this is still only an approximate solution. At the outset, we decided to neglect all higher order terms in $h_{\mu\nu}$. Physically, this means we neglected any curvature of spacetime caused by the stress-energy of the wave itself. Further discussion of the energy content of GWs is located in Chapter III, and analysis of a complete GW solution is found in [9, p.957-961].

Then, we have:

$$\begin{aligned} G_{\mu\nu} &= -\frac{1}{2}\bar{h}^{TT}_{\mu\nu,\alpha}{}^{\alpha} \\ &= -\frac{1}{2}\Box\bar{h}^{TT}_{\mu\nu} \end{aligned} \tag{2.35}$$

From this equation, along with the gauge condition, we can make a few observation. First, in empty space, this is the wave equation, $\Box\bar{h}^{\mathrm{TT}}_{\mu\nu} = 0$. Second, the gauge condition $\bar{h}^{\mathrm{TT}}_{\alpha\nu,}{}^{\alpha} = 0$ means that we can find a coordinate system where the amplitude is perpendicular to the propagation direction (this is the transverse part of "transverse traceless gauge"). Third, for a solution of the form $\bar{h}^{TT}_{\mu\nu} = C_{\mu\nu}e^{ik_\sigma x^\sigma}$, the equation requires that $k_\sigma k^\sigma = 0$, making the wave vector a null vector and showing that gravitational waves must travel at the speed of light. Finally, as already discussed above, the wave is traceless. Combining these with the symmetry demanded by the metric, we arrive at the matrix:

$$\bar{h}_{\mu\nu} = \begin{bmatrix} 0 & 0 & 0 & 0 \\ 0 & h_+ & h_\times & 0 \\ 0 & h_\times & -h_+ & 0 \\ 0 & 0 & 0 & 0 \end{bmatrix} \tag{2.36}$$

2.4.2. Emission of Gravitational Waves

This section closely follows [9, §38.10]

Exact solutions of Einstein's Equations that produce gravitational waves (e.g., a binary black hole system) are not currently known. We can, however, study an approximation of it, and the results are shown to be accurate by numerical relativity simulations. In particular, we will assume that all motion in the source is much less than the speed of light; this allows us to return to the Newtonian definition of time, and work with only the spatial components.

Unlike electromagnetic radiation, which is dipolar, quadrupole radiation is the first possible radiation mode for GWs: conservative of mass/energy prohibits a time-changing monopole moment, and conservation of momentum disallows any such change in dipole moment. Any analog to magnetic radiation would violate the conservation of angular momentum. Thus the strongest radiation term must come from the quadrupole moment.

To derive the exact equation, we return to the notation of linearized theory, but without the assumption that curvature is small. We can write Einstein's equations in a similar way as we did before, operating in the Lorentz gauge (but not the transverse traceless gauge yet):

$$\bar{h}^{\mu\nu}{}_{,\alpha\beta}\eta^{\alpha\beta} = -16\pi\big(T^{\mu\nu} + t^{\mu\nu}\big) \tag{2.37}$$

Here, $t^{\mu\nu}$ represents the deviation from linearized theory, and is unknown. We will deal with this not by calculating it, but by carefully manipulating the equations and eventually finding the appropriate approximation that allows us to neglect it.

Equation 2.37 is essentially a 4-dimensional version of the Poisson equation. Since all nonlinearity has been safely stashed in $t^{\mu\nu}$, we can treat $\bar{h}^{\mu\nu}$ as a tensor in flat space. So, it can be turned into an integral simply:

$$\bar{h}^{\mu\nu}(t,\mathbf{x}) = 4\int_{\text{all space}} \frac{[T^{\mu\nu}+t^{\mu\nu}]_{\text{ret}}}{|\mathbf{x}-\mathbf{x}'|}d^3x' \tag{2.38}$$

Now we must make simplifying assumptions. First, we assume that there is a single source of size L producing GWs. Next, we assume that we are far from the source, in the sense that $r >> L$, and restrict to the spacelike components $\bar{h}^{jk}$. Then, to first order, the integral becomes:

$$\bar{h}^{jk}(t,\mathbf{x}) \approx \frac{4}{r}\int_{\text{source}} \left[T^{jk}+t^{jk}\right]_{\text{ret}} d^3x' \tag{2.39}$$

Next, we develop a math trick. Taking the divergence of Equation 2.37:

$$\begin{aligned}(T^{\mu\nu}+t^{\mu\nu})_{,\nu} =& \bar{h}^{\mu\nu}{}_{,\alpha\beta\nu}\eta^{\alpha\beta} \\ =& (\bar{h}^{\mu\nu}{}_{,\nu})_{,\alpha\beta}\eta^{\alpha\beta} \\ =& 0\end{aligned} \tag{2.40}$$

We've used the gauge condition for the last equality. We can further write:

$$
\begin{aligned}
0 =&(T^{\mu\nu} + t^{\mu\nu})_{,\nu} \\
=&(T^{0\nu} + t^{0\nu})_{,\nu} \\
=&(T^{0\nu} + t^{0\nu})_{,\nu 0} \\
=&(T^{0l} + t^{0l})_{,l0} + (T^{00} + t^{00})_{,00}
\end{aligned}
\tag{2.41}
$$

We can also do a different substitution:

$$
\begin{aligned}
0 =&(T^{\mu\nu} + t^{\mu\nu})_{,\nu} \\
=&(T^{m\nu} + t^{m\nu})_{,\nu} \\
=&(T^{m\nu} + t^{m\nu})_{,\nu m} \\
=&(T^{ml} + t^{ml})_{,lm} + (T^{0l} + t^{0l})_{,l0}
\end{aligned}
\tag{2.42}
$$

Subtracting the two equations yields $(T^{00} + t^{00})_{,00} = (T^{ml} + t^{ml})_{,lm}$. Next, we consider the term:

$$
\begin{aligned}
\big[(T^{00} + t^{00})x^j x^k\big]_{,00} &= (T^{lm} + t^{lm})_{,lm} x^j x^k \\
&= \big[(T^{lm} + t^{lm})_{,l} x^j x^k\big]_{,m} - (T^{lj} + t^{lj})_{,l} x^k - (T^{lk} + t^{lk})_{,l} x^j \\
&= \big[(T^{lm} + t^{lm})_{,l} x^j x^k\big]_{,m} - \big[(T^{lj} + t^{lj})x^k - (T^{lk} + t^{lk})x^j\big]_{,l} \\
&\quad + 2(T^{jk} + t^{jk}) \\
&= \big[(T^{lm} + t^{lm})x^j x^k\big]_{,lm} - 2\big[(T^{lj} + t^{lj})x^k - (T^{lk} + t^{lk})x^j\big]_{,l} \\
&\quad + 2(T^{jk} + t^{jk})
\end{aligned}
\tag{2.43}
$$

Thus,

$$T^{jk} + t^{jk} = \frac{1}{2}\big[(T^{00} + t^{00})x^j x^k\big]_{,00} + \big[(T^{lj} + t^{lj})x^k - (T^{lk} + t^{lk})x^j\big]_{,l} - \frac{1}{2}\big[(T^{lm} + t^{lm})x^j x^k\big]_{,lm} \tag{2.44}$$

Note that the last two terms are divergences. This means that when we integrate over the source, the divergence theorem can be used to turn them into surface integrals over the bounding surface. Since there is neither matter nor strong gravitational fields there, these terms vanish when integrated. Thus, our integral becomes:

$$\bar{h}^{jk}(t, x^j) = \frac{2}{r}\int_{\text{source}} \big[(T^{00} + t^{00})_{\text{ret}} x'^j x'^k\big]_{,00} d^3x' \tag{2.45}$$

Now we assume that the source is nearly Newtonian, with its gravitational field holding little energy compared to its mass energy. After swapping the order of integration and differentiation, we see the (retarded) quadrupole moment:

$$\begin{aligned}\bar{h}^{jk}(t, x^j) =& \frac{2}{r}\frac{d^2}{dt^2}\int_{\text{source}} T^{00}_{\text{ret}} x'^j x'^k d^3x' \\ =& \frac{2}{r}\frac{d^2 I^{jk}_{\text{ret}}}{dt^2}\end{aligned} \tag{2.46}$$

Now we remove the trace to find $\bar{h}^{TT}_{jk}$:

$$\bar{h}^{TT}_{jk}(t, x^j) = \frac{2}{r}\frac{d^2 I^{TT}_{jk}}{dt^2} \tag{2.47}$$

Removing the trace from the I^{jk} yields the reduced quadrupole moment:

$$I_{jk}^{TT} = \int T^{00}\big(x_j x_k - \frac{1}{3}\delta_{jk} r^2\big) d^3x \tag{2.48}$$

Finally, in order to have the correct units, we must add back the constants which had been set to 1:

$$\bar{h}_{jk}^{TT} = \frac{2}{r}\frac{G}{c^4}\ddot{I}_{jk}^{TT}\Big(t - \frac{r}{c}\Big) \tag{2.49}$$

So any system with a quadrupole moment that varies in time will emit gravitational radiation. In essence, this translates to any dynamic system that lacks axial symmetry, which includes any orbiting objects. The simplest case, a binary system of equal masses, is examined in Appendix A.1.

This type of system also allowed for the first indirect detection of GWs from the PSR B1913+16 (also named the Hulse-Taylor binary in honor of the astronomers who discovered it) [3]. This system is made up of two neutron stars, one of which is pulsar. By timing the pulses, Hulse and Weisberg were able to measure the orbital period to high precision. Observations spaced out over a decade clearly showed that the period was decreasing, implying that the system was losing energy. Calculations from General Relativity of the expected losses to gravitational radiation matched those losses, providing an indirect proof of the existence of GWs.

The direct detection of the GWs emitted is, as we will show in the next chapter, an extremely difficult task, requiring a well-funded international collaboration. To its great credit, the National Science Foundation generously funded this effort. The indirect detection of GWs from the Hulse-Taylor binary doubtless entered into their consideration.

CHAPTER III

GRAVITATIONAL RADIATION AND LIGO

This chapter contains co-authored material from [13]

As shown in the previous chapter, Einstein's General Relativity gives rise to a new phenomenon: gravitational waves. This is another concrete prediction that diverges from Newtonian gravity. However, as Einstein quickly realized, gravitational waves are extremely difficult to produce, and there was no known process that could create waves large enough to detect at the time. As shown in Equation 2.49, the equation for the amplitude of GWs has a pre-factor of G/c^4, making any GWs produced extremely small. Since the time of Einstein, experimental methods have been greatly improved, and new astronomical sources of GWs identified. In this chapter, we discuss the instrument that made the detection of GWs possible: the Laser Interferometer Gravitational-wave Observatory (LIGO). We begin by showing how objects react to passing GWs.

3.1. The Effect of GWs on Matter

Gravitational waves, being small changes in the metric tensor, manifest themselves (in Newtonian terms) as small changes in the gravitational force on objects. The most obvious way to do this is to to place an object at a particular location and see how it moves, but this method has a serious flaw, as we will show. Consider a freely falling object (a test mass). First, note the form of the metric for flat space with a gravitational wave incoming from the z-direction:

$$ds^2 = -dt^2 + \big(1 + h_+(t)\big)dx^2 + 2h_\times dxdy + \big(1 - h_+(t)\big)dy^2 + dz^2 \tag{3.1}$$

Being unconnected to anything and far from any gravitational body, the test mass can move in any direction if subjected to a force. We can use the geodesic equation to find the equation of motion:

$$\frac{d^2x^\alpha}{d\tau^2} + \Gamma^\alpha{}_{\mu\gamma}\frac{dx^\mu}{d\tau}\frac{dx^\gamma}{d\tau} = 0 \tag{3.2}$$

Since it starts at rest in its own frame, $\frac{dx^j}{d\tau} = 0$ at $t = 0$. Thus, in this frame (at $t = 0$), this reduces to:

$$\begin{aligned} 0 =& \frac{d^2x^\alpha}{d\tau^2} + \Gamma^\alpha{}_{00}\frac{dx^0}{d\tau}\frac{dx^0}{d\tau} \\ =& \frac{d^2x^\alpha}{d\tau^2} + \Gamma^\alpha{}_{00} \end{aligned} \tag{3.3}$$

Now, the Christoffels are found via derivatives of the metric (Equation 2.11):

$$\Gamma^\mu{}_{\alpha\beta} = \frac{1}{2}g^{\mu\nu}\left(\partial_\alpha g_{\mu\beta} + \partial_\beta g_{\nu\alpha} - \partial_\nu g_{\alpha\beta}\right) \tag{3.4}$$

The Christoffels we're looking for will then be:

$$\begin{aligned} \Gamma^\mu{}_{00} =& \frac{1}{2}g^{\mu\nu}\left(\partial_0 g_{\mu 0} + \partial_0 g_{\nu 0} - \partial_\nu g_{00}\right) \\ =& 0 \end{aligned} \tag{3.5}$$

All of these terms vanish because the identified components of the metric are constant. The gravitational wave only appears in the g_{xx}, g_{xy}, and g_{yy} components. Thus, the equation of motion of the test mass is simple as there is no acceleration: $x^\alpha(\tau) =$ constant. Also note that this generalizes to any gravitational wave, not just one traveling in the z-direction.

How can this be true, if we are to measure gravitational waves? We must remember what we have calculated is what happens to the coordinate location of

the test mass in the particular frame and gauge. In a different frame, we would find a different equation of motion just the same as we would under Galilean relativity. What we desire is to find some coordinate system-invariant measurement of the gravitational wave. This requires measuring a scalar. We will measure the distance between the two test masses, using light as our ruler.

But first, we should make sense of why the test mass remains at the same coordinates in the transverse-traceless gauge. Recall that transforming into the transverse-traceless gauge introduced small wiggles into the coordinate system. These wiggles evidently exactly cancelled out the wiggles caused by the gravitational wave.

Now, consider the distance between the two test masses as the gravitational wave passes, assuming that the wavelength of the gravitational wave is much longer than the distance between them, and thus h_+ and $h_\times$ can be considered constants (a more general treatment can be found in Section 3.3). We place them along the x-axis for simplicity and integrate along the curve $\gamma(t) = (0, t, 0, 0)$. Since the curve changes in only one direction, only one term survives:

$$L = \int_0^{L_0} \sqrt{g_{xx}}\, dx = L_0\sqrt{1+h_+} \approx L_0\left(1 + \frac{1}{2}h_+\right) \tag{3.6}$$

The change in length is then $\frac{1}{2}Lh_+$. We measure the strength of gravitational waves with the quantity $\frac{\Delta L}{L}$, which is equal to $\frac{1}{2}h_+$ in this case. This value is called strain, and is dimensionless.

So in principle, the detection of gravitational waves is simple: continually measure the distance between two suspended objects and wait for a gravitational wave to change it. The scale involved makes this task nearly impossible: Consider two neutron stars, orbiting each other with just 1 light-second of separation

between them. In this orbit, they would be traveling over 1,000 km/s, and complete an orbit every 15 minutes. But from 1 kpc away, the GW strain would be less than 1×10^{-20}. For this to produce an observed change in distance of 1 mm, the two objects would have to be separated by 10^{17} meters, or roughly the distance to the star Sirius. So in order to detect GWs, very large and extremely sensitive detectors are needed.

3.2. LIGO

There are currently two detectors that make up the LIGO network [6, 7]: one in Hanford, Washington and the other in Livingston, Louisiana[1]. The two detectors share most aspects of the design, including 4 km long arms. Widely-spaced detectors are important for gravitational wave detection because terrestrial noise sources will be uncorrelated, allowing coherence to be a powerful tool for identification of real astrophysical signals. The detectors feature long arms because of the nature of gravitational waves discussed above.

3.2.1. Laser Interferometry

When two waves overlap, the result is simply the sum of them. Changing the relative phase between the waves will change the interference pattern. In interferometry, this principle is exploited to make high-precision measurements by coupling the objects we wish to measure to the phase of light. The particular kind of interferometer used in LIGO observatories is the Michelson interferometer. It works by sending a laser beam into a beam splitter, down perpendicular arms

[1]Virgo, a sister organization, operates a similar instrument in Pisa, Italy. There is another detector under construction in Japan by the KAGRA collaboration, and LIGO plans to build expand its network with a detector in India.

to suspended test masses, and then recombining them and measuring the output light, as shown in Figure 3.1. When the arms are exactly the same length, the laser power at the output will be at its maximum. But if one of the mirrors moves by a quarter of the wavelength of the light, when it reaches the output its phase will be shifted by π (since it travels the arm once in each direction), and the output power will be zero.

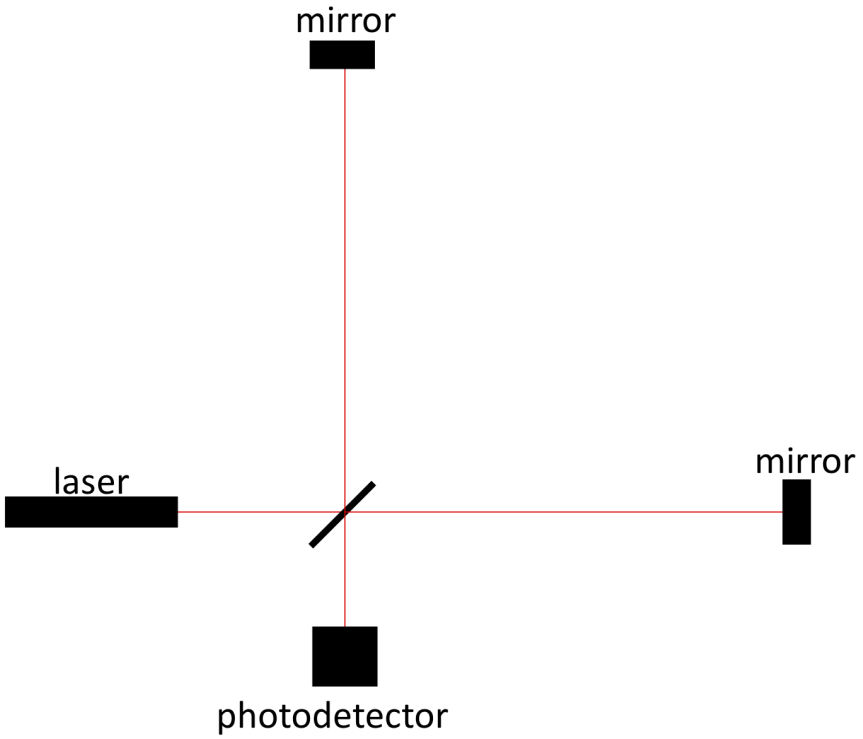

FIGURE 3.1. Diagram of a Michelson inteferometer.

Since visible light has a wavelength of 400–700 nm, this design quickly reaches length scales of about 100 nm. But even with 4 km long arms of the LIGO interferometers, this would reach only strain of 10^{-11}. A gravitational wave with

an amplitude of 10^{-21}, like GW150914, will move the mirrors by only 4×10^{-18} m, about 0.2% of the diameter of a proton.

3.2.2. How a GW is Observed by LIGO

To see precisely how an interferometer reacts to gravitational waves, consider a GW hitting the detector from directly above. As discussed in the previous section, the length of the x-arm will be:

$$L_x = \int_0^{L_0} \sqrt{g_{xx}} dx \tag{3.7}$$

Similarly, the length of the y-arm will be:

$$L_y = \int_0^{L_0} \sqrt{g_{yy}} dy \tag{3.8}$$

However, we cannot easily measure each of these separately. Though the technique of interferometry, we can measure the difference between the two, the Differential ARm-length Measurement (DARM):

$$\begin{aligned} \text{DARM} =& L_x - L_y \\ =& \int_0^{L_0} \sqrt{g_{xx}}\ dx - \int_0^{L_0} \sqrt{g_{yy}}\ dy \\ =& \frac{1}{2}\Big(\int_0^{L_0} \bar{h}_{xx}\ dx - \int_0^{L_0} \bar{h}_{yy}\ dy \Big) \end{aligned} \tag{3.9}$$

For wavelengths much longer than the arms, the integrals are trivial and we find that DARM $= \frac{1}{2}\big(\bar{h}_{xx} - \bar{h}_{yy}\big) = h_+$. For a discussion of the signal produced by GWs from other directions and of shorter wavelengths, see Section 3.3.

3.2.3. Detector Design

Each LIGO detector follows the basic design outlined above, with a host of improvements that together increase the sensitivity by a factor of a billion. We outline a few of the most important ones here. First, we start with an extremely stable and monochromatic laser, because any instabilities will show up at the output. Rather than a single laser beam traveling through once, the inteferometer is made up of a series of optically resonant cavities. Each arm is a Fabry-Pérot cavity, which allows photons to travel the arms multiple times and effectively lengthens the arms. There are also resonant cavities on both the input and output sides of the beam splitter, which work to recycle laser power back into the interferometer and removed undesired modes from the laser beam, improving the purity of the input light further. The arms and optical cavities are all inside of a vacuum system because air would cause additional noise. All mirrors are isolated from the ground by multiple levels of seismic isolation, both active and passive.

Fundamental physics also places theoretical limits on the sensitivity of the instrument. At low frequencies, noise due to the radiation pressure of the light impinging on the test masses. Sensitivity at high frequency is limited by shot noise, caused by the quantum nature of photons. Increasing the laser power reduces the shot noise, but at the price of increased radiation pressure noise. Currently, the LIGO instruments are limited by seismic noise at low frequency, and the laser power is constrained by hardware complications that arise with increased power.

The resonant optical cavities, while essential to the performance of the detector, also greatly increase the difficulty of operation. Each cavity must be kept in resonance simultaneously with all of the other cavities in order for data to be collected. When the detector is in this state, it is referred to as "in

lock." Small deviations from the optimal configuration cause disturbances that spread throughout the detector and can quickly knock the detector out of lock. A multitude of sensors and actuators must work together seamlessly to keep the system operating effectively.

Finally, in order to reach high sensitivity, careful data analysis is required. Many different gravitational wave searches are carried out, and each is tuned to the specific sources targeted. In Chapter V, one such search (using two different software pipelines) is presented, and Chapter VI explores the prospect of a signal following the merger of a binary neutron star system. All searches are concerned with data quality, which is the subject of the next two sections.

3.2.4. Physical Environment Monitor (PEM)

When trying to study movement at a scale smaller than a proton, one quickly discovers that the world is very loud and shaky place. In order to be sure that detected signals are coming from the cosmos and not earth, each LIGO detector has hundreds of sensors monitoring every noise source we can think of. A map of the sensors in the Hanford detector is shown in Figure 3.2. Some are also used to diagnose problems with the operation of the detector: for example, high winds at Hanford can cause enough shaking that the optical cavities wander out of resonance, resulting in the loss of lock. So, we have anemometers monitoring the wind on top of each building and seismometers checking for increased ground motion. The wind pushing on the buildings also slightly deforms the buildings themselves, so tilt meters have been installed in some buildings (seismometers cannot differentiate rotational motion from translational).

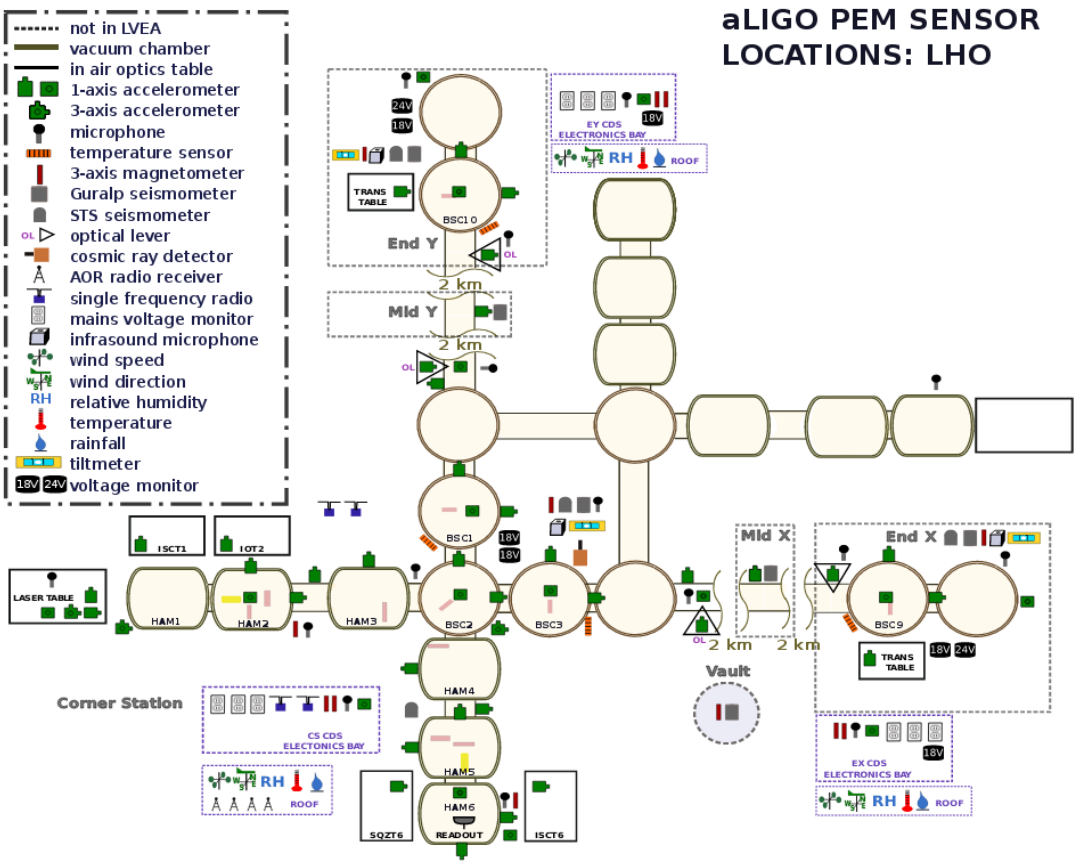

FIGURE 3.2. A map of the sensors which make up LIGO Hanford's PEM system. Available online at http://pem.ligo.org/channelinfo/index.php

Glitch detection is another important role for the environmental monitoring system. Though signal morphology is often a strong veto for matched filter searches, glitches that look similar to expected signals present a huge problem. Unmodeled searches, which cannot veto glitches as effectively, are especially vulnerable to glitches in data. A standard step in validating any candidate GW signal is the examination of all relevant auxiliary channels to search for coincident signals that would point to a local (rather than astronomical) source. See [14] for a full explanation of how the modeled searches for Compact Binary Coalescences (CBC) deal with glitches.

3.2.5. Glitches

While it is often convenient to model noise as a stationary Gaussian process, the noise in LIGO detectors is often more complicated. The noise slowly evolves over time (thus is non-stationary), and is frequently interrupted by transient non-Gaussian features, called glitches. These glitches have many different shapes, sizes, and causes. Some come from the environment (everything from trains, trucks, and snowplows to lightening strikes, power line fluctuations, wind, and ravens pecking at ice built up on liquid nitrogen lines[2]), and others from the electronics and controls systems. The detector characterization team works to identify, classify, and understand each type of glitch. With this work done, data segments with glitches can be easily identified and discarded, allowing searches to be more sensitive to real signals from GWs.

One particularly problematic type of glitch is the blip glitch. Blip glitches are short transients about 10 milliseconds long, in the hundreds of Hz range (example shown in Figure 3.3). Unlike many other glitch types, they do not show up in any auxiliary channels. They are also similar to high mass CBC signals, making them particularly problematic for those searches. As they occur about twice an hour, understanding and eliminating these glitches is a high priority for the Detector Characterization group.

Through analysis of blip glitch rates and auxiliary channel data, we discovered a possible clue to their source: at Hanford, the rate greatly increased at times during the winter of 2015 when the relativity humidity rate inside of the vacuum enclosure areas (VEAs) dropped to near 0%, as shown in Figure 3.4. Livingston also experiences blip glitches, but showed little variation in time.

[2]https://alog.ligo-wa.caltech.edu/aLOG/index.php?callRep=37630

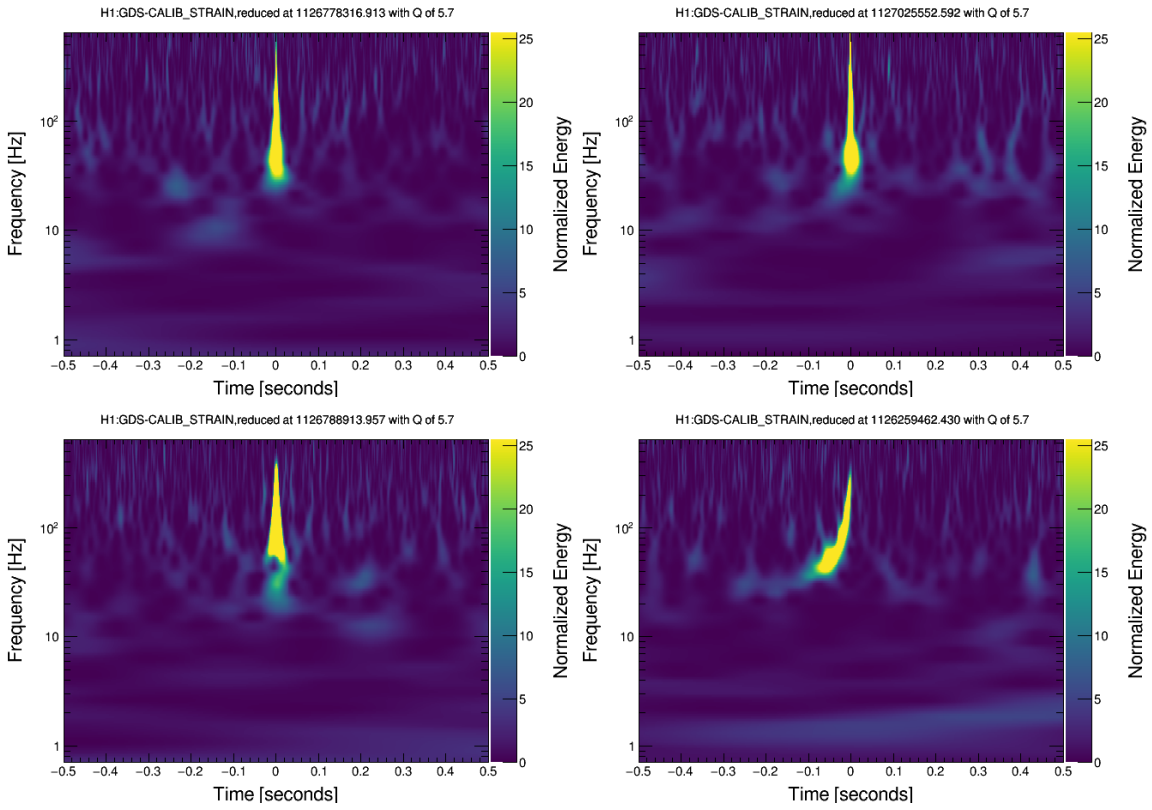

FIGURE 3.3. Q-scans of data from the Hanford detector. Top left, top right, and bottom left are blip glitches, while bottom right is GW150914. While GW150914 is easily differentiated from the blip glitches because of its frequency evolution, high mass ratio systems spend less time in the inspiral phase and so look closer to blip glitches.

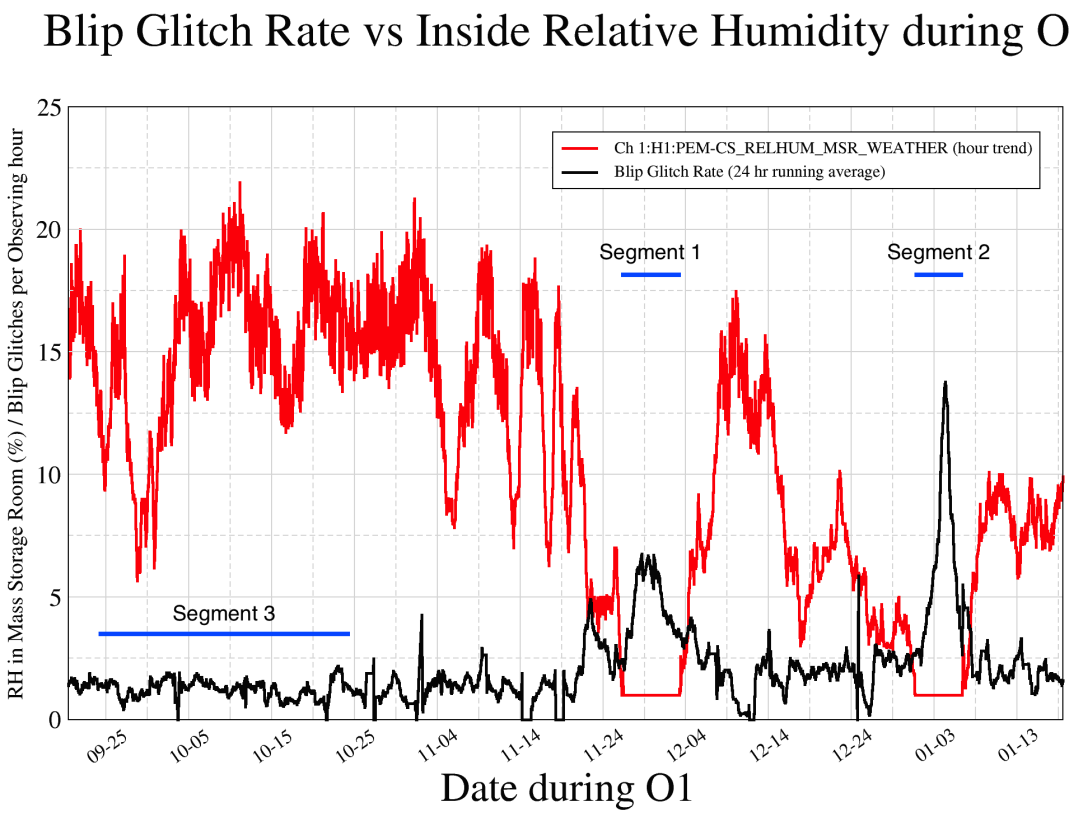

FIGURE 3.4. Comparison of the blip glitch rate with the relative humidity. When the air was very dry (during segments 1 and 2), the blip glitch rate was higher than when it was not (segment 3). This difference was statistically significant.

This correlation, along with the short nature of the glitches, suggests that the source could be related to a discharge of static electricity in electronic components. The most likely suspect was the electrostatic drives, which produce high voltages that are used to actively damp the test masses through the electrostatic force. However, a later investigation which used magnetometers to monitor for such static discharges did not find any correlation.

It is possible that there are two distinct causes of these blip glitches: one that is caused by low humidity, and another that occurs regardless of weather

conditions. Investigations of blip glitches are ongoing, and no cause has yet been found.

3.3. Antenna Response Functions

Previously, we examined how a detector would respond to long-wavelength GWs traveling in the z-direction. Of course in the real world, gravitational waves come from all directions, in both polarizations, and in shorter wavelengths. To see how a generalized GW will be felt, we begin by defining the antenna response function, which states how the detector responds to GWs from a given location and polarization. Consider the strain matrix for the detector's rest frame (in the TT gauge):

$$\bar{h}_{\mu\nu} = \begin{bmatrix} h_{xx} & h_{xy} & h_{xz} \\ h_{xy} & h_{yy} & h_{yz} \\ h_{xz} & h_{yz} & h_{zz} \end{bmatrix} \tag{3.10}$$

We have ignored the time-dimension since we are still using linearized gravity. Following the calculations from above, we see that only the h_{xx} on the length of the x-arm, and similar reasoning shows that only h_{yy} has an effect on the y-arm. Thus in order to find the detector's response to a gravitational wave, we need only transform it into the detector's coordinate system and simply read off the two relevant matrix elements.

Next recall that, for any GW, the strain matrix in its own TT frame is:

$$\bar{h}_{\mu\nu} = \begin{bmatrix} h_{+} & h_{\times} & 0 \\ h_{\times} & -h_{+} & 0 \\ 0 & 0 & 0 \end{bmatrix} \tag{3.11}$$

Here, the z-axis is pointed from the source to the detector. To transform the wave propagation frame into the detector's frame, we need three rotations: First, we rotate around the z-axis until the x-axis is parallel to the detector's x-y plane, calling this the polarization angle ψ. Next, we rotate around the (new) z-axis until it is parallel to the detector's z-axis, with this angle θ being complementary to the altitude of the source. Finally, we rotate by the (new) z-axis until the coordinate systems are aligned. This angle ϕ is equal to the source's azimuth. These rotations can be carried out through matrix multiplication, with the full transformation taking the form:

$$R = \begin{bmatrix} \cos\phi & -\sin\phi & 0 \\ \sin\phi & \cos\phi & 0 \\ 0 & 0 & 1 \end{bmatrix} \begin{bmatrix} 1 & 0 & 0 \\ 0 & \cos\theta & -\sin\theta \\ 0 & \sin\theta & \cos\theta \end{bmatrix} \begin{bmatrix} \cos\psi & -\sin\psi & 0 \\ \sin\psi & \cos\psi & 0 \\ 0 & 0 & 1 \end{bmatrix} \tag{3.12}$$

Since the strain tensor is second-rank, we must transform both indices:

$$\begin{aligned} \bar{h}^{\text{det}}_{\mu\nu} =& R_{\mu}{}^{\alpha} R_{\nu}{}^{\beta} \bar{h}^{\text{wp}}_{\alpha\beta} \\ =& R_{\mu}{}^{\alpha} \bar{h}^{\text{wp}}_{\alpha\beta} (R^{-1})^{\beta}{}_{\nu} \end{aligned} \tag{3.13}$$

Written in matrix equation form, $\bar{h}^{\text{det}} = R\bar{h}^{\text{wp}}R^{-1}$. Following Equation 3.9, $\text{DARM} = \frac{1}{2}\big(\bar{h}_{xx} - \bar{h}_{yy}\big)$, so the signal seen by the detector will be:

$$\begin{aligned} \text{DARM} =& \frac{h_+}{2}\Big((1+\cos^2\theta)\cos 2\phi\cos 2\psi - 2\cos\theta\sin 2\phi\sin 2\psi\Big) \\ &+ \frac{h_\times}{2}\Big(-(1+\cos^2\theta)\cos 2\phi\sin 2\psi - 2\cos\theta\sin 2\phi\cos 2\psi\Big) \end{aligned} \tag{3.14}$$

Expressing this in the form DARM $= F_+ h_+ + F_\times h_\times$, we see that the antenna factors $F_\times$ and F_+ are given by:

$$\begin{aligned} F_+ =& \frac{1}{2}(1+\cos^2\theta)\cos 2\phi \cos 2\psi - \cos\theta \sin 2\phi \sin 2\psi \\ F_\times =& -\frac{1}{2}(1+\cos^2\theta)\cos 2\phi \sin 2\psi - \cos\theta \sin 2\phi \cos 2\psi \end{aligned} \tag{3.15}$$

In practice, we also have another problem. Because detectors are located at different points on a rotating Earth, the altitude and azimuth of astronomical objects must be calculated from their absolute coordinates in the equatorial coordinate system. This can be done in two ways: either calculate the azimuth and altitude for a particular source at a particular time and detector and use the above transformation, or do a series of transformations. For the latter method, an incoming GW is first transformed into a non-rotating frame fixed to the center of the earth, then to one rotating with the Earth, then to the relevant detector's frame.

Finally, there is one more complication in real interferometers. We had assumed that the wavelength of any GW was long compared to the detector, and this assumption holds: a wavelength of 4 km corresponds to a frequency of nearly 75 kHz, and LIGO data is only calibrated up to 4 kHz. However, these instruments are not simple Michelson interferometers; the arms are resonant Fabry-Pérot cavities, so each photon travels down each arm multiple times before recombining at the beam splitter. An exact calculation of this effect, done by analyzing the light as a wave rather than individual photons, is done in [15], and finds that the error is small (a few percent) up to about 1 kHz.

3.4. Energy in Gravitational Waves

Since GWs are capable of moving objects, they must contain energy. But calculating how much energy they contain is not trivial: the most obvious place to look is the stress-energy tensor, but the GW solution we found was for empty space where $T_{\mu\nu} = 0$, to linear order in $h_{\mu\nu}$. Any contributions to the stress-energy tensor from GWs then must be at least quadratic in $h_{\mu\nu}$, and so the linear approximation must be abandoned. Carrying out the calculation of the Einstein tensor to the next order is described in [9, p.969] as a "straightforward but long calculation", with the result:

$$T_{\mu\nu}^{\mathrm{GW}} = \frac{1}{32\pi}\langle \bar{h}_{jk,\mu}\bar{h}_{jk,\nu}\rangle \tag{3.16}$$

The angle brackets indicate that this must be averaged over multiple waves. Stress-energy from gravitational waves cannot be localized: At any point there exists a reference frame in which spacetime is locally flat, and thus the gravitational field cannot contribute any stress-energy. Writing this as GW fluence (energy flux per unit area) in terms of the two polarizations:

$$F_{GW} = \frac{c^3}{16\pi G}\int (\dot{h}_+^2 + \dot{h}_\times^2)dt \tag{3.17}$$

We will use this equation when calculating the minimum detectable energy for the GW searches in Chapters V and VI.

3.5. The First Detection: GW150914

Since shortly after Einstein first published his theory of General Relativity, scientists had known that gravitational radiation was predicted by the theory. It

was not until 1989 that observations of the Hulse-Taylor binary, which showed the system slowly losing energy at the rate expected by the emission of GWs, offered indirect proof of the existence of GWs [16].

The first direct detection of gravitational waves was made on September 14, 2015, when the two LIGO detectors observed the merger of a binary black hole (BBH) system [17]. Through careful analysis of the waveform, it was determined that the system was originally composed of two black holes which weighed 29 and 36 solar masses. During the merger, 3 solar masses of energy ($M_\odot c^2$) was released, resulting in a single black hole with a mass of 62 $M_\odot$. In addition to the wealth of information in gravitational wave data, this was the first time black holes of 30-plus solar masses had been identified. Since then, nearly a dozen more BBH mergers have been observed [18].

3.6. The First Binary Neutron Star Merger: GW170817

LIGO's second observing run yielded the first detection of an inspiraling binary neutron star system [8]. This detection, on August 17 2017, was also the first time gravitational waves were detected in conjunction with electromagnetic observations, as GRB 170817A was detected by Fermi-GBM 1.7 seconds later [19]. Observing both light and gravitational waves from a single event allows a new and independent measurement of the Hubble constant [20]. And since neutron stars are much lighter than the black holes observed merging, the inspiral phase was observable for much longer, increasing the significance of the detection and yielding detailed information about the spins of the stars and the tidal effects they experienced. More on the discovery and an in-depth look at hypothesized post-merger signals and ways to search for them are in found in Chapter VI.

As we saw in Chapter II, any object with a time-varying quadrupole moment will emit gravitational radiation. While the cataclysmic merger of binary systems of compact objects like black holes and neutron stars are the strongest known sources of GWs, many other processes are known to produce them. In the next chapter, we discuss the astrophysics of magnetars, which are a possible source of GWs.

CHAPTER IV

MAGNETAR ASTROPHYSICS

4.0.1. Neutron Stars

Neutron stars are widely accepted to be formed during supernovae, where a dying star with high metallicity collapses due to falling rates of nuclear fusion, bounces off of the core and explodes, losing most of the original mass of the star. The core, compressed to supranuclear densities, lives on as a neutron star. They generally have a mass of 1–2 $M_\odot$ with a radius of about 10 km. As stars spin and have magnetic fields, so too do neutron stars; since their formation involves a huge decrease in radius, conservation of angular momentum and magnetic flux predict a corresponding increase in angular velocity and magnetic field strength. Both of these features have been observed: neutron stars typically have polar magnetic fields of 10^{11}–10^{13} G (compare to our sun's 1–2 G[1]), with spin rates from under 0.1 Hz to as high as a few hundred Hz.

The makeup of neutron stars is not fully understood. The star is supported against further gravitational collapse only by neutron degeneracy pressure and the strong nuclear force. This state of matter, with neutrons (along with a few protons and electrons) packed together more tightly than in an atomic nucleus, is found nowhere else in the universe and cannot be reproduced in a laboratory. This makes it difficult to determine the physical characteristics of neutron star matter. The equation of state, which describes how density depends on pressure, is not yet known, though there are a number of models for it (see more discussion in Chapter VI). These models must accurately account for a wide range of physical

[1]https://nssdc.gsfc.nasa.gov/planetary/factsheet/sunfact.html

phenomenon, from the more ordinary magnetohydrodynamics that governs their atmospheres to the quantum field theory of the individual neutrons, to the general relativistic effects caused by the strong gravitational field.

It is even possible that some neutron stars are not neutron stars, but quark stars, an even denser star where the quarks are packed too tightly for hadronization to be possible [21]. None have been confirmed to exist, though one star was identified as a possible candidate before further observations confirmed that it is an ordinary neutron star [22, 23]. As they are more dense than neutron stars, they would be excellent targets for gravitational wave searches.

A wide range of behaviors have been observed from neutron stars. Many are pulsars, which emit regular pulses of light. The frequency of these pulsations (up above 1 Hz), along with their stability, prove that these must be neutron stars: No other known object is compact enough to allow for that rotational velocity while having the ability to emit light [24]. Most pulsars emit primarily at radio frequencies, but some emit x-rays. The first x-rays pulsars discovered were in binary systems and powered the emission by pulling matter off of their neighbor. However, some x-ray pulsars did not have a neighbor, and thus could not be powered by accretion. These were named the Anomalous X-ray Pulsars (AXPs). A separate group of neutron stars, known for occasional short bursts of soft γ-rays, were named the Soft Gamma Repeaters (SGRs). As more has become known about these objects, they have been combined into a single class: magnetars.

4.1. History of SGRs and AXPs

The first observations of magnetars were the soft γ-ray bursts from SGRs, and were originally categorized as a new type of GRB. However, unlike typical

GRBs (which are caused by cataclysmic events like BNS mergers and supernovae), these tended to come from the same locations. It was not until 1979, when a new, massively energetic event was observed at the same location where bursts of soft γ-rays had previously been seen, that a neutron star was hypothesized as the source [25]. The timescale of the burst was so short (milliseconds) and the event so energetic (10^{46} erg), that the source must be a very small and very energetic object.

This object (now named SGR 0526-66) and other repeating sources of soft γ-rays became known as Soft Gamma Repeaters (SGRs), though it was unknown what physical characteristics caused them to be different from other neutron stars.

In the 1990s, a new class of pulsars was identified, called the Anomalous X-ray Pulsars (AXPs). Unlike other x-ray pulsars, these stars were not powered by their rotation (known by comparison of the pulsed EM energy and their loss of rotational energy) nor accretion, as they were isolated neutron stars.

As more observations of AXPs and SGRs were made, it became clear that these two groups had more in common than originally thought. SGR-like bursts were observed from an AXP [26]. A previously-identified SGR was found to give off pulsed x-rays [27]. What they shared was an unusually strong magnetic field which fed its energy into the previously unexplained behaviors. A summary of the observations from SGRs and AXPs is found in Sections 4.3 and 4.4.

4.2. The Magnetar Hypothesis

The magnetar hypothesis states that the AXPs and SGRs are two manifestations of the same phenomenon—a star whose magnetic field powers emission and outbursts [28]. Their magnetic field strengths are generally in the range of

$10^{14} - 10^{15}$ G, though some are lower. For example, the magnetar SGR 0418+5729 has a dipolar field strength of only 7.5×10^{12} G, which is lower than some non-magnetar pulsars [29]. They spin at a rate of 1 revolution every 2 to 12 seconds, as evidenced by the x-ray pulsations. The fact that all magnetars have spin periods in such a narrow range points to a common spin-down mechanism during birth. Currently there are 23 confirmed magnetars, with another 6 candidates[2]. In the next sections, we discuss the current understanding of magnetars and their activities.

4.2.1. Magnetic Field Strength

Magnetic fields in magnetars are estimated through the spin-down rate. Through classical electrodynamics, a spinning magnetic dipole will radiate away energy and angular momentum, slowing its rate of rotation. This rotation rate can be calculated with great precision for pulsars, including magnetars with detectable pulsations. Combining this with an estimate of the star's angular momentum yields the rate of change of the rotational kinetic energy E:

$$\dot{E} = \frac{d}{dt}\frac{1}{2} I\Omega^2 = I\Omega\dot{\Omega} \tag{4.1}$$

Here, I is the star's moment of inertia and Ω is its rotational velocity. Following [24, p.8-9], this can be compared to the energy radiated by the spinning magnetic dipole by analyzing the magnetic field of the star in two regimes: near the magnetar, where the field moves in lock step with the rotation of the star, and far from it, where such evolution is prohibited by relativity and thus radiation fields dominate. The former is simply the field of a magnetic dipole, $B_{dipole}(r) =$

[2]See the catalog at `http://www.physics.mcgill.ca/~pulsar/magnetar/main.html`

$B_0(a/r)^3$, where a is the radius of the star. The latter is $B_{wave}(r) = B_0(a/r)$. They must be equal at the point that an object rotating at the same rate as the star would being traveling at the speed of light, which is at a distance of $r = c/\Omega$. Thus, at this location we have $B_{wave} = B_0(a\Omega/c)^3$. The power radiated by the field per unit area will be $2B^2c/3\mu_0$ (the factor of 2/3 is due to the radiation pattern). If the torque due to the spinning dipole magnetic field is responsible for the star's rotation slowing down, we arrive at:

$$\dot{E} = \frac{8\pi B_0^2 a^6 \Omega^4}{3\mu_0 c^3} \tag{4.2}$$

Combining this with Eq. 4.1 yields:

$$B_0 = \sqrt{\frac{3\mu_0 c^3 I\dot{\Omega}}{8\pi a^6 \Omega^3}} \tag{4.3}$$

It is usually more convenient to write this in terms of rotational period ($P = 2\pi/\Omega$) and its time derivative ($\dot{P} = -2\pi\dot{\Omega}/\Omega^2$):

$$B_0 = \sqrt{\frac{3\mu_0 c^3 IP\dot{P}}{32\pi^3 a^6}} \approx 3.2 \times 10^{19}\sqrt{\frac{P}{1\text{ sec}}\dot{P}}\text{ G} \tag{4.4}$$

4.3. Continuous Emission

Though initially SGRs were not known to be x-ray pulsars, all SGRs have now been discovered to emit pulsed x-rays. Since the light is beamed from a particular location on the star, the timing of the pulses indicates the spin period of the star. This allows for the estimation of the dipole magnetic field strength, as outlined above.

Some magnetars have also experienced "glitches" in their rotation rate, where the rotation rate suddenly speeds up by a small amount. The same behavior has been seen in ordinary pulsars. The leading hypothesis is that the inner core of the star rotates faster than the crust, and when a glitch occurs some angular momentum is transferred outward. However, anti-glitches, where the rotation rate suddenly decreases, have also been observed in two magnetars [30, 31]. The mechanism responsible for anti-glitches is not understood, and may lead to new theories about ordinary glitches.

The measured values for energy radiated in these pulsed emissions shows that magnetars are very different than typical pulsars: there is significantly more energy radiated in x-rays than there is rotational energy lost. And since magnetars have no companion object to take energy from, magnetars must be powered by their magnetic fields. In the next section, we will discuss the transient events that first brought magnetars to the attention of astronomers, and further reinforce the need for a large amount of energy stored in the magnetic field.

4.4. Short Bursts and Giant Flares

Occasionally and unpredictably, magnetars give off short bursts of soft γ-rays, lasting 0.01–1 sec. The burst duration and time between bursts follow lognormal distributions [32]. They can occur at any point in the star's rotation, and the light curves vary widely, even among bursts from the same magnetar. The exact mechanism behind these bursts is unknown, but may be caused by seismic events, Alfvén waves in the star's atmosphere, magnetic reconnection events, or some combination of these (see e.g. [33]). In particular, one model posits that the magnetic field gradually weakens, which causes strain in the crust of the magnetar.

When the crust formed, the magnetic and gravitational forces cancelled out, but this changes as the magnetic field weakens. Eventually, the crust cracks, allowing a reconfiguration of the magnetic field nearby and releasing a large amount of energy [34].

Giant flares are the much larger (and rarer) cousins of short bursts. At their peak, which lasts a few tenths of a second, they reach intensities in the range of 10^{45} erg/s. Though the initial peak is short-lived, giant flares have long tails: the persistent emission does not return to normal levels for hundreds to thousands of seconds. Only three giant flares have been definitively identified (all coming from magnetars in or near the Milky Way), though some extra-galactic γ-ray bursts may have actually been magnetar giant flares [35, 36]. Recently, some bursts with energies between that of short bursts and giant flares have been reported [37]. This, and other theoretical work (e.g. [34]), suggests that giant flares and short bursts are caused by similar mechanisms.

4.4.1. Quiescence and Outbursts

Some magnetars exhibit variability in their activity. They may have long periods of quiescence where their continuous pulsed emission is reduced and they produce no short bursts, then suddenly and unpredictably awaken. In just days, their emission can rise by order of magnitude and produce a flurry of short bursts [38]. These are called transient magnetars, and the first one discovered was XTE J1810–197 [39].

At present, we have do not have enough data on magnetars to have a complete picture. Fewer than 30 magnetars have been identified. Only three magnetars have been observed producing a giant flare, and each has only done so

once, so we do not know if a magnetar is even capable of producing more than one in its lifetime.

4.5. Magnetars as a Source of GWs

As they are highly compact objects capable of intense outbursts, magnetars are a promising source of GWs. In the next chapter, we present a search for such GWs, targeting two possible emission types at two timescales. The first would is motivated by so-called quasi-periodic oscillations, will be discussed below in Section 4.5.1. The second mechanism is an excitation in the fundamental mode (or f-mode) of the star, which is primarily damped by gravitational radiation and would last less than a second.

4.5.1. Quasi-Periodic Oscillations

After giant flares, there is a soft X-ray tail which lasts for hundreds of seconds. Quasi-periodic oscillations (QPOs) have been observed in this tail of giant flares [40, 41] and some short bursts [42, 43], during which various frequencies appear, stay for hundreds of seconds, and then disappear again, indicating a resonance within the magnetar. Many possible resonant modes in the core and crust of the magnetar have been suggested to cause the QPOs, although it is unclear which modes actually produce them. For QPOs well above 100 Hz, Alfvén waves may be the cause [34].

Some of these resonant modes, such as f-modes and r-modes, couple well to GWs. Other modes, such as the lowest order torsional mode, do not create the time changing quadrupole moment needed for GW emission (see Section 2.4.2). None of these models provide precise predictions for emitted GW waveforms.

4.5.2. Estimates of GW Energy

Though there are no exact models of GW emission from magnetars, a few papers have worked to model and constrain the output GW energy. For example, [44] built on a previous model to constrain the GW energy of a giant flare to 10^{48}–10^{49} erg. This energy is far above the electromagnetic energy of giant flares, and would be detectable for most waveforms up to a few kilohertz at distances of 10 kpc (for full upper limits and their astrophysical implications, see Chapter V).

Later, a pair of papers set the upper limit much lower [45, 46]. The first used theory to show that only a small fraction of a giant flare's energy would flow into the star's f-mode. Since this is the mode that most directly couples to gravitational radiation, this severely limits the GW energy that can be produced. The other relied on numerical magnetohydrodynamics with general relativity, and directly modeled the GWs emitted during a giant flare (which were mostly, but not all, from the f-mode). The gravitational waves created in their simulations would not be detectable by Advanced LIGO even when operating at design sensitivity. They also show that the emitted GW energy is strongly dependent on the magnetic field strength, with the resulting strain going as $(B_{\rm pole})^{3.3}$, and would require the magnetar to have a field stronger than 10^{16} G.

Nevertheless, we searched for evidence of GWs coincident with magnetar activity. A brief overview of the source properties is below, and the search is explained in Chapter V.

4.6. SGR 1806-20

The magnetar bursts for which I searched for a gravitational wave counterpart all came from SGR 1806-20. This magnetar was one of the first identified, and

produced a giant flare in 2004 [47]. Its magnetic field is the strongest yet measured, at an estimated 2×10^{15} G, and it has had periods of vigorous bursting activity since the 2004 giant flare.

The bursts studied are all at much lower energy than a giant flare, with the highest being 10^{38} erg (assuming a distance of 8.7 kpc and isotropic energy distribution). Light curves for the bursts are shown in Fig. 4.1. Both the plots as well as notification of the bursts themselves came from David Palmer, who found them in sub-threshold SWIFT-BAT data [48].

Since these are sub-threshold events, they have not been officially named. Here, we adopt the convention used by the Fermi Gamma Ray Monitor, which labels bursts according to the source type, name (if location is unavailable), and date. Thus the burst from SGR 1806-20 on February 25, 2017 is called SGR1806170225.

4.7. GRB170304003A

The other burst was classified as a GRB from the Small Magellanic Cloud. The data from the Fermi satellite is displayed in Figure 4.2. The spectrum was similar to that of many SGR short bursts. Though no SGR is known to be at this location, the presence of an energetic burst makes this an appealing target for a GW search.

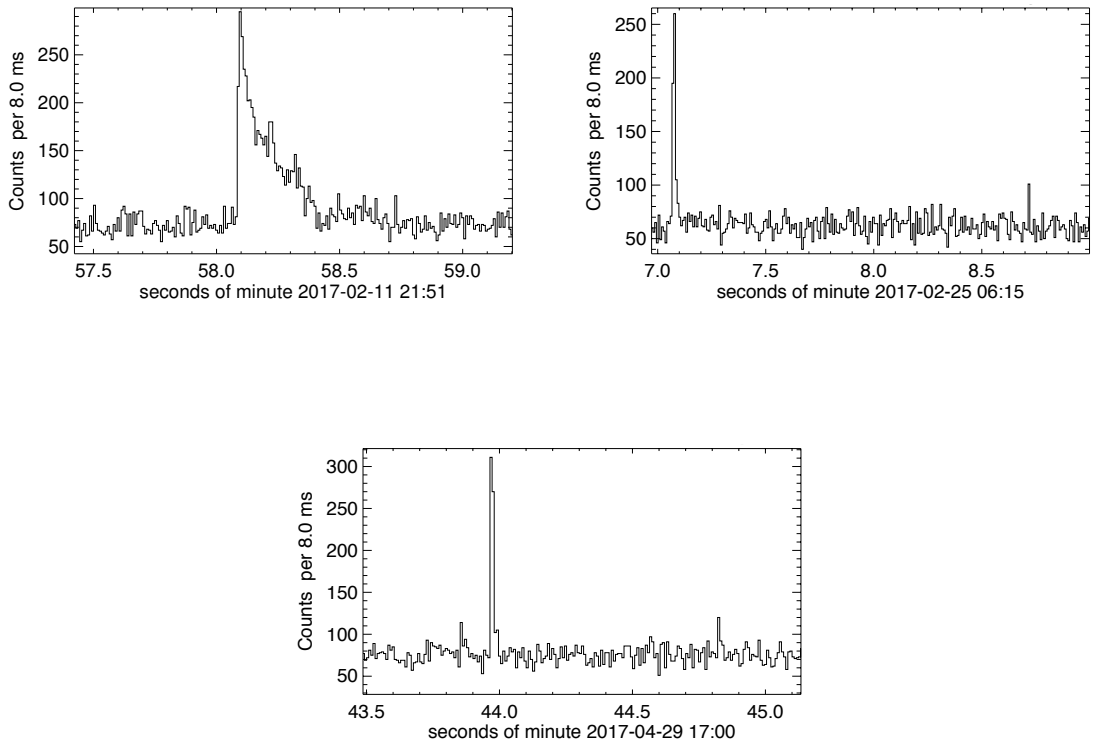

FIGURE 4.1. Data from SWIFT-BAT for the three bursts from SGR 1806-20

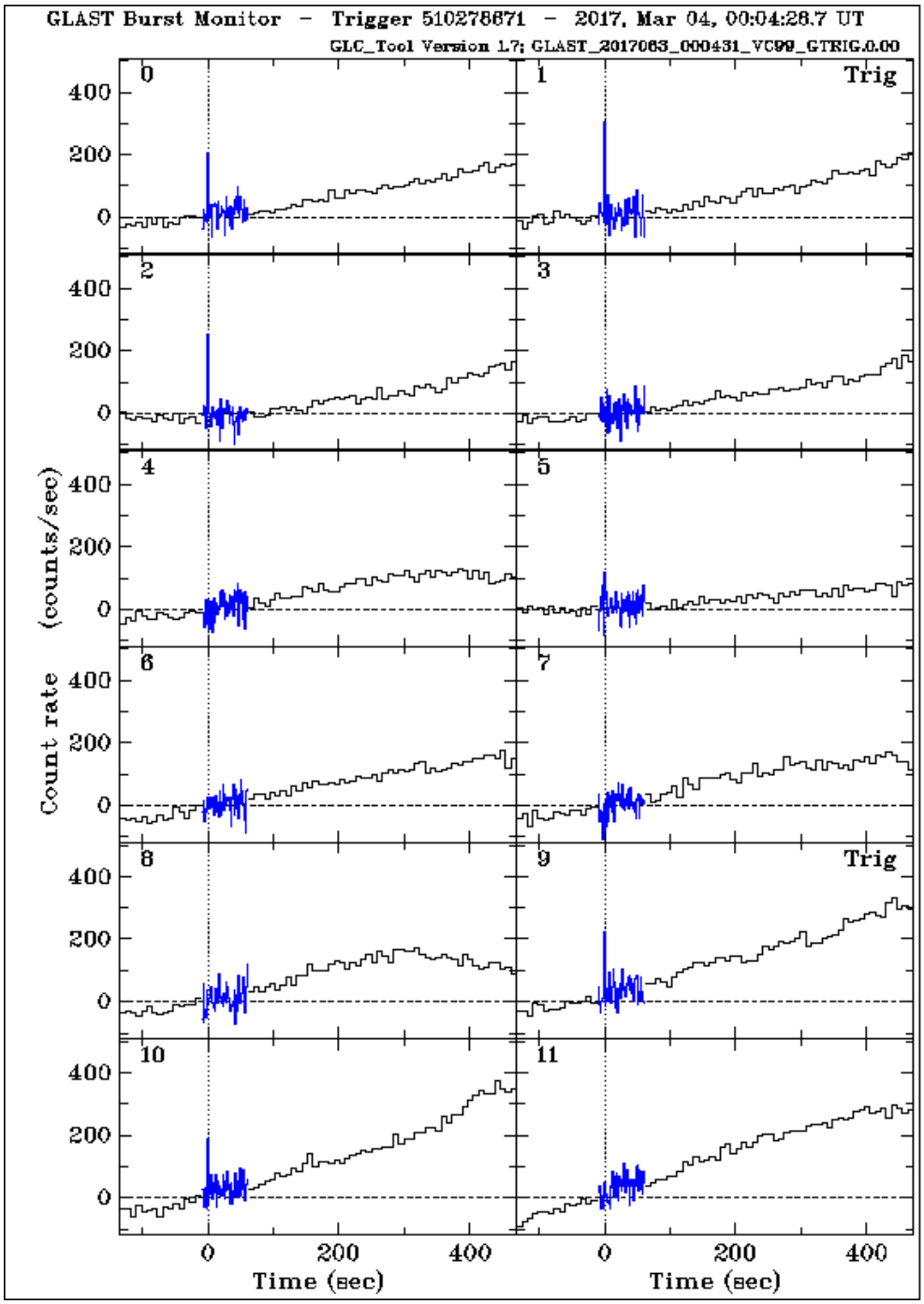

FIGURE 4.2. Data from the Fermi GBM for the GRB170304A

CHAPTER V

SEARCH FOR GRAVITATIONAL WAVES ASSOCIATED WITH MAGNETAR TRANSIENTS

This chapter contains co-authored material from [49].

So far, LIGO [7] and Virgo [50], have reported detections of eleven gravitational-wave (GW) signals from coalescence of compact binary systems [18]. Isolated compact objects may also emit detectable GWs, though they are predicted to be much weaker than compact binary coalescences [51]. Because of the high energies and mass densities required to generate detectable GWs, neutron stars and supernovae are among the main targets of non-binary searches.

The large energies involved originally led to the belief that magnetar bursts could be promising sources of detectable gravitational waves, e.g. [44, 52]. Further theoretical investigation indicates that most mechanisms are likely too weak to be detectable by current detectors [45, 46]. Nevertheless, due to the large amount of energy stored in their magnetic fields and known transient activity, magnetars remain a promising source of GW detections for ground-based detectors with rich underlying physics.

This search was triggered following identification of magnetar bursts by γ-ray telescopes. The methodology is similar to one done during Initial LIGO's sixth science run [1, 53] with a few improvements and the use of an additional pipeline targeted toward shorter-duration signals (X-Pipeline) [54]. This pipeline has been used to look for GWs coincident with γ-ray bursts (GRBs) (see [55] for such searches during Advanced LIGO's first observing run). There were also two other searches for GW counterparts from magnetar activity during Initial

LIGO using different methodology — one triggered by observations of the 2004 giant flare [56], the other short bursts during Initial LIGO's fourth science run [57, 58, 59]. Additionally, a magnetar was considered as a possible source for a GRB during Initial LIGO (GRB 051103), and a search using X-Pipeline and the since-deprecated Flare pipeline placed upper limits on GW emission from the star's fundamental ringing mode [35].

This search was performed on data coincident with the four short bursts from magnetars during Advanced LIGO's second observing run for which there was sufficient data (we require data from two detectors) for both short-duration (less than a second long) and intermediate-duration (hundreds of seconds long) signals. Table 5.1 describes the four bursts; the light curves can be found in Chapter IV. In addition to the four studied bursts, there were five bursts that occurred during times when at least one detector was offline. No GW analysis was done on them. All GW detector data comes from the two LIGO detectors because Virgo was not taking data during any of these bursts.

Source	Date	Time (UTC)	Duration (s)	Fluence (erg cm^{-2})	Distance (kpc)
SGR 1806-20	Feb 11, 2017	21:51:58	0.256	8.9×10^{-11}	8.7
SGR 1806-20	Feb 25, 2017	06:15:07	0.016	1.2×10^{-11}	8.7
GRB170304A	March 4, 2017	00:04:26	0.16	3.1×10^{-10}	–
SGR 1806-20	April 29, 2017	17:00:44	0.008	1.4×10^{-11}	8.7

TABLE 5.1. List of magnetar bursts considered in this GW search. GRB170304A is described in GCN circular 20813; data on SGR 1806-20 burst activity is courtesy of David M. Palmer.

5.0.1. Excess Power Searches

Fundamentally, all multi-detector GW searches seek to identify GW signals that are consistent with the data collected at both detectors. Some searches identify candidate signals in each detector separately, then later consider only the candidates that occur in all detectors within the light-travel time and with the same signal parameters. However, this generally requires a model that can accurately predict how the GW strain evolves over time, which in turn can be used to predict the response of the detectors. These predictions are called templates, which are then compared against the detector data. We cannot perform a templated search here because there is no current model which can produce templates for magnetar GW bursts. Instead, we first combine the two data streams to create a time-frequency map where the value in each time-frequency pixel represents some measure of the GWs (often energy) consistent with the observations from the detectors. The way this is done in the analysis pipelines used for this search will be discussed below.

The next step is to identify GW signals in the time-frequency map. This is done by clustering together groups of pixels, calculating the significance of each cluster with a metric, and searching for the most significant cluster. Finally, we conduct the same search on data where we know there is no signal, and compare this background to the search result for data taken around the time of the magnetar burst (the "on-source" data). In order to cover a broader range of frequencies and time scales, we use two different analysis pipelines which use different clustering algorithms.

The short-duration search uses seed-based clustering implemented by X-Pipeline, which focuses on groups of bright pixels (the seed) [54]. Specifically,

the clusters considered by X-Pipeline are groups of neighboring pixels that are all louder than a chosen threshold. This approach works well for short-duration searches, but fails for longer-duration signals for two reasons: random noise will tend to break up the signal into multiple clusters, and each pixel is closer to the background, so fewer of them will be above the threshold.

We rely on STAMP [60] for the intermediate-duration search. STAMP offers a seedless method whose clustering algorithm integrates over many, randomly chosen, Bézier curves [61, 62]. Because of this, it can jump over gaps in clusters caused by noise, and thus it is better suited for longer-duration signals. Additionally, it can build up signal-to-noise ratio (SNR) over many pixels of only slightly elevated SNR. This method was previously used to search for signals from magnetars during Initial LIGO [1, 53].

5.1. STAMP

The Stochastic Transient Analysis Multi-detector Pipeline (STAMP) was designed to search for unmodeled long-lived narrowband signals, and is described in detail in [60]. Below is an overview and analysis of features germane to the particularities of this search.

5.1.1. Cross-Power and the Filter Function

Since any gravitational wave can be treated as superposition of plane waves, the phase difference between the GWs incident on each detector is determined by the distance between the detectors and the sky locations. This is the basis of coherent GW searches. STAMP implements this idea by first considering the

cross-power in the data streams of the two detectors. The cross-power in a time-frequency pixel is given by

$$CP = \tilde{s}_I^*(t;f)\tilde{s}_J(t;f)e^{2\pi i f\hat{\Omega}\cdot\Delta\vec{x}_{IJ}/c} \tag{5.1}$$

Here, $\tilde{s}_I$ is the Fourier transformed data stream from the detector I, $\hat{\Omega}$ is a unit vector indicating sky location, and $\Delta\vec{x}_{IJ}$ is the displacement vector between the two detectors. The complex exponential term is required to correct for the difference in the GW's phase at the two sites.

Next, we must account for the two independent polarizations of GWs and the effect they have on the detectors. To do this, we calculate the *antenna functions* $F_I^A(\hat{\Omega},t)$, which describe how the interferometers react to GW strain in a particular polarization at a particular sky location. They defined using the equation $\tilde{s}_I(t;f) = \sum_A \tilde{h}^A(t;f,\hat{\Omega},A)F_I^A(\hat{\Omega},t) + \tilde{n}(t;f)$, where $\tilde{h}^A(t;f,\hat{\Omega},A)$ is the strain due to the GW with polarization A at frequency f, and $\tilde{n}(t;f)$ is the noise in the detector. Now, we can expand the cross power relation, taking an average over pixels and assuming that the noise at each site is uncorrelated with both the signal and the noise at the other site:

$$\begin{aligned}\langle CP\rangle &= \sum_{A,A'}\langle\tilde{h}^{*A}F_I^A\tilde{h}^{A'}F_J^{A'}e^{2\pi i f\hat{\Omega}\cdot\Delta\vec{x}_{IJ}/c}\rangle \\ &= \sum_{A,A'}\langle\tilde{h}^{*A}\tilde{h}^{A'}\rangle F_I^A F_J^{A'}e^{2\pi i f\hat{\Omega}\cdot\Delta\vec{x}_{IJ}/c}\end{aligned} \tag{5.2}$$

For co-located detectors, the antenna functions will be the same, and thus the average of the cross power due to a signal will always be a real number. However, the detectors are not co-located; thus in some cases we expect to find a complex number with nonzero imaginary part. With information about the polarization of

the gravitational waves, we can refine this, see Section 5.1.8 below. For example, if the GWs are unpolarized (i.e., the polarizations are uncorrelated), then:

$$\langle CP_{\text{unc}} \rangle = \sum_A \langle \tilde{h}^{*A} \tilde{h}^A \rangle F_I^A F_J^A e^{2\pi i f \hat{\Omega} \cdot \Delta \vec{x}_{IJ}/c} \tag{5.3}$$

Though in this case, we are looking for an elliptically polarized signal, without knowing the two polarization angles ι and ψ, using the unpolarized filter function is the best we can do.

After this, STAMP uses an estimate of the detectors' power spectral density (PSD) to whiten the data (an example of a PSD is found in Figure 5.1). Then each pixel is divided by the variance of the surrounding pixels. An example SNR map, made using data taken a few hours before the burst on February 25, 2017, is shown in Figure 5.2. If the detector data is Gaussian noise, the resulting SNR of the pixels will follow a Gaussian distribution.

5.1.2. Clustering Algorithm

We are searching for intermediate-duration (on the order of hundreds of seconds) gravitational waves, with few theoretic clues as to the waveform. For the range of frequencies that LIGO is sensitive to, hundreds of seconds corresponds to quality factors at least in the thousands. Since gravitational waves are caused by oscillations of matter, the creation of such waves requires a high finesse mechanical mode, which must have a very small bandwidth.

Thus we focus on narrowband gravitational wave signals. Such signals appear in the time-frequency map described above as curves that are a single pixel wide. So the problem of finding gravitational waves is reduced to finding curves with the loudest SNR.

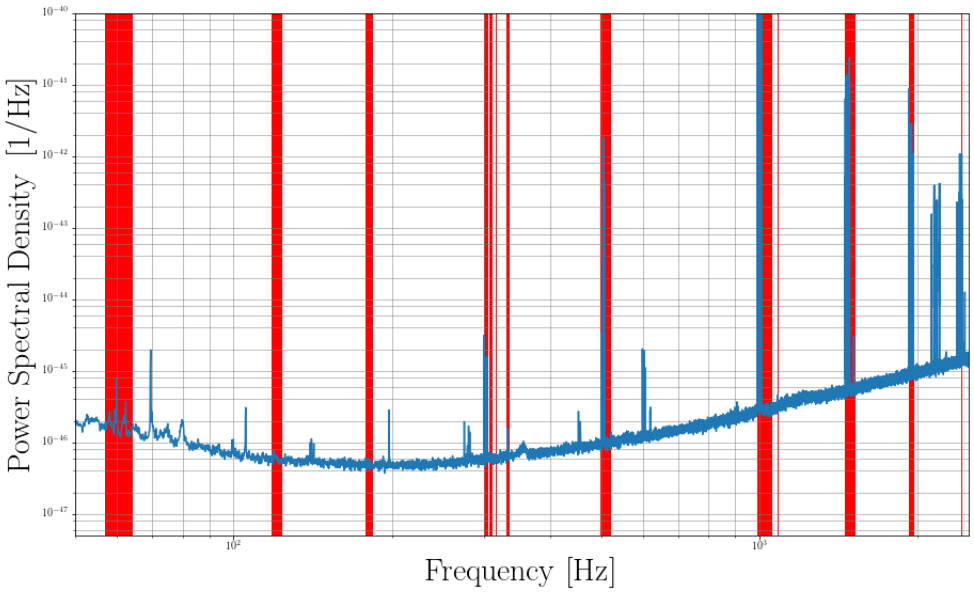

FIGURE 5.1. An estimate of the PSD of the noise in the Hanford detector during O2. The red bars are frequencies which are excluded due to excess noise at those specific frequencies, see Section 5.1.3.

For short and loud signals, a viable method might be to consider only the loudest pixels in the map. This is how X-Pipeline works, which will be discussed later in this chapter. For longer and weaker signals, however, this is not ideal. Such a signal would only rise slightly higher than the noise in the data stream, and could be overpowered by noise at times. So instead of relying on individual loud pixels, we generate random groupings of pixels (clusters) according to the expected signal morphology and calculate the SNR of each cluster, and record the loudest cluster in each time-frequency map [61]. When a map returns a higher SNR than expected from random noise, we can conclude that a signal is present (see Section 5.1.6 for details).

In particular, we generate 30 million Bézier curves, which are a type of smooth curve parameterized by three points. These curves are continuous in

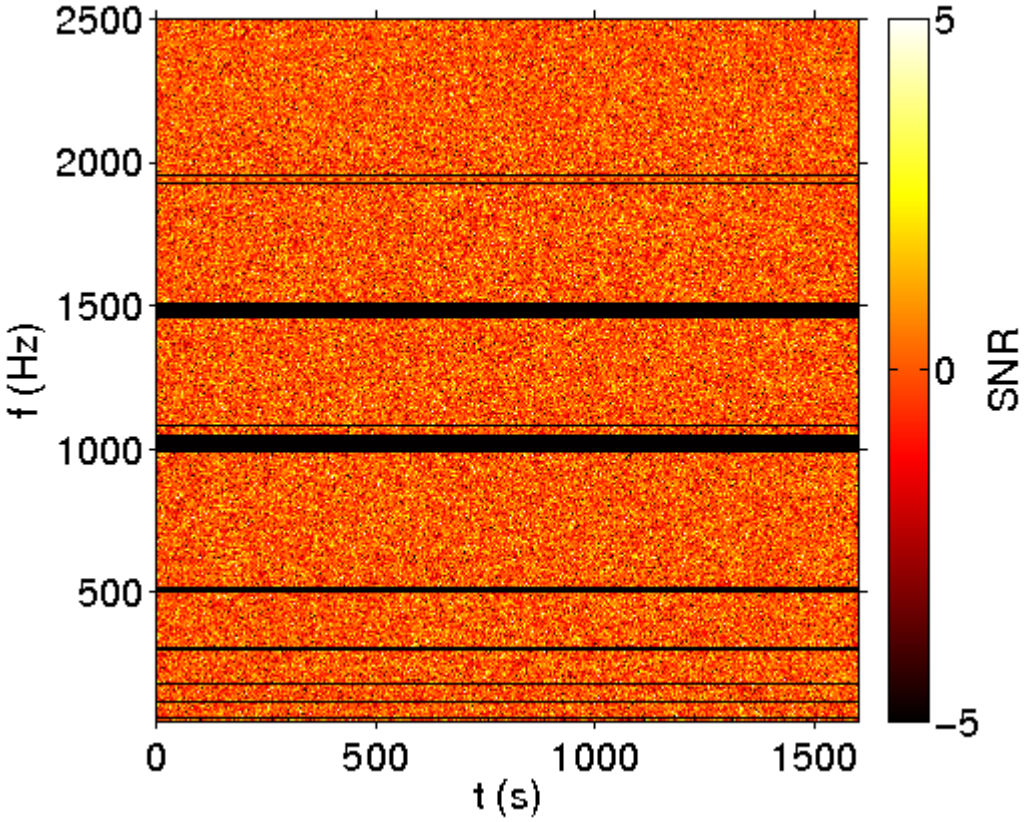

FIGURE 5.2. An example of a time-frequency SNR map calculated by STAMP. This map was used as part of the background for the February 25 burst, as explained in Section 5.1.6. The black bars are at frequencies that have been notched out due to known noise sources.

frequency, but the time-frequency maps only have values for integer frequencies. To resolve this discrepancy, we average as appropriate, e.g. $\mathrm{SNR}(f = 59.4\mathrm{Hz}) = 0.6 \times \mathrm{SNR}(f = 59\mathrm{Hz}) + 0.4 \times \mathrm{SNR}(f = 60\mathrm{Hz})$.

There is one last constraint on our clusters: since we hope to find signals related to QPOs, it makes sense to search for signals with the same signal morphology as QPOs, namely monochromatic ones. It is unclear how precisely monochromatic QPOs are, so we allow the signal frequency to change by up to 10% of the original frequency.

Finally, we must decide how to construct the multi-pixel SNR statistic. Summing the SNR of each pixel in the cluster is not ideal, since this method will tend to include noise on either side of the signal. Taking the mean of the pixels is also not ideal because we would like to bias toward longer clusters. So we use a middle ground, and use:

$$\mathrm{SNR}_{\mathrm{tot}} = \frac{1}{\sqrt{n}} \sum_{i}^{n} \mathrm{SNR}(p_i) \tag{5.4}$$

where $\mathrm{SNR}(p_i)$ is the SNR of the ith pixel in the cluster.

5.1.3. Detector Noise

Generally in gravitational wave detector data analysis, we assume that the data is Gaussian. This assumption makes the statistics and significances reported by searches also come out Gaussian. However, in reality we know that this is not the case. In the time domain, short non-Gaussian transients, called glitches, are numerous and well studied. In frequency, the spectrum contains many lines due to everything from the AC frequency of the power mains to injected calibration lines to mechanical resonances in various detector components.

One significant advantage of this longer duration search is that short-duration glitches can be mostly ignored. All clusters are a minimum of 50 seconds long, reducing the impact of short glitches, and dividing by the variance of nearby pixels suppresses broadband glitches.

Lines, frequencies with unusually high noise, can be a major problem for this search, since we are searching for a signal that looks like a line (see Figure 5.1). For example, the power grid operates at 60 Hz, so excess noise is expected (and

seen) at 60 Hz and its harmonics. The suspensions that hold the test masses have resonances at about 500 Hz and harmonics at 1000 Hz.

In order to mitigate these, we first eliminate frequencies with a known line. We used the list of lines used for the all-sky long duration stochastic search. Any other lines that may be present will be somewhat suppressed through dividing by the background PSD, and we examined the background to ensure that no one frequency was showing up more often than would be expected by chance.

5.1.4. Non-Monochromatic Waveforms

For simplicity, we injected exactly monochromatic waveforms. But there is no strong reason to demand that GWs from magnetars be exactly monochromatic. As explained above, these injections to do not place constraints on type of waveforms that are detectable, but the upper limits are derived from those particular waveforms. Since incoming waveforms may change in frequency, we examine the detectability of such waveforms.

The main effect on detection efficiency comes from the particular choice of frequency bins. With a purely monochromatic signal that falls into exactly one frequency bin (e.g., 150 Hz), the clustering algorithm can recover all of the power from the signal. With a signal between frequency bins (e.g., 149.5 Hz), half of the signal power will be split between two bins. For this case, the clustering algorithm will not recover all of the signal power: it will take a weighted average of the power in the relevant pixels (if the clustering algorithm was changed to use all of the power in the relevant pixels, more noise would also be included). Thus, for the worst-case of signals exactly between frequency bins, only half of the signal power will be recovered. This is borne out in studies of recovery efficiency.

This same problem will occur for non-monochromatic signals. Even if they begin exactly in one frequency bin, over time they change in frequency. If the time it takes the signal to move between frequency bins is much smaller than the attenuation time, we expect to recover about 75% of the injected power, regardless of the starting frequency of the signal. On the other hand, monochromatic signals would vary between 50% and 100% recovery, depending on how close the starting frequency is to the center of a bin.

5.1.5. The Role of Randomness

At a cursory level, this search operates like any other: given a chunk of data, the algorithm quantifies the amount of the desired signal, and compares this to similar data segments where there is known to be no signal. But the random nature of the cluster selection in this algorithm insert another layer of uncertainty. The number of clusters searched over is an important parameter: generating fewer clusters increases the chance of missing signal power, which increases the likelihood of missing the signal. On the other hand, using too many clusters wastes computation time.

We can start by making a rough estimate of the number of possible different clusters. The Bézier curves are parameterized by three points: each having a frequency and time value. Constraining these to be exactly centered on a pixel in the time-frequency map (otherwise the number of possible clusters is infinite), we find $801^3 \times 2450^3 \approx 4$ trillion. While this estimate neglects the constraints we've placed on allowed clusters (minimum length and maximum change in frequency), it clearly shows that we have no hope of exhaustively searching each and every one.

The previous search for GWs from magnetars during Initial LIGO [53] used 30 million clusters, so we start by evaluating how well the pipeline performs with that number of clusters. To see if this number is sufficient, we first look at the distribution of cluster SNR for a background experiment, and one with an injection added (the particular injection here is a ringdown at 150 Hz and a characteristic time of 400 seconds; the injections are fully explained in Section 5.1.7). The results are plotted in Figure 5.3. This injection is successfully recovered, but to ensure that all similar injections would be recovered, we re-reun this experiment with different seeds for the pseudo-random number generator (PRNG) that determines the clusters. The result, plotted in figure 5.4, shows that the search is working properly.

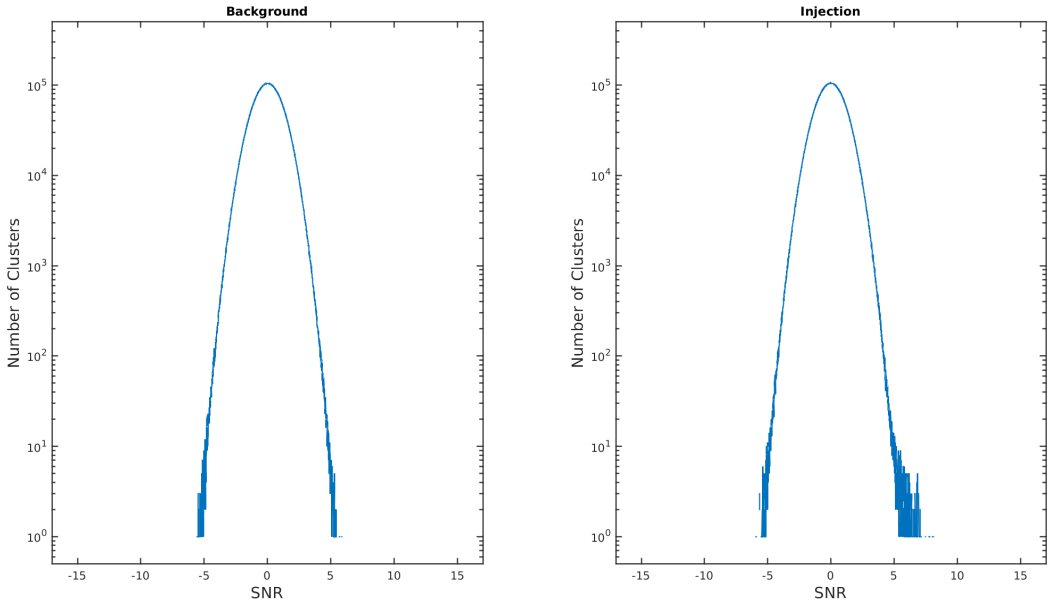

FIGURE 5.3. Histogram of the SNR of clusters for the STAMP search. Left: a background experiment, right: with an injection added. Note the shoulder on the right side of the distribution with the injection.

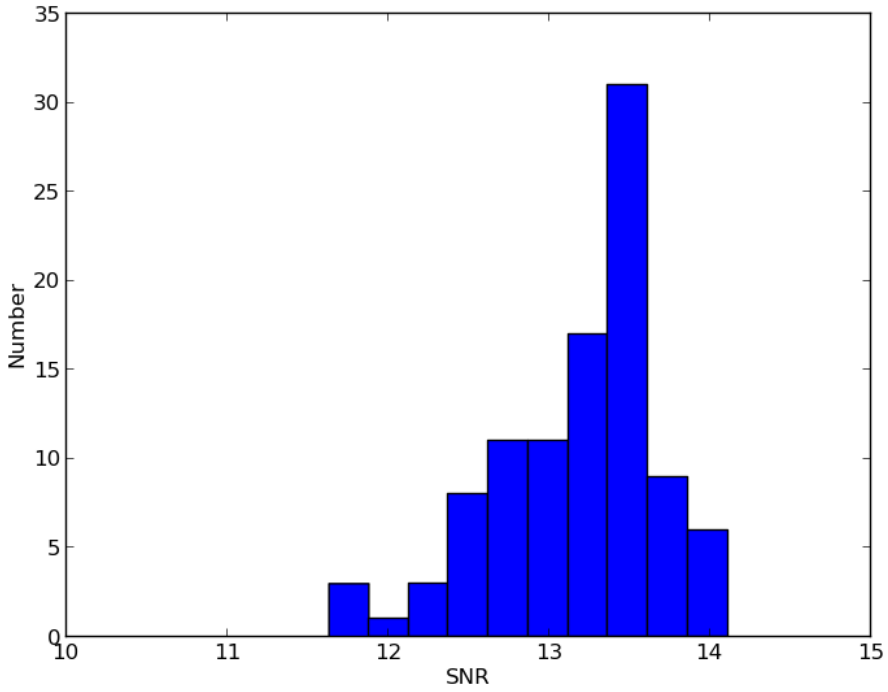

FIGURE 5.4. Running the search on the same data with the same injection but different PRNG seeds yields slightly different results. The mean SNR is 13.2, with a standard deviation of 0.51. Searching over more clusters would tighten this distribution, but require more computational time.

When it comes to estimating the background and sensitivity of the search, the randomness complicates matters again. For each case, we run the search on a chunk of data, either with or without an injection (each of these is considered an "experiment"). But since the particular clusters searched are determined by a PRNG, changing the seed of the PRNG changes which clusters are searched. Since we search a sufficient number of clusters, we know it cannot have a huge effect on the search (i.e. we know all loud signals will be detected), but it can change upper limits. However, as will be shown in Sections 5.1.6 and 5.1.7, since the on-source is only run once (and thus with only one PRNG seed), we can solve

these problems by choosing a particular PRNG seed for use in all background and injection experiments.

5.1.6. Background Estimation

If we assume perfectly Gaussian noise in the detectors, it is relatively straight forward to calculate the rate at which clusters with a particular SNR will appear [63]. Unfortunately, the noise in the detectors is known to not be perfectly Gaussian. Since we're interested in calculating the expected rate of rare events (strong signals), this precludes any confidence in such a calculation. Instead, we will estimate the expected rate of false alarms by analyzing data in which we know there are no GW signals.

In many searches, this is done by *time slides*. This process involves analyzing not-quite-coincident data: if the data from Hanford was taken more than 10 milliseconds after the data from Livingstone, then there this cannot contain a coincident GW signal. This is because the light travel time (and thus the GW travel time, see Chapter II) is about 10 milliseconds. This makes it easy to generate a huge amount of background data: take all of the data from each detector, slide by 15 milliseconds and analyze. Slide by another 15 milliseconds and repeat. With this method, LIGO was able to push the false alarm rate for a GW150914-type event to below 1 per 200,000 years [17].

However, since this search focuses on nearly-monochromatic signals, such a strategy will not work. The signal may well be at the same frequency 15 milliseconds later, so the time slides could contain what appears to be a coincident signal, caused by a real GW. Instead, we divide the background time into 33 separate segments, then use the data from different time segments in each detector.

Thus there can be no contamination from real astrophysical signals, unless those signals last significantly longer than 1600 seconds. Because the properties of the noise tend to change over time, we calculate a separate background for each event. These backgrounds, along with the SNR of the loudest cluster found during the on-source, are plotted in Figure 5.5.

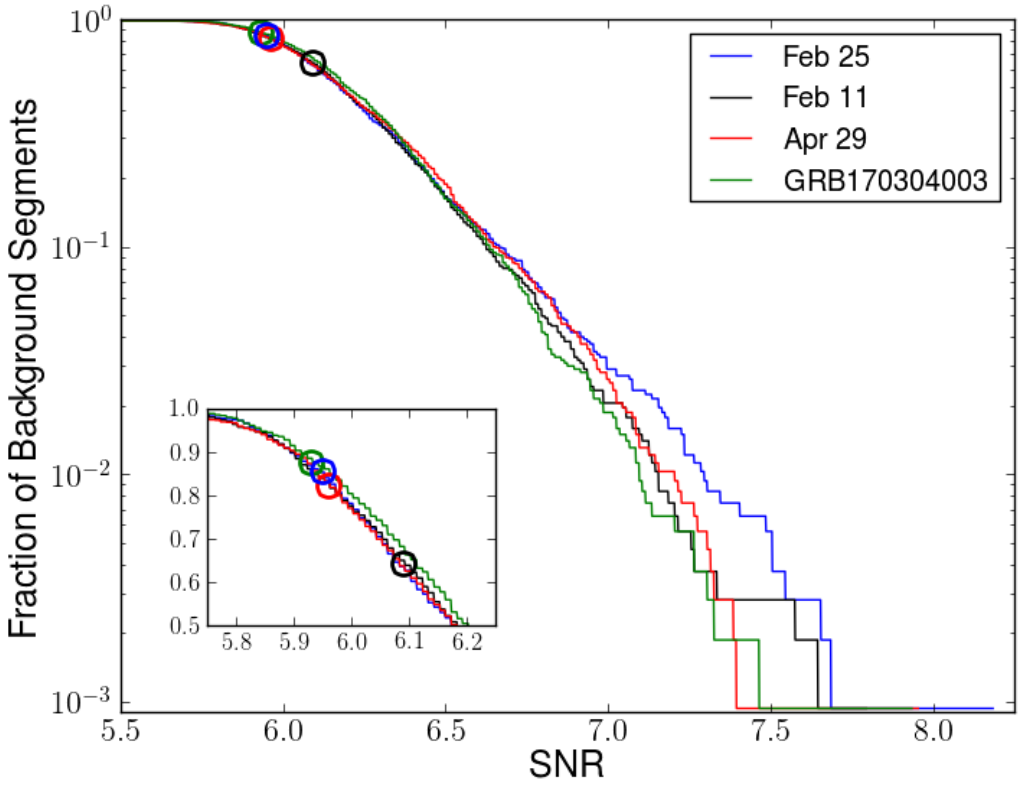

FIGURE 5.5. SNR distribution of the background (lines) and onsource result (open circles) for each burst for the intermediate-duration search. As expected, the background distributions are similar; since many background analyses give louder SNR than the on-source, we conclude that no signal has been detected. Inset: a detailed view of the on-source results.

5.1.7. Injections and Upper Limits

In order to assess the sensitivity of this analysis pipeline, we add software injections of the signal type that we are searching for. In this case, we do not have an exact waveform, but we have a rough timescale (hundreds of seconds) and frequency evolution (monochromatic). These waveforms do not determine the signals that can be detected by this pipeline; the only constraints are on minimum length (50 seconds) and change in frequency (10% of maximum frequency).

For the injections, we used two waveforms, half-sine Gaussians and ringdowns (exponentially decaying sine waves), each at five frequencies (55, 150, 450, 750, and 1550 Hz) and two characteristic times (150 and 400 sec).

Since the search is computationally intensive and a large number of injections are required to obtain good upper limits, we use an algorithm called Singletrack to reduce the computation required. Instead of running the search on all 30 million randomly selected clusters for every injection trial, we run the full search, with fixed random seed, on only a small number for each waveform. From these runs, we extract the most commonly selected clusters, and search on only these clusters in order to obtain the upper limits.

To test the effectiveness of this strategy, we analyze the SNR recovered by this method versus running the standard search. The results are plotted in Figure 5.6. Because this method requires searching over the same clusters in each injection run, there is some concern that we may be anomalously (in)sensitive to a particular injection because of the choice of seed. But as we saw in Section 5.1.5, we are searching enough clusters that this effect should smaller than about 1 SNR. Note that, by using the same random seed for the on-source search, we guarantee that

the results found by these injection studies are reflective of the on-source search's sensitivity.

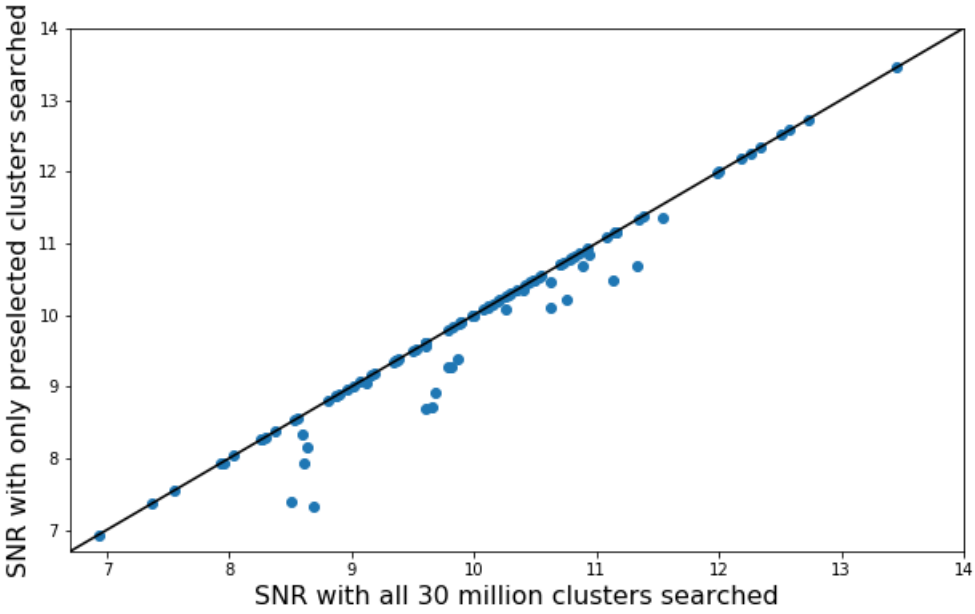

FIGURE 5.6. Singletrack's effectiveness in recovering injections.

In setting the upper limit, we seek to determine the minimum amplitude signal that can be reliably recovered by this search. Here there are two terms to define: "reliably" and "recovered." Though there are many defensible choices, we choose to define an injection as "recovered" if Singletrack produces more SNR than the loudest on-source event. Using this definition, we can produce recovery efficiency curves like Figure 5.7. As for "reliably", searches in LIGO often report recovery efficiency values of 50% or 90%. For this search, we use 50%.

5.1.8. Polarization

For a GW source on a particular point in the sky, how would the LIGO detectors react to an incoming GW? The answer depends on the polarization of

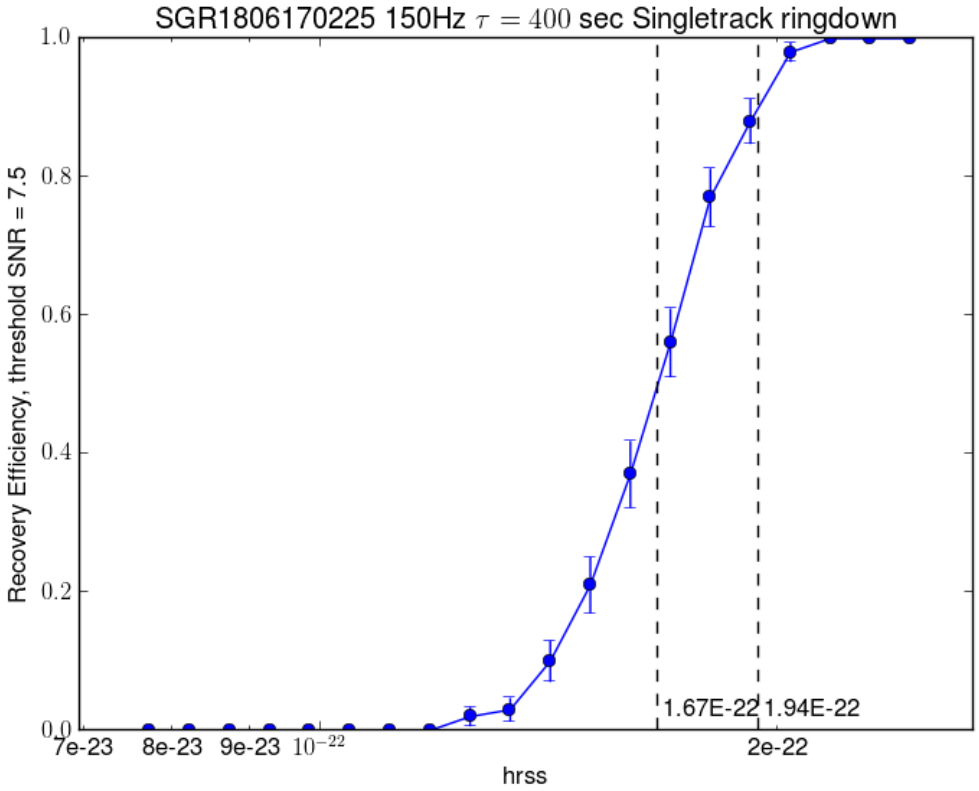

FIGURE 5.7. Recovery efficiency curve for one of the waveforms injected.

the waves. As discussed in Chapter 1, GWs come in two polarizations, + and ×. For gravitational waves from the zenith, the detectors are very sensitive to +, but completely insensitive to ×. Since this is a triggered search, we know the sky location of any GWs, so we can calculate the sensitivity to both polarizations. However, we do not know the polarization of the incoming GWs. If they are due to an oscillating quadrupole, then they will be elliptically polarized, following the equations (derived in Appendix A.1):

$$\begin{aligned} h_+ &= \frac{h_0}{2}(1+\cos^2\iota) \\ h_\times &= h_0 \cos\iota \end{aligned} \tag{5.5}$$

In addition, the SNR of each pixel is calculated using the cross power between the two detectors. This results in a complicated expression for the relationship between polarization and cross power. For elliptically polarized GWs, the result is [60, Eq. A48]:

$$\begin{aligned}\langle \hat{Y}\big(t; f, \hat{\Omega}, \iota, \psi\big)\rangle =& 2\mathrm{Re}\Big[\frac{1}{2}\frac{\delta_{ff_0}}{2N_s}\Big(F_I^+F_J^+\left[A_+^2\cos(2\psi)^2 + A_\times^2\sin(2\psi)^2\right] \\ &+ F_I^+F_J^\times\left[(A_+^2 - A_\times^2)\cos(2\psi)\sin(2\psi) - iA_+A_\times\right] \\ &+ F_I^\times F_J^+\left[(A_+^2 - A_\times^2)\cos(2\psi)\sin(2\psi) + iA_+A_\times\right] \\ &+ F_I^\times F_J^\times\left[A_+^2\sin(2\psi)^2 + A_\times^2\cos(2\psi)^2\right]\Big) \\ &e^{-2\pi i f(\hat{\Omega}\cdot\Delta\vec{x}_{IJ}/c)}\tilde{Q}_{IJ}(t; f, \hat{\Omega}, \iota, \psi)\Big]\end{aligned} \tag{5.6}$$

The last two terms are the light travel time correction and the filter function (which were discussed briefly above), respectively. It is instructive to plot this, without taking the real part and sans filter function/travel time correction, parametrically in the complex plane. Figure 5.8 shows the result for the sky location of SGR 1806-20 during the February 25 short burst.

It may be surprising that the cross power usually has an imaginary component. We can see that this is due to the fact that the detectors do not have the same orientation: the imaginary part of the cross power is $A_+A_\times\big(F_I^\times F_J^+ - F_I^+F_J^\times\big)$, and thus will be zero if the detectors have the same orientation (and therefore the same antenna functions). More concretely, this occurs because of two effects: first, differing antenna functions mean that the two detectors will treat each polarization differently, producing a different signal. Second, differing orientations mean that they will not even agree on the definition of the polarizations. And

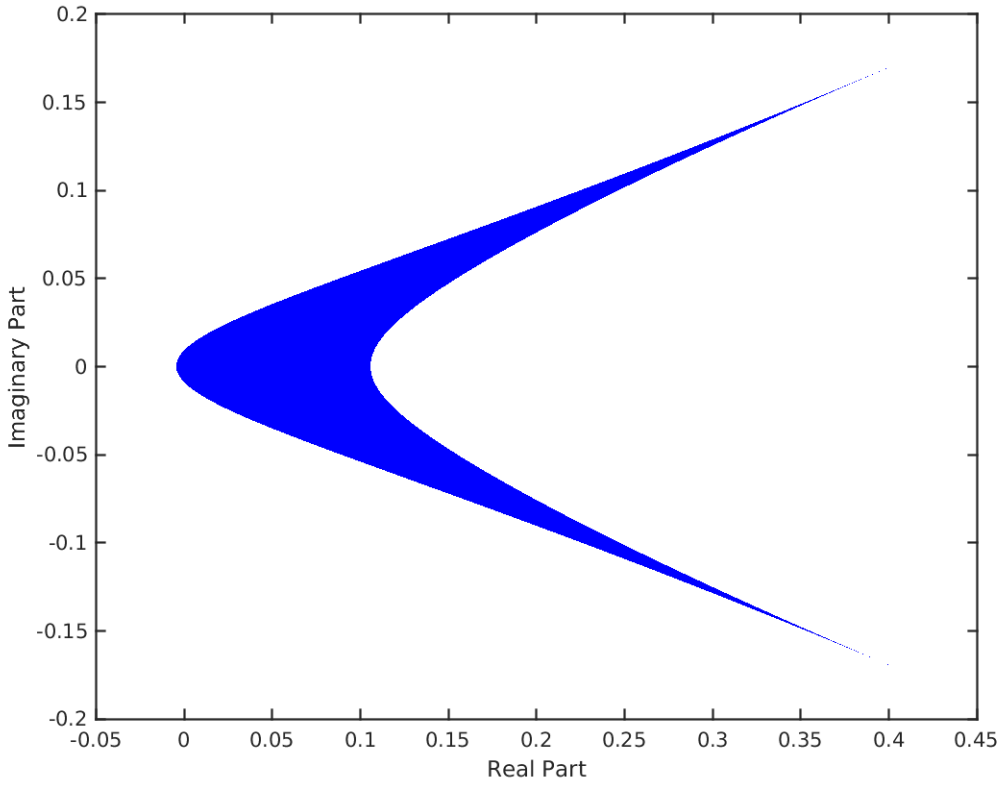

FIGURE 5.8. Complex-valued cross power over all source polarizations for a GW signal from SGR 1806-20 during the February 25 short burst. The units are the fraction of power recovered compared to ideally oriented detectors and source polarization. The differing orientations of the detectors mean that this plot will never reach the ideal value of 1, instead approaching about 0.96.

because each detector produces a single scalar strain value, these disagreements can not be untangled.

The broad range of magnitudes is also striking. Partly this is due to the different antenna functions for the two polarizations, but a large effect is due to the pattern of radiation from a quadrupole. As discussed in Chapter II, pure quadrupolar radiation, analogously to the more familiar dipolar radiation of electromagnetism, is not spherically symmetric in its power output. If the axis of

rotation is pointed directly toward (or away from) Earth, we receive much more GW energy than if the axis of rotation is perpendicular to our line of sight.

Now consider the effect of detector noise, filter function, and taking the real part: detector noise is assumed to be uncorrelated, meaning that the phase of the noise in each pixel should be random. The phase of the filter function, combined with taking the real part, chooses which phase of the cross power to be understood as possibly astrophysical. However, elliptically polarized signals present a problem: the phase of the cross power depends on the polarization. Since this is not known, we have no way to know which is the ideal filter function. And with a non-ideal filter function we would be throwing away signal power, and thus SNR, reducing the sensitivity of the search.

But without knowing the polarization of the incoming GWs, we cannot know what the ideal filter function is. In fact, it is possible for the cross power to have any complex phase, so no filter function can hope to recover waves with any polarization. However, as shown in Figure 5.8, signals that result in a large amount of cross power cluster around two phases. These phases can be deduced from the cross power function plotted. The ends of the boomerang occurs at $\iota = 0, \pi$: this must be the case because changing the angle ψ can only change the real part, but changes nothing at $\iota = 0, \pi$ besides the initial phase. Taking $\iota = 0$ in Equation 5.6, $A_+ = A_\times = h_0$, so we find:

$$\begin{aligned}\langle \hat{Y}\big(t; f, \hat{\Omega}, \iota, \psi\big)\rangle =& 2h_0^2 \mathrm{Re}\Big[\frac{1}{2}\frac{\delta_{ff_0}}{2N_s}\Big(F_I^+F_J^+ - iF_I^+F_J^\times + iF_I^\times F_J^+ + F_I^\times F_J^\times\Big) \\ & e^{-2\pi i f(\hat{\Omega}\cdot\Delta\vec{x}_{IJ}/c)}\tilde{Q}_{IJ}(t; f, \hat{\Omega}, \iota, \psi)\Big]\end{aligned} \tag{5.7}$$

The phase is then:

$$\phi = \arctan\left(\frac{F_I^{\times}F_J^{+} - F_I^{+}F_J^{\times}}{F_I^{+}F_J^{+} + F_I^{\times}F_J^{\times}}\right) \tag{5.8}$$

For $\iota = \pi$, this changes by an overall sign.

In light of this analysis, we must re-evaluate the choice of filter function. Following other analyses using this software pipeline, we chose the unpolarized filter function, taking only the real part (as illustrated in Figure 5.8). Instead of choosing this middle ground, we could instead run the analysis twice, running along the phases calculated above. However, this approach suffers from two problems that reduces its efficacy: first, this will increase the noise. Second, it produces the greatest gains when the antenna factors are poor and the chances of making detections are lowest. So for this analysis, the unpolarized filter functions will be used.

5.2. X-Pipeline

X-Pipeline is a software package designed to search for short-duration gravitational wave signals in multiple detectors, and includes automatic glitch rejection, background calculation, and software injection processing (for details, see [54]). It forms coherent combinations from multiple detectors, thus making it relatively insensitive to non-GW signals, such as instrumental artifacts. X-Pipeline is used primarily to search for GWs coincident with γ-ray bursts (GRBs), but is suitable for any short-duration coherent search.

X-Pipeline takes a likelihood approach to estimating the GW energy found in each time-frequency pixel. It models the data collected at the detectors as a combination of signal and detector noise, then uses a maximum likelihood technique to calculate the estimated GW signal power in each time-frequency pixel.

For clustering, X-Pipeline selects the loudest 1% of pixels and connects neighboring pixels. Each connected group is a cluster, and the clusters are scored based on the likelihood described in the previous paragraph. We want to pick the time length of the pixels in the time-frequency map so that signal is present in the smallest number of time-frequency pixels, as this will recover the signal with the highest likelihood. Since we do not have a model for the waveform we are searching for, we use multiple pixel lengths and run the clustering algorithm on all of them. After clusters are identified, X-Pipeline identifies which candidate clusters are likely glitches by comparing three measurements of signal energy: coherent energy consistent with GWs, coherent energy inconsistent with GWs, and sum of the signal energy in all detectors (referred to as incoherent energy). GW signals can be differentiated from noise by the ratio of coherent energy inconsistent with GWs to the incoherent energy (see Sections 2.6 and 3.4 of [54] for full details).

The primary target of this search are GWs produced from the excitation of the magnetar's fundamental mode, which are primarily dampened by the emission of GWs [64, 65]. We have chosen parameters for X-Pipeline to search for signals a few hundred milliseconds long. The search window begins 4 seconds before the γ-rays arrive and ends 4 seconds after. The frequency range for the short-duration search is 64–4000 Hz, and the pixel lengths are every factor of 2 between 2 s and 1/128 s, inclusive.

5.3. Results and Upper Limits

No signals were found by either the short- or intermediate-duration searches. We present the results and upper limits on GW strain and energy for each analysis below.

5.3.1. Short-Duration Search Upper Limits

No significant signal was found by X-Pipeline. After glitch rejection, the most significant cluster for the February 25 burst had a p-value of 0.63.

Following the previous f-mode search [35], we injected white noise bursts (frequencies: 100–200 Hz and 100–1000 Hz; durations: 11 ms and 100 ms), and ringdowns (damped sinusoids, at frequencies: 1500 Hz and 2500 Hz; time constants: 100 ms and 200 ms), and chirplets (chirping sine-Gaussians; this differs from the prior search, which used sine-Gaussians). The best limits for the white noise bursts were for the 11 ms long bursts in the 100–200 Hz band, at 2.1×10^{44} erg in total isotropic energy and $h_{\rm rss}$ (root sum squared of the GW strain) of 5.6×10^{-23} at the detectors. We are most sensitive to ringdowns at 1500 Hz and a time constant of 100 ms, with an upper limit of 2.3×10^{47} erg and $h_{\rm rss}$ of 1.9×10^{-22}. Directly comparing the $h_{\rm rss}$ limits to [57], we see that limits have improved by roughly a factor of 10, though the ringdowns we used had slightly different parameters. Comparing to [35], which provided only energy upper limits assuming a distance of 3.6 Mpc, we see an improvement of factor of 60 after correcting for the larger distance. This corresponds to roughly a factor of 8 improvement in $h_{\rm rss}$ limits. A full list of upper limits for the waveforms tested is found in Table 5.2.

5.3.2. Intermediate-Duration Search Upper Limits

To calculate upper limits, we add software injections of two waveforms (half-sine Gaussians and exponentially decaying sinusoids) at five frequencies (55, 150, 450, 750, and 1550 Hz) and at two timescales (150 seconds and 400 seconds). Reported upper limits are for 50% recovery efficiency, where recovery is defined as finding a cluster, at the same time and frequency as the injection, with SNR greater

Injection Type	Frequency (Hz)	Duration/ τ (ms)	$h_{\rm rss}$	Energy (erg)
chirplet	100	10	5.42×10^{-23}	8.49×10^{43}
chirplet	150	6.667	4.93×10^{-23}	1.58×10^{44}
chirplet	300	3.333	5.29×10^{-23}	7.27×10^{44}
chirplet	1000	1	1.15×10^{-22}	3.82×10^{46}
chirplet	1500	0.6667	1.69×10^{-22}	1.81×10^{47}
chirplet	2000	0.5	2.32×10^{-22}	5.92×10^{47}
chirplet	2500	0.4	3.06×10^{-22}	1.56×10^{48}
chirplet	3000	0.3333	3.96×10^{-22}	3.65×10^{48}
chirplet	3500	0.2857	5.30×10^{-22}	8.51×10^{48}
white noise burst	100–200	11	5.57×10^{-23}	2.09×10^{44}
white noise burst	100–200	100	7.88×10^{-23}	4.15×10^{44}
white noise burst	100–1000	11	1.00×10^{-22}	1.04×10^{46}
white noise burst	100–1000	100	1.83×10^{-22}	3.55×10^{46}
ringdown	1500	200	1.89×10^{-22}	2.25×10^{47}
ringdown	2500	200	2.87×10^{-22}	1.37×10^{48}
ringdown	1500	100	1.89×10^{-22}	2.25×10^{47}
ringdown	2500	100	2.80×10^{-22}	1.30×10^{48}

TABLE 5.2. Upper limits on isotropic energy from the short-duration search for the February 25 burst from SGR 1806-20. For white noise bursts, we give the duration of the injection; for the other waveforms, the characteristic time. All limits are given at 50% detection efficiency, meaning that a signal with the given parameters would be detected 50% of the time.

than that of the on-source (for the February 25 event, it was 6.09). Full results are shown in Table 5.3.

Due to the improved sensitivity of Advanced LIGO, we are able to set strain upper limits about a factor of 10 lower than the previous search during Initial LIGO [1], see Fig. 5.9. Unlike the previous search, this search showed little difference in $h_{\rm rss}$ sensitivity between the two injection lengths. STAMP has been refined to improve PSD estimation, which explains the small gap between the injection timescales for this search.

Frequency (Hz)	Tau (sec)	$h_{\rm rss}$		Energy (erg)	
		Half Sine-Gaussian	Ringdown	Half Sine-Gaussian	Ringdown
55	400	2.29×10^{-22}	2.43×10^{-22}	1.82×10^{44}	2.06×10^{44}
55	150	1.97×10^{-22}	2.11×10^{-22}	1.35×10^{44}	1.55×10^{44}
150	400	1.32×10^{-22}	1.37×10^{-22}	4.52×10^{44}	4.86×10^{44}
150	150	1.14×10^{-22}	1.22×10^{-22}	3.37×10^{44}	3.89×10^{44}
450	400	1.69×10^{-22}	1.79×10^{-22}	6.62×10^{45}	7.47×10^{45}
450	150	1.78×10^{-22}	1.83×10^{-22}	7.43×10^{45}	7.83×10^{45}
750	400	2.56×10^{-22}	2.70×10^{-22}	4.21×10^{46}	4.69×10^{46}
750	150	2.11×10^{-22}	2.37×10^{-22}	2.87×10^{46}	3.61×10^{46}
1550	400	5.86×10^{-22}	6.22×10^{-22}	9.21×10^{47}	1.03×10^{48}
1550	150	4.38×10^{-22}	4.58×10^{-22}	5.16×10^{47}	5.62×10^{47}

TABLE 5.3. Upper limits on GW strain and energy from the intermediate-duration search for the February 25 burst from SGR 1806-20. All limits are at 50% detection efficiency.

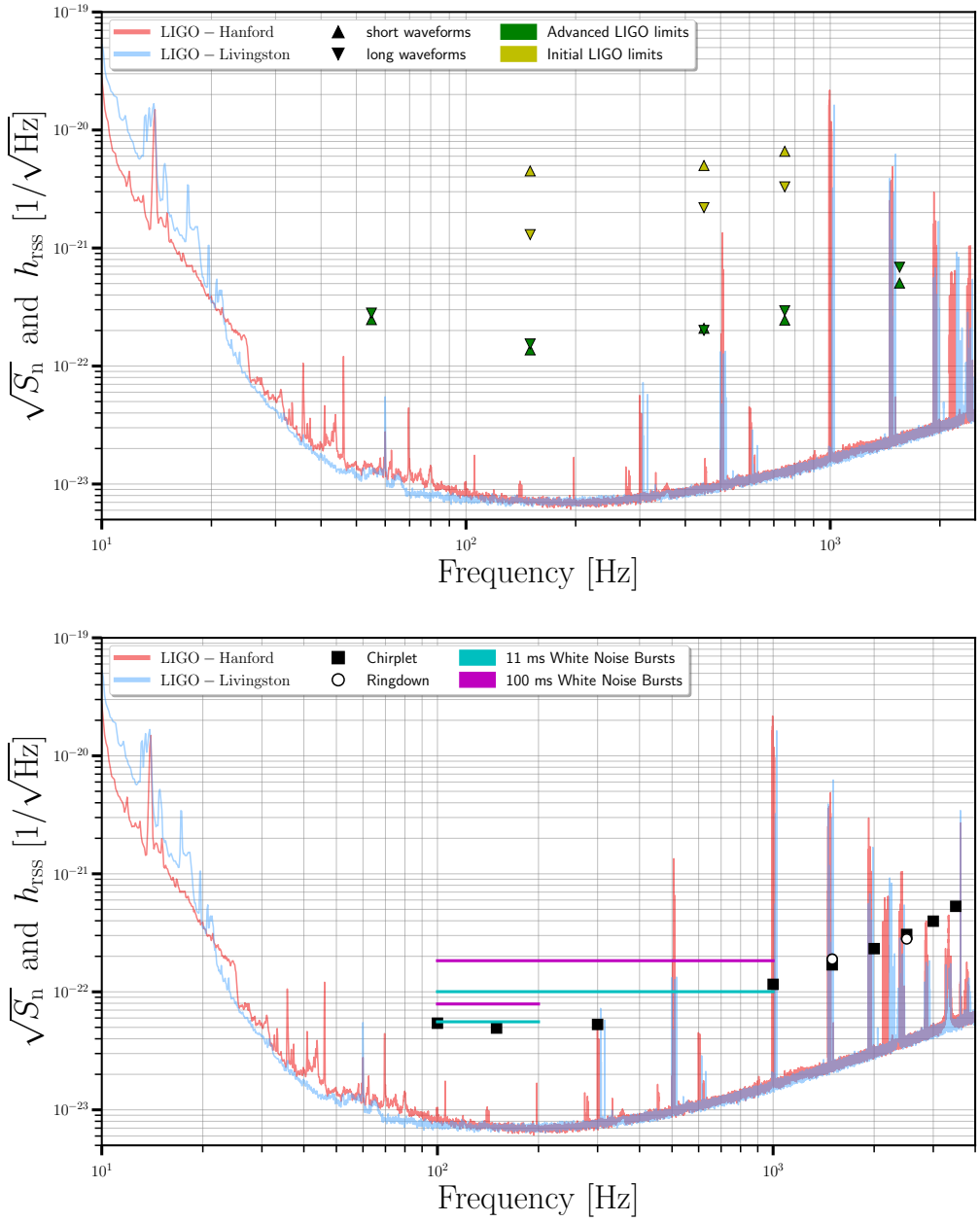

FIGURE 5.9. Upper limits for the the intermediate-duration search (above) and short-duration search (below), along with the sensitivity of the detectors. We plot $h_{\rm rss}$ at 90% detection efficiency for the intermediate-duration search here to allow direct comparison to published figures for the previous search in Initial LIGO [1]. Short-duration limits are for 50% efficiency as before. The Advanced LIGO search limits are for the February 25 burst from SGR 1806-20 during the second observing run, and detector sensitivity is calculated from data during the analysis window.

5.4. Astrophysical Implications

This search has set the strongest upper limits on short- and intermediate-duration GW emission associated with magnetar bursts. The energy limits, which are as low as 10^{44}–10^{47} erg, are now well below the EM energy scale of magnetar giant flares (10^{46} erg). The short bursts analyzed here were much weaker than a giant flare (see Table 5.1), so for these bursts the limit is much larger than the observed electromagnetic energy. In addition, these limits assume ideal orientation of the magnetar (both sky position and polarization of produced GWs). The impact of other polarizations on the intermediate-duration search are discussed above, and plotted in Figure 5.10.

The upper limits set by this search are still far above the GW energy from f-mode excitation during a giant flare according to [46], unless the magnetic field strength is far higher than currently accepted value of 2×10^{15} G [2]. Using Equation 2 from [46], f-mode GW emission from a giant flare would be about 1.4×10^{38} erg. A surface magnetic field of 1.8×10^{16} G would be required to reach the best upper limit found with the short-duration source.

As the LIGO detectors increase in sensitivity, these upper limits will improve, and will be well-positioned to place meaningful limits on emitted GW energy in the event of a future nearby magnetar giant flare. For reference, the distances to some nearby magnetars are shown in Table 5.4. Analysis of GW waveforms from magnetar would give great insight into the inner workings of both magnetars and neutron stars in general.

Thanks to the detection of the merger of two neutron stars in GW170817, the study of neutron stars through GWs has already begun. From the nature of neutron star in equilibrium to its behavior during cataclysmic merger events, the

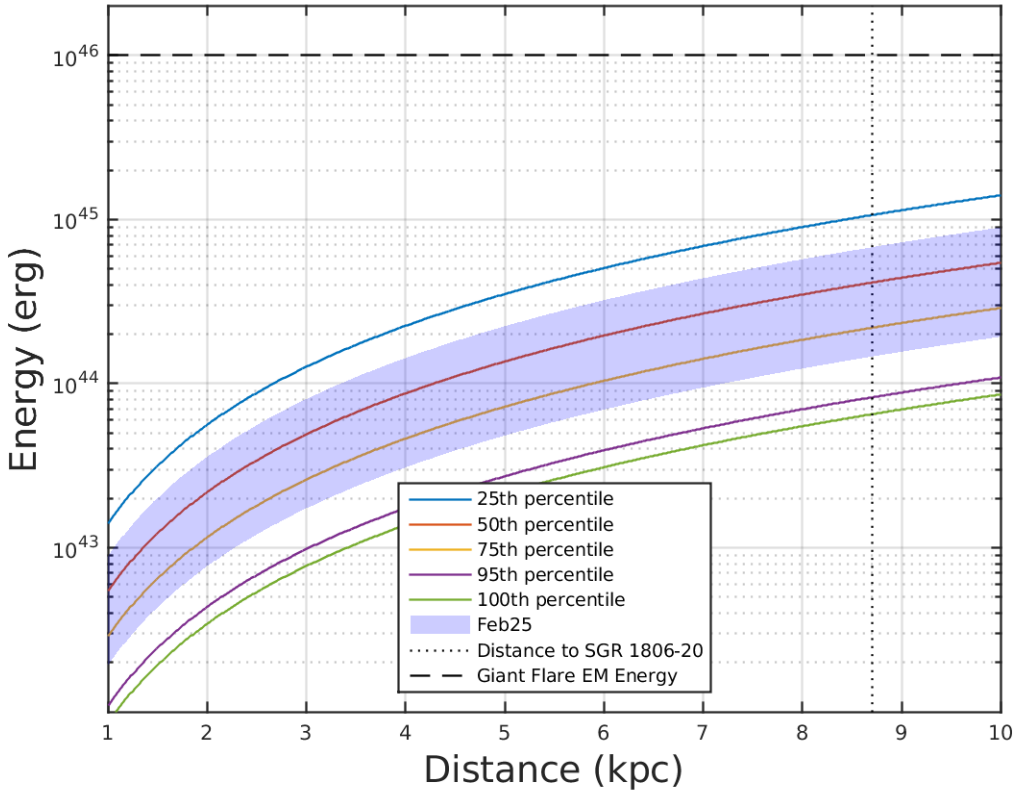

FIGURE 5.10. Minimum detectable energy for the intermediate-duration search vs distance for SGR 1806-20 for varied sky locations and GW polarizations at 55 Hz. The lines show how the variation in sky position (caused by the earth's rotation) and polarization (assumed to be random) affects the sensitivity; the purple 95th percentile line indicates that the network sensitivity will be better than indicated by that line only 5% of the time. The shaded region indicates the sensitivity to GW energy from the burst on February 25. Here, the uncertainty is only due to the unknown polarization.

Magnetar	Distance (kpc)
Swift J1822.31606	1.6
SGR 0418+5729	2
SGR 0501+4516	2
1E 2259+586	3.2
XTE J1810197	3.5
4U 0142+61	3.64
1RXS J170849.0400910	3.8
CXOU J164710.2455216	3.9
Swift J1834.90846	4.2
1E 1547.05408	4.5

TABLE 5.4. List of all magnetars within 5 kpc of Earth, along with their distances. SGR 1806-20 is 8.7 kpc from Earth. All data from [2]

window is already being opened. This work, as well as ways that the searches outlined in this chapter can be adapted for the case of BNS merger events, is the topic of the next chapter.

CHAPTER VI

GW170817 AND THE PROSPECT OF DETECTING POST-MERGER SIGNALS

This chapter contains material from an upcoming paper, co-authored with Michael Coughlin, Scott Coughlin, James A. Clark, and Andres Bauswein, titled "The missing components: boosting the sensitivity of post-merger gravitational-wave searches using principal component analysis."

On August 17, 2017, the inspiral and coalescence of two neutron stars was detected for the first time [8]. The neutron stars were between 1.17 and 1.6 $M_\odot$, with total mass of 2.74 $M_\odot$, and at a distance of 40^{+8}_{-14}Mpc. The merger was followed by GRB 170817A 1.7 seconds later, ushering in the era of multi-messenger gravitational wave astronomy.

The detection was complicated by a large glitch which occurred in the Livingston detector during the inspiral phase (and before the merger). This caused online searches to veto the event from that interferometer, but the Hanford data showed a clear signal. Initial data analysis efforts dealt with the glitch through gating, where the data during the glitch time is set to zero (with windowing on either side so as to not introduce large artifacts from the gating). Later, a team used a Bayesian inference software package called BayesWave [66] to reconstruct the Livingston data without the glitch. This cleaned data was then used for all published results, and will be used in the next section.

In Section 6.1, we show how the GW signal for this event can be recovered by adapting the STAMP search algorithm discussed in Chapter V. The rest of the chapter covers the possibility of a GW signal produced after the merger of two neutron stars: In Section 6.2, we discuss the current understanding of post-merger astrophysics, expectations for GW signals, and a recent paper purporting to

have found such a signal following GW170817. In Section 6.3, we explain how the STAMP search can be adapted for such signals and we find no such post-merger signal in the data. Finally, Section 6.4 explores an adaptation of the X-Pipeline software package designed to search for post-merger signals.

6.1. Detection of the GW Signal

The two best pipelines for CBC analysis recovered a signal roughly 60 seconds long [8], making this signal long enough to be visible to STAMP. To tailor the search to a BNS-type signal, a few adjustments were needed.

Since the signal length is shorter than for the magnetar intermediate duration search, the time-frequency pixels should be shorter. We chose to use 1 second long pixels, still with an overlap of 50% (down from 4 seconds).

To determine the ideal frequency range, we consider the signal morphology of a BNS signal: as the inspiral progresses, the frequency increases as the orbit shrinks. With smaller orbits, the GW luminosity increases which further increases the rate of orbital decay. The result is that little signal energy is emitted at higher frequency. So, while parameter estimation pipelines estimated a peak frequency around 3 kHz, little signal energy is found over 300 Hz. In addition, because the signal frequency increases very quickly, the signal power will be spread among many time-frequency pixels, making it difficult for STAMP to find. So, we set the maximum frequency at 300 Hz.

Next we must consider where to set the low frequency limit. Going back in time from the merger, the signal extends down to essentially zero frequency, though the signal weakens and the detector sensitivity worsens. Still, the signal is clearly visible in spectrograms to at least 40 Hz, so we set the lower limit to 30 Hz.

Finally, we ran the search using clusters modeled for signals from compact binary coalescences ("CBC clusters") in addition to the randomly selected Bézier curves. The SNR time-frequency map, both with the glitch and with the glitch removed, can be found in Figure 6.1.

The CBC clusters recovered the signal with an SNR of 19.0, while the Bézier clusters found a loudest cluster with an SNR of 13.2. By treating this as a triggered search on GRB 170817A, we can estimate the background in the same way as for the magnetar search. Out of 1,000 background experiments, the loudest background cluster found for the CBC clusters and Bézier clusters was 7.3 and 9.0, respectively. Since this is far lower than the on-source, we can conclude that the data contains a real signal, with a false alarm probability[1] of under 0.1%. Running more background experiments would decrease the false-alarm probability, but since searches designed for CBC signals have already proven this signal to be astrophysical, there is little motivation to use more computational resources to do so. Plots of the backgrounds, compared with the on-source recovery, are shown in Figure 6.2.

6.2. Post-Merger Astrophysics

With Binary Black Hole mergers (BBHs), the post merger physics is relatively straight-forward: the two black holes merge into a larger one, releasing a huge burst of GWs. Barring any unforeseen effects from quantum gravity no light can escape, which is consistent with the BBH observations so far. What is left is an isolated black hole, with properties dictated by general relativistic conservation laws.

[1]We define 'false alarm probability' as the probability that a segment of data with no GW signal will be assigned an SNR louder than the loudest background experiment.

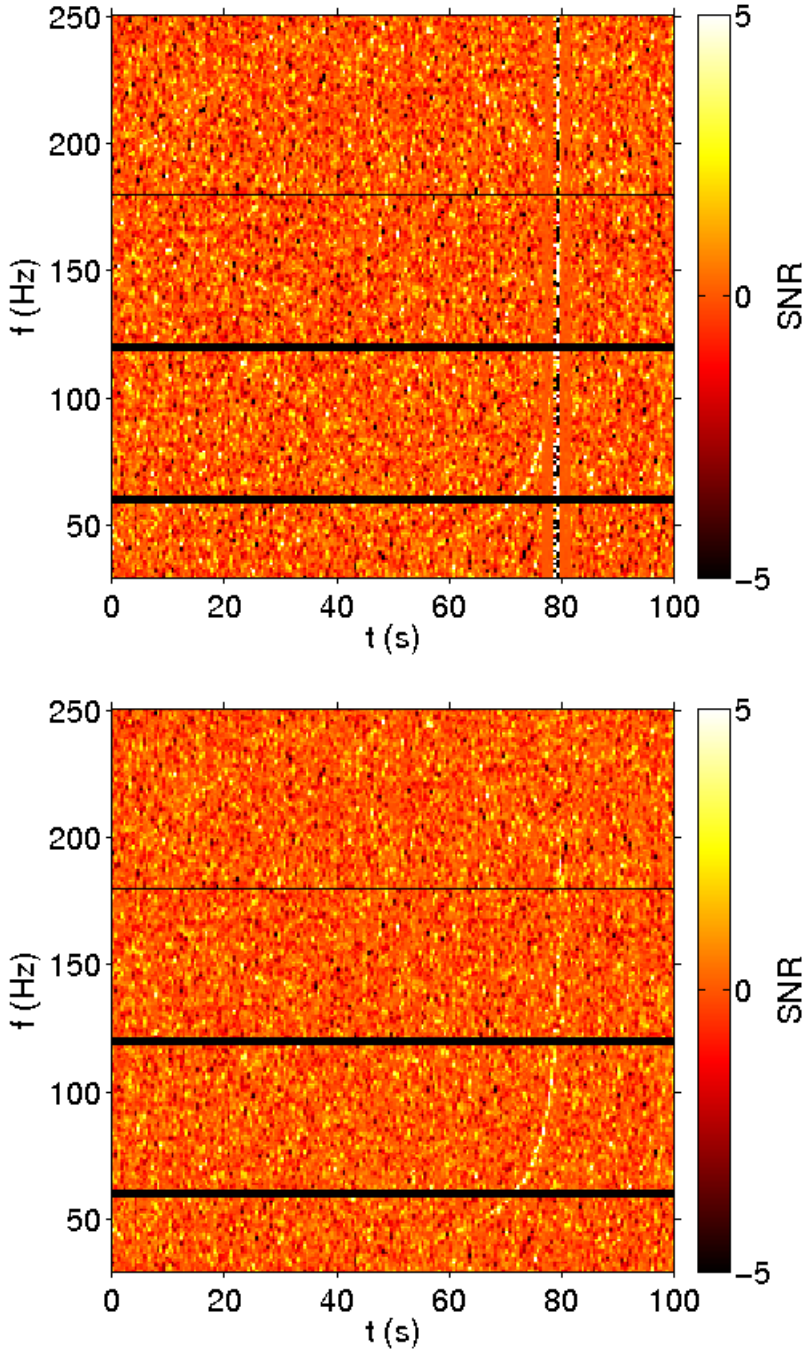

FIGURE 6.1. SNR maps for GW170817. Above: before data cleaning. Below: with glitch removal via BayesWave. Even before glitch removal, the signal is recovered with SNR of 11, well above the loudest background.

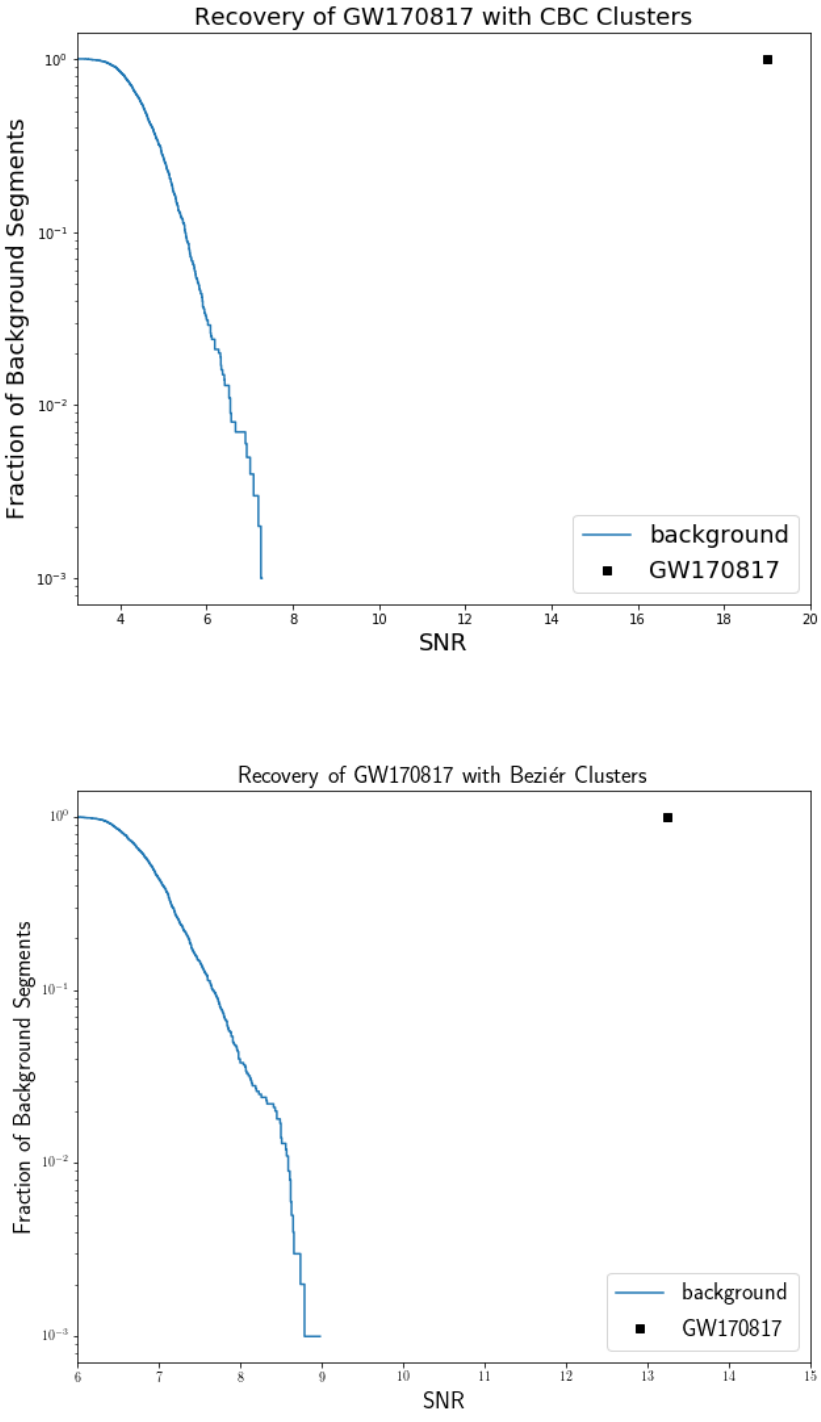

FIGURE 6.2. Comparison of the recovery of GW170817 with STAMP to background.

Neutron star mergers are not as simple. Unlike black holes, which are point-like singularities, neutron stars are extended in space and are, at some level, "squishy." Late in the inspiral phase, the tidal forces on each neutron star causes them to deform slightly (see [67] for estimation of this effect on GW170817). Furthermore, the end result of the merger is not clear. If the mass is large enough, a prompt collapse to a black hole is expected, but the amount of mass required is not known precisely. Stable, non-spinning neutron stars are supported against further gravitational collapse by the strong nuclear force, but this is only feasible up to some mass limit, called the Tolmann-Oppenheimer-Volkoff (TOV) limit. Above that limit, the gravitational force dominates and collapse to a black hole cannot be avoided. The primary factor in determining the exact value of the TOV limit is the neutron star Equation of State (EoS), the relationship between density and pressure. A "soft" EoS is one where neutron star matter is very compressible (the density increases quickly with increasing pressure) and would result in a lower maximum neutron star mass. Though the exact value of the TOV limit is not currently known, two neutron stars above 2 $M_\odot$ have been observed [68, 69], setting the lower limit.

The question of whether the remnant is above the TOV limit is not the end of the story, however. In addition to the support provided by neutron star pressure, centrifugal force provided by rotation and forces due to differential rotation can also protect against collapse. This allows for the possibility of supramassive neutron stars—those with a mass larger than the limit for non-rotating neutron stars—as the product of the merger. The evolution of these objects is a subject of current research, and will be further discussed below.

Another effect expected from BNS mergers is the ejection of some neutron star material. This happens due to two effects: first, the tidal forces cause some material to be thrown from the stars and form an accretion disk. Second, the collision of the surfaces of the two neutron stars can cause some matter to be ejected [70]. The huge flux of free neutrons allows the production of heavy elements (those heavier than iron) through the rapid neutron capture process (or r-process) [71]. This occurs when neutron capture happens more quickly than other radioactive processes which would ordinarily result in fission or α-particle emission. The ejecta cools from the expansion, though it is also heated by the radioactive decay from the r-process nuclei and possibly the remnant star (if it is not a black hole). This bubble of matter, predicted to be visible at optical wavelengths for days after a merger as an afterglow, was observed after GW170817. At first it was dominated by blue to UV wavelengths [72], but rapidly shifted to red and IR [73]. Using these observations, combined with estimates of the total mass and GRB energy, [70] estimated that the TOV limit is about 2.17 $M_\odot$.

6.2.1. Short GRBs

High energy γ-ray bursts (GRBs) have been observed for many years, generally falling into two categories: long GRBs, which last longer than 2 seconds and are thought to be caused by supernovae, and short GRBs (SGRBs), which are shorter than 2 seconds and are strongly believed to come from BNS or NS-BH mergers. SGRBs begin suddenly, which points to a highly compact source. While they have a short peak, some SGRBs have a longer tail lasting $\sim$ 100 seconds, pointing towards a continued source of energy. Since black holes cannot

emit energy, this suggests that the result of the BNS merger does not immediately collapse to a black hole in all cases.

Instead, the two neutron stars might merge together to form a supra-massive neutron star, supported from further gravitational collapse by its rapid rotation. This star could continually provide energy to the cloud of matter surrounding it, producing the extended emission tails and x-ray plateaus seen in some short GRBs [74]. The total mass of the binary that produced GW170817 was 2.74 $M_\odot$ [8]. which is likely above the TOV limit[2]. Thus the remnant would require some mechanism other than neutron degeneracy pressure in order to remain stable, like the centrifugal force provided by rapid rotation.

6.2.2. Magnetars From BNS Mergers

One possible intermediate object is a millisecond magnetar, with a magnetic field strength $\sim 10^{15}$ G [76]. While all magnetars currently known have rotational periods of 2–12 seconds, a millisecond magnetar would rotate on a timescale of milliseconds. To explain the slow and uniform rotation rate of galactic magnetars, scientists have proposed that a highly effective braking mechanism slows their rotation shortly after birth.

Stable neutron stars above the TOV limit fall into two categories: hypermassive and supramassive. The more massive of the two categories, hypermassive neutron stars, are supported by differential rotation. They are expected to collapse quickly, as the differential rotation is halted by internal forces. Supramassive neutron stars, on the other hand, are supported by the centrifugal force caused by their rotation, which is uniform. However, like all neutron stars,

[2]Most EoS models place the TOV limit close to 2 $M_\odot$[75]

they would have a rotating magnetic field that would slow the rotation rate through magnetic torque. Once the rotation slows to the point that the centrifugal force can no longer support the weight of the star, it collapses. This is likely to happen within about 12 hours, and may emit GWs before doing so [77].

6.3. Post-Merger Signals

There has been much work on models of post-merger GW emission as well as searches for such signals. The LVC paper found no signal [78]. However, there was a paper published that purported to find a signal in the data that the LVC released to the public [79] (hereafter vP-DV). In particular, the paper reported the existence of an anti-chirping signal, which was used to explain the central engine of the GRB that occurred shortly after the BNS merger.

Just as we adapted STAMP to search for the BNS signal, we can do the same for this signal. The SNR map produced by STAMP starting just before the merger is shown in Figure 6.3. Here, unlike the magnetar search, we have a short window and strong priors on the waveform provided by vP-DV: We search for waveforms of the form $f(t) = (f_{\max} - f_0)e^{-\alpha t} + f_0$. In addition to the three parameters shown in the equation $(\alpha, f_0, f_{\max})$, we vary the start time and the length of the cluster. Varying the length of the cluster is necessary to recover the maximum SNR: including pixels after the signal has decreased too far will decrease the SNR of the cluster. As for the values of the parameters, we have a strong prior on the start time: vP-DV's theory requires that the anti-chirp begins before the GRB, giving a 1.7 second window.

Furthermore, vP-DV reported the exact parameters of their recovered signal. In attempting to verify this signal, we search for both this particular cluster as well

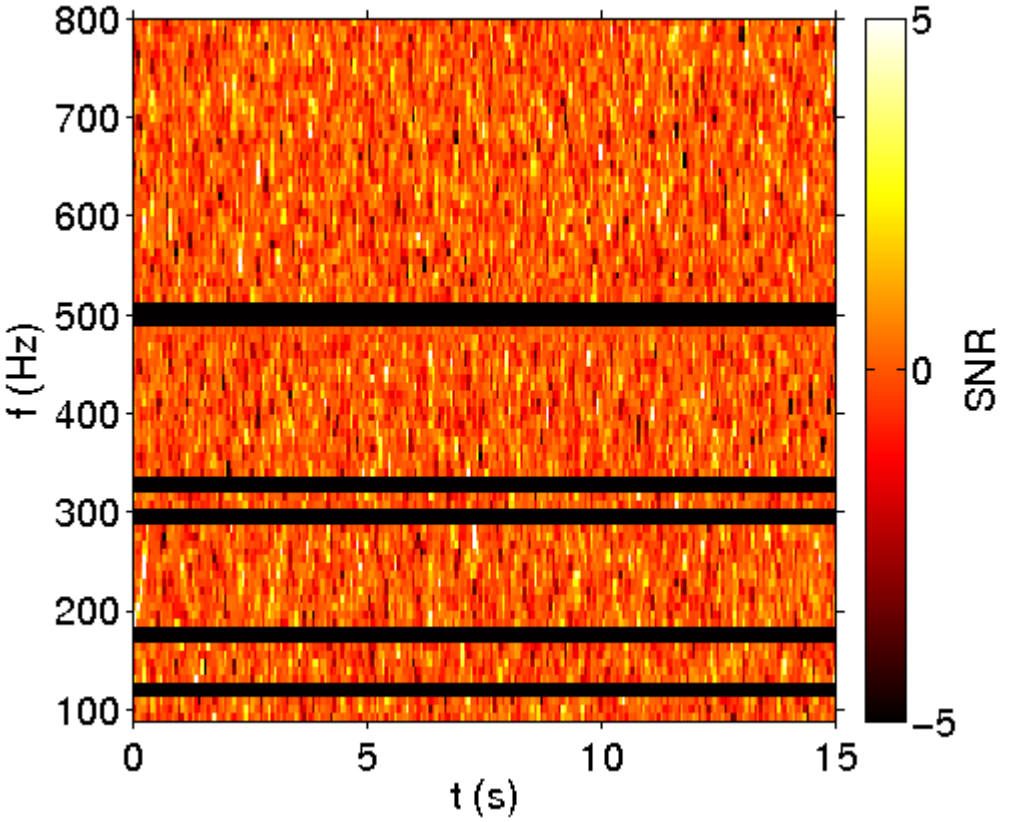

FIGURE 6.3. SNR time-frequency map, with 1/8 sec pixels, starting just before the merger of GW170817. The end of the inspiral is visible at the start of the window, beginning at about 200 Hz. No post-merger signal is apparent, and STAMP confirms that none is present.

as clusters of the same form with different parameters. The parameters searched over are noted in Table 6.1.

	f_0	$f_{\max}$	α	t_{start}
vP-DV	98	650	0.33	1.1
Narrow	92–104	640–650	0.31–0.35	0.75–1.5
Broad	92–200	500–800	0.1–1	0–2

TABLE 6.1. Parameters of antichirp signal searched over. 'Narrow' matches the signal reported by vP-DV, while 'Broad' is over a range of similar waveforms

In addition to searching for this specific signal, we also searched for general narrowband signals by searching over Bézier curves in the same timescale. Neither study found evidence of any signal following GW170817.

6.3.1. Setting Upper Limits

The purported signal discovered by vP-DV had an energy of 0.002 $M_{\odot}c^2$ assuming a distance of 40 Mpc. Calculations of an ideal matched filter indicate that such a weak signal is not detectable using any means; even when using the optimal matched filter and setting a lower threshold for detection, the lowest amount of energy that could possibly be detected is 0.015 $M_{\odot}c^2$ [80]. Given that vP-DV's model does not provide an exact waveform with which one could perform a matched filter search, even this limit is impossible to reach. He does, however, give enough information for us to calculate an upper limit on the predicted emission using STAMP.

We produced injections that followed the signal morphology of the vP-DV waveform, adapting code provided by the authors of [80]. This model assumes GW emission from a quadrupole (as in Appendix A.1) whose characteristics aside from rotational velocity do not change. An example of such an injection added to LIGO data is shown in Figure 6.4.

To calculate upper limits, we follow the same procedure outline in Chapter V. We place upper limits on both the existence of any antichirping signal as well as the antichirp with the parameters reported in [79]. Since we injected only that waveform, the difference here is the threshold SNR: the loudest antichirping cluster in the on-source was found to be 4.32, so that is the threshold for the general antichirp. But the loudest antichirp cluster with the particular parameters

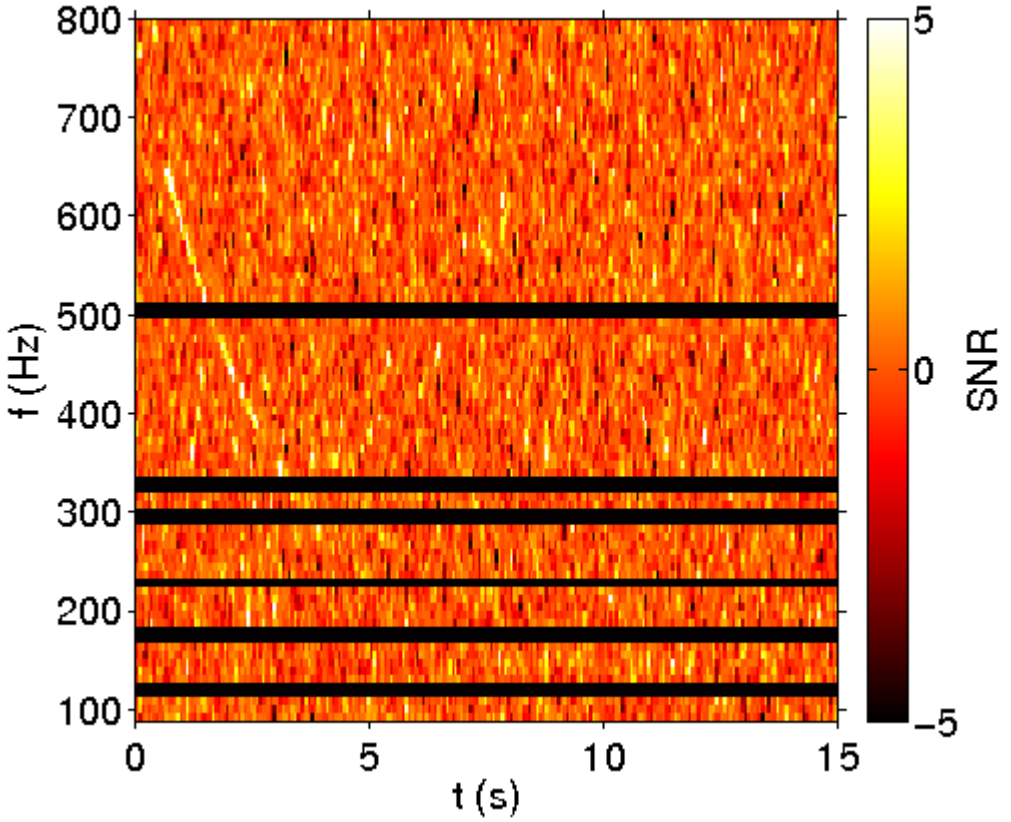

FIGURE 6.4. SNR time-frequency map, with 1/8 sec long pixels, of LIGO data with an antichirp injection added. The injection starts just before 1 second at 650 Hz.

from [79], was 1.70. The fact that this SNR is lower than the general case is a restatement of the principal finding: the signal purported by [79] is not recovered by this search.

The injection study finds that the minimum detectable energy for this search (at 50% recovery efficiency) is 4.1×10^{52} erg and 1.2×10^{53} erg for narrow and broad search parameters, respectively. In solar masses, this is 0.023 $M_{\odot}c^2$ and 0.0955 $M_{\odot}c^2$. As expected, these energies are both larger than the minimum energy detectable by an ideal matched filter search.

6.4. X-Pipeline with PCA

In the standard configuration of X-Pipeline (see Chapter V, for example), only the loudest few pixels are utilized. However, many waveforms have power spread across multiple frequencies, so the standard approach may throw away signal as well as noise. For such waveforms that are well-defined, a matched filtering approach is preferred. On the other hand, there are some waveform families that are not tightly constrained, yielding too many similar waveforms for a matched filter to be feasible. Thus a middle ground approach can bring better results. Post-merger signals from BNS systems fall into this category: as discussed above, there are a number of different models for predicting the resulting GW signal, but usually they require parameters that are currently unknown (such as the neutron star equation of state).

For this analysis, we first obtain a catalog of waveforms, made from a set of simulations. The spectrograms of the waveforms are decomposed, using principle component analysis, into basis spectrograms[3]. However, since the goal of this search is to find evidence for a signal (rather than source characterization), we only keep the first principle component. This component will be shared by all waveforms in the catalog. Later components would be able to differentiate between waveforms, but that task only matters once a detection is confirmed.

We then use X-Pipeline to convolve this principle component spectrogram over the time-frequency map, reporting the time and peak frequency at which they have the greatest overlap. An example of an injected signal compared with the principle component spectrogram is shown in Figure 6.5.

[3]Each input waveform has a well-defined peak frequency. Before deconomposition, each waveform is aligned to the same peak frequency. During the search, this value is varied.

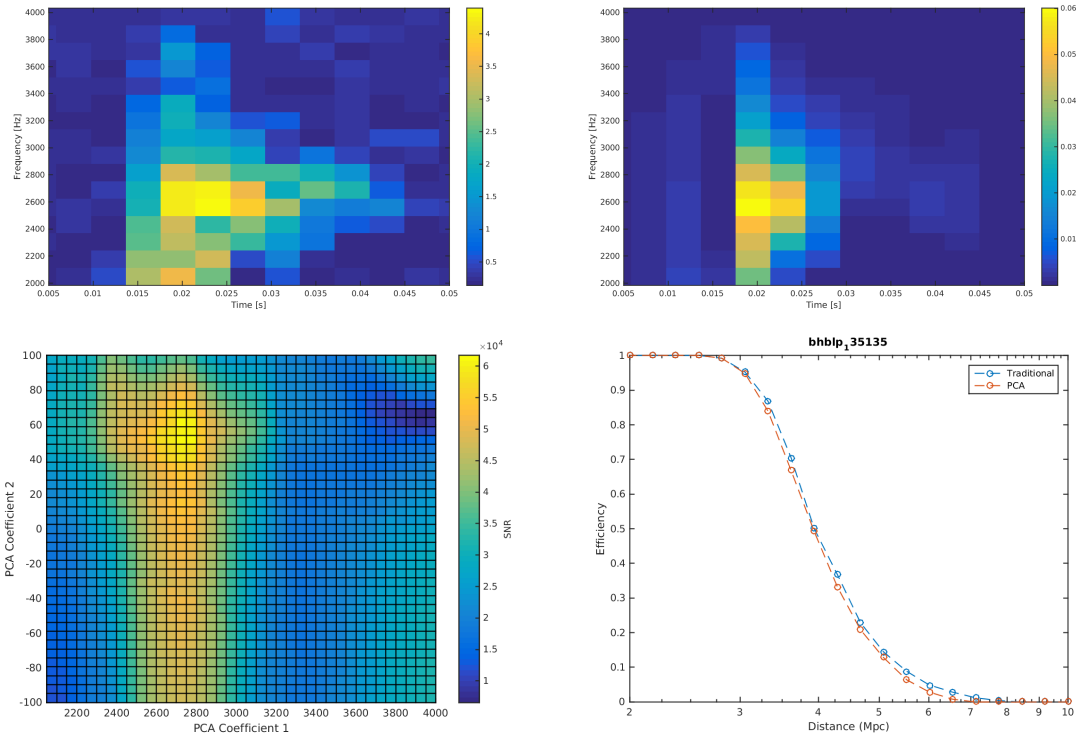

FIGURE 6.5. Injected signal (upper left), compared to the signal reconstructed using the PCA method (upper right). This signal was constructed with the BHBLP equation of state. The lower left plot shows how the SNR recovered depends on the central frequency and the first PCA component. In the lower right, we compare the sensitivity of the PCA search to traditional X-Pipeline

The performance of this method varies slightly with different models, usually performing slightly better than traditional X-Pipeline. Some waveforms do not match the first principle component as well (e.g., the waveform shown in Figure 6.5). Though the reconstruction does not match the signal as well as the signal in Figure 6.6, the PCA algorithm performs very well on it.

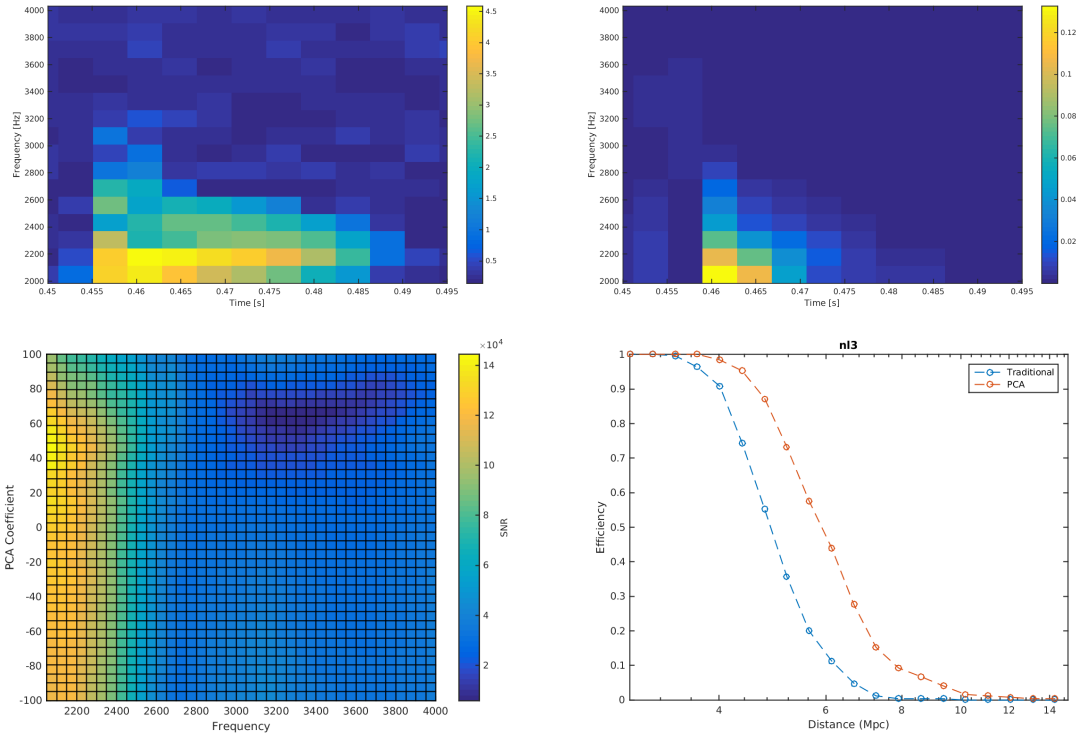

FIGURE 6.6. Same plots as in Figure 6.5 for the NL3 EoS.

Future work will extend the search to include more PCA components. Using templates that adhere more closely to the actual signal will boost SNR, though the additional degree of freedom may increase the background as well. The additional computational resources needed may require a coarser-grained search over PCA parameters, which would could also limit sensitivity.

CHAPTER VII

CONCLUSION

In the study of neutron stars, gravitational waves are invaluable. Analyses of GW170817 have already constrained models of the neutron star equation of state, verified theories about r-process nucleosynthesis, and contributed to our understanding of cosmology through estimates of neutron star binary populations and measurement of the Hubble parameter [20].

Gravitational waves from isolated neutron stars may be next. Though of much lower energy, signals from isolated neutron stars will be extremely informative. Current observations of neutron stars are limited to the electromagnetic spectrum, leaving the interior inaccessible to direct measurement. Gravitational waves have no such limitation. Any oscillations, provided that they are not axially symmetric, produce gravitational radiation which cannot be absorbed in the way light can.

The greatest challenge at the present is the detection of GWs. Even the strongest sources from the most cataclysmic processes result in only the tiniest of ripples in spacetime. To detect any GWs at all required a herculean effort by many scientists over many years. This dissertation covered a few more steps toward better gravitational wave astronomy.

7.1. The Search

The searches described here concern neutron stars, emitting gravitational radiation through three very different mechanisms. First, we explored GWs from isolated galactic magnetars, produced in conjunction with the transient bursting

activity characteristic of SGRs. Because of the uncertainty in the mechanism and mechanics of SGR bursts, we cast a broad net and used two separate analysis pipelines: X-Pipeline, designed for short-duration signals, and STAMP, targeted to intermediate-duration ones. Though no signal was detected, this search placed new limits on the GW power associated with those bursts.

Second, we showed that GW170817, caused by the merger of two neutron stars, can be found with an adaptation of the STAMP search. Analyses specifically designed for BNS signals produced better recoveries, but this analysis reinforces the flexibility and reliability of STAMP.

Finally, we examined the possibility of a post-merger signal from the object leftover after GW170817, and discussed the development of a new semi-modeled search for these GWs. Here we relied on principle component analysis to extract characteristics that multiple numerical models had in common. The technique offers improvement over currently-used methods.

7.2. Looking to the Future

It is currently an exciting time for LIGO, gravitational wave astronomy, and more broadly, time-domain astronomy. Strain sensitivity will soon reach a level where detections are routine, and new gravitational wave sources may be just around the corner. As more GW detectors operate for more and more time at greater and greater sensitivities, more secrets of the universe will be unlocked. Magnetar giant flares, galactic supernovae,a and other rare phenomena will be studied in great detail with GWs.

Sir Isaac Newton famously said "If I have seen further it is by standing on the shoulders of Giants." Nowhere is this more evident than in gravitational-

wave astronomy. All of the work in this dissertation was only possible because of contributions to the field from thousands of people: from the origins of the field to the construction of the instruments and software tools and many thankless tasks. It is my hope that this work will allow others to see a little further.

APPENDIX

OTHER DERIVATIONS

A.1. GW emission from a quadrupole

Consider the case of a rotating system where all mass is confined to a single axis, e.g. a rotating rod or a binary star system. Assuming the system rotates in the $x-y$ plane and defining $t=0$ as a time when all mass is lined up along the x-axis, the quadrupole moment tensor is:

$$I_{jk} = I \begin{bmatrix} \cos^2(\omega t) & \sin(\omega t)\cos(\omega t) & 0 \\ \sin(\omega t)\cos(\omega t) & \sin^2(\omega t) & 0 \\ 0 & 0 & 0 \end{bmatrix} \tag{A.1}$$

where the system is rotating with frequency ω, and I is the moment of inertia for the system. For an observer whose line of sight to the source forms angle ι with the source's z-axis, the transverse traceless part of this is:

$$I^{TT}_{jk} = P_{jl} I_{lm} P_{mk} - \frac{1}{2} P_{jk}\big(P_{lm} I_{ml}\big) \tag{A.2}$$

where $P_{jk} = \delta_{jk} - n_l n_m$ is the projection operator when n_m is the unit vector pointing from the observer to the source. Confining our observer to $y=0$ for simplicity, $n_m = (-\sin\iota, 0, \cos\iota)$, so the projection operator is:

$$P_{jk} = \begin{bmatrix} \cos^2\iota & 0 & \cos\iota\sin\iota \\ 0 & 1 & 0 \\ \cos\iota\sin\iota & 0 & \sin\iota \end{bmatrix} \tag{A.3}$$

So then,

$$
\begin{aligned}
P_{jk}I_{kl} =& I \begin{bmatrix} \cos^2\iota & 0 & \cos\iota\sin\iota \\ 0 & 1 & 0 \\ \cos\iota\sin\iota & 0 & \sin^2\iota \end{bmatrix} \begin{bmatrix} \cos^2\omega t & \sin\omega t\cos\omega t & 0 \\ \sin\omega t\cos\omega t & \sin^2\omega t & 0 \\ 0 & 0 & 0 \end{bmatrix} \\
=& I \begin{bmatrix} \cos^2\iota\cos^2\omega t & \cos^2\iota\cos\omega t\sin\omega t & 0 \\ \sin\omega t\cos\omega t & \sin^2\omega t & 0 \\ \cos\iota\sin\iota\cos^2\omega t & \cos\iota\sin\iota\sin\omega t\cos\omega t & 0 \end{bmatrix}
\end{aligned}
\tag{A.4}
$$

Thus $P_{lm}I_{ml} = I\big(\cos^2\iota\cos^2\omega t + \sin^2\omega t\big)$. And,

$$
P_{jl}I_{lm}P_{mk} = Mr^2 \begin{bmatrix} \cos^4\iota\cos^2(\omega t) & \cos^2\iota\cos(\omega t)\sin(\omega t) & \sin\iota\cos^3\iota\cos^2\omega t \\ \cos^2\iota\sin(\omega t)\cos(\omega t) & \sin^2(\omega t) & \sin\iota\cos\iota\sin\omega t\cos\omega t \\ \cos^3\iota\sin\iota\cos^2(\omega t) & \cos\iota\sin\iota\sin(\omega t)\cos(\omega t) & \cos^2\iota\sin^2\iota\cos^2\omega t \end{bmatrix}
\tag{A.5}
$$

The other term is:

$$
-\frac{1}{2}P_{jk}\big(P_{lm}I_{ml}\big) = -\frac{1}{2}\Big(\cos^2\iota\cos^2(\omega t) + \sin^2(\omega t)\Big) \begin{bmatrix} \cos^2\iota & 0 & \cos\iota\sin\iota \\ 0 & 1 & 0 \\ \cos\iota\sin\iota & 0 & \sin^2\iota \end{bmatrix}
\tag{A.6}
$$

Then we calculate I^{TT}, and rotate it with the rotation matrix:

$$
R = \begin{bmatrix} \cos\iota & 0 & -\sin\iota \\ 0 & 1 & 0 \\ \sin\iota & 0 & \cos\iota \end{bmatrix}
\tag{A.7}
$$

After doing all of that math, we find that $h_+ = \text{stuff} * \frac{1}{2}\big(1 + \cos^2\iota\big)$ and $h_\times = \text{stuff} * \cos\iota$. With an assist from Mathematica, we find:

$$\begin{aligned} h_{jk}^{TT} =& \frac{2}{r}\frac{G}{c^4}\ddot{I}_{jk}^{TT} \\ =& \frac{2}{r}\frac{G}{c^4}\frac{d^2}{dt^2}\Big[R^{-1}\Big(P_{jl}I_{lm}P_{mk} - \frac{1}{2}P_{jk}\big(P_{lm}I_{ml}\big)\Big)R\Big] \\ =& \frac{8G}{c^4}\frac{I\omega^2}{2}\frac{1}{r}\begin{bmatrix} \frac{1}{2}\cos(2\omega t)\big(1+\cos^2\iota\big) & \sin(2\omega t)\cos\iota & 0 \\ \sin(2\omega t)\cos\iota & -\frac{1}{2}\cos(2\omega t)\big(1+\cos^2\iota\big) & 0 \\ 0 & 0 & 0 \end{bmatrix} \end{aligned} \tag{A.8}$$

In the last line, we have divided up the prefactor into groups to show the logic of the equation: the physical constants, rotational energy, and the factor of $\frac{1}{r}$ which shows that this is radiation. Note that this equation is only true for the quadrupole tensor outlined above, and does not hold when there is additional spherical symmetry (for example, a rotating neutron star with a mountain).

REFERENCES CITED

[1] Ryan Quitzow-James et al. Exploring a search for long-duration transient gravitational waves associated with magnetar bursts. *Classical and Quantum Gravity*, 34(16):164002, 2017. URL http://stacks.iop.org/0264-9381/34/i=16/a=164002.

[2] S. A. Olausen and V. M. Kaspi. The McGill magnetar catalog. *The Astrophysical Journal Supplement Series*, 212(1):6, 2014. URL http://stacks.iop.org/0067-0049/212/i=1/a=6.

[3] J. H. Taylor and J. M. Weisberg. A new test of general relativity - Gravitational radiation and the binary pulsar PSR 1913+16. *The Astrophysical Journal*, 253:908–920, February 1982. doi: 10.1086/159690.

[4] Kip S Thorne. Gravitational-wave research: Current status and future prospects. *Reviews of Modern Physics*, 52(2):285, 1980.

[5] R. Kafka and L. Schnupp. Final Result of the Munich-Frascati Gravitational Radiation Experiment. , 70:97, November 1978.

[6] Barry C Barish and Rainer Weiss. Ligo and the detection of gravitational waves. *Physics Today*, 52:44–50, 1999.

[7] J Aasi et al. Advanced LIGO. *Classical and Quantum Gravity*, 32(7):074001, 2015. URL http://stacks.iop.org/0264-9381/32/i=7/a=074001.

[8] Abbott, B. P. et al. GW170817: Observation of gravitational waves from a binary neutron star inspiral. *Phys. Rev. Lett.*, 119:161101, Oct 2017. doi: 10.1103/PhysRevLett.119.161101. URL https://link.aps.org/doi/10.1103/PhysRevLett.119.161101.

[9] Charles W. Misner, Kip S. Thorne, and John Archibald Wheeler. *Gravitation*. W. H. Freeman, 1973. ISBN 0-7167-0344-0.

[10] Robert M. Wald. *General Relativity*. The University of Chicago Press, 1984. ISBN 0-226-87033-2.

[11] Shuang Liang and Yi Xie. New upper limit on the cosmological constant from solar system dynamics. *Research in Astronomy and Astrophysics*, 14(5):527, 2014. URL http://stacks.iop.org/1674-4527/14/i=5/a=003.

[12] Bernard Schutz. *A First Course in General Relativity*. Cambridge University Press, 2 edition, 2009. doi: 10.1017/CBO9780511984181.

[13] Miriam Cabero, Andrew Lundgren, Alex H. Nitz, Thomas Dent, David Barker, Evan Goetz, Jeff S. Kissel, Laura K. Nuttall, Paul Schale, Robert Schofield, and Derek Davis. Blip glitches in Advanced LIGO data. *arXiv e-prints*, art. arXiv:1901.05093, Jan 2019.

[14] B P Abbott et al. Effects of data quality vetoes on a search for compact binary coalescences in Advanced LIGO's first observing run. *Classical and Quantum Gravity*, 35(6):065010, 2018. URL `http://stacks.iop.org/0264-9381/35/i=6/a=065010`.

[15] M Rakhmanov, J D Romano, and J T Whelan. High-frequency corrections to the detector response and their effect on searches for gravitational waves. *Classical and Quantum Gravity*, 25(18):184017, 2008. URL `http://stacks.iop.org/0264-9381/25/i=18/a=184017`.

[16] Joseph H. Taylor and J. M. Weisberg. Further experimental tests of relativistic gravity using the binary pulsar PSR 1913+16. *The Astrophysical Journal*, 345:434–450, 1989. doi: 10.1086/167917.

[17] Abbott, B. P. et al. Observation of gravitational waves from a binary black hole merger. *Phys. Rev. Lett.*, 116:061102, Feb 2016. doi: 10.1103/PhysRevLett.116.061102. URL `https://link.aps.org/doi/10.1103/PhysRevLett.116.061102`.

[18] B. P. Abbott et al. GWTC-1: A Gravitational-Wave Transient Catalog of Compact Binary Mergers Observed by LIGO and Virgo during the First and Second Observing Runs. *arXiv e-prints*, art. arXiv:1811.12907, Nov 2018.

[19] A. Goldstein et al. An ordinary short gamma-ray burst with extraordinary implications: Fermi-GBM detection of GRB 170817A. *The Astrophysical Journal Letters*, 848(2):L14, 2017. URL `http://stacks.iop.org/2041-8205/848/i=2/a=L14`.

[20] Abbott, B. P. et al. A gravitational-wave standard siren measurement of the Hubble constant. *Nature*, 551(7678):85–88, 2017.

[21] Barry Freedman and Larry McLerran. Quark star phenomenology. *Physical Review D*, 17(4):1109, 1978.

[22] Jeremy J Drake et al. Is RX J1856.5–3754 a quark star? *The Astrophysical Journal*, 572(2):996, 2002.

[23] JE Trümper et al. The puzzles of RX J1856.5–3754: neutron star or quark star? *Nuclear Physics B-Proceedings Supplements*, 132:560–565, 2004.

[24] F Curtis Michel. *Theory of neutron star magnetospheres*. University of Chicago Press, 1991.

[25] Sandro Mereghetti, José A. Pons, and Andrew Melatos. Magnetars: Properties, origin and evolution. *Space Science Reviews*, 191(1):315–338, Oct 2015. ISSN 1572-9672. doi: 10.1007/s11214-015-0146-y. URL https://doi.org/10.1007/s11214-015-0146-y.

[26] V. M. Kaspi et al. A major soft gamma repeater-like outburst and rotation glitch in the no-longer-so-anomalous x-ray pulsar 1E 2259+586. *The Astrophysical Journal*, 588(2):L93–L96, apr 2003. doi: 10.1086/375683. URL https://doi.org/10.1086%2F375683.

[27] Chryssa Kouveliotou et al. An x-ray pulsar with a superstrong magnetic field in the soft γ-ray repeater SGR 1806–20. *Nature*, 393(6682):235, 1998.

[28] P. Esposito, N. Rea, and G. L. Israel. Magnetars: a short review and some sparse considerations. *arXiv Preprint*, 2018. URL https://arxiv.org/abs/1803.05716.

[29] N Rea et al. A low-magnetic-field soft gamma repeater. *Science*, page 1196088, 2010.

[30] Sinem Şaşmaz Muş et al. A glitch and an anti-glitch in the anomalous x-ray pulsar 1e 1841–045. *Monthly Notices of the Royal Astronomical Society*, 440 (4):2916–2921, 2014.

[31] Robert F Archibald et al. An anti-glitch in a magnetar. *Nature*, 497(7451):591, 2013.

[32] Sandro Mereghetti. The strongest cosmic magnets: soft gamma-ray repeaters and anomalous x-ray pulsars. *The Astronomy and Astrophysics Review*, 15(4): 225–287, 2008.

[33] Christopher Thompson and Robert C Duncan. The soft gamma repeaters as very strongly magnetized neutron stars-i. radiative mechanism for outbursts. *Monthly Notices of the Royal Astronomical Society*, 275(2):255–300, 1995.

[34] Christopher Thompson, Huan Yang, and Néstor Ortiz. Global crustal dynamics of magnetars in relation to their bright x-ray outbursts. *The Astrophysical Journal*, 841(1):54, may 2017. doi: 10.3847/1538-4357/aa6c30. URL https://doi.org/10.3847%2F1538-4357%2Faa6c30.

[35] E. O. Ofek et al. The short-hard GRB051103: Observations and implications for its nature. *The Astrophysical Journal*, 652(1):507, 2006. URL http://stacks.iop.org/0004-637X/652/i=1/a=507.

[36] Hurley, K et al. An exceptionally bright flare from SGR 1806–20 and the origins of short-duration γ-ray bursts. *Nature*, 434(7037):1098, 2005.

[37] S. Mereghetti et al. STRONG BURSTS FROM THE ANOMALOUS x-RAY PULSAR 1e 1547.0–5408 OBSERVED WITH THEINTEGRAL/SPI ANTI-COINCIDENCE SHIELD. *The Astrophysical Journal*, 696(1):L74–L78, apr 2009. doi: 10.1088/0004-637x/696/1/l74. URL https://doi.org/10.1088%2F0004-637x%2F696%2F1%2Fl74.

[38] P. M. Woods et al. Changes in the x-ray emission from the magnetar candidate 1*e* 2259+586 during its 2002 outburst. *The Astrophysical Journal*, 605(1): 378–399, apr 2004. doi: 10.1086/382233. URL https://doi.org/10.1086%2F382233.

[39] Alaa I. Ibrahim et al. Discovery of a transient magnetar: XTE J1810–197. *The Astrophysical Journal*, 609(1):L21–L24, may 2004. doi: 10.1086/422636. URL https://doi.org/10.1086%2F422636.

[40] G. L. Israel et al. The discovery of rapid x-ray oscillations in the tail of the SGR 1806–20 hyperflare. *The Astrophysical Journal Letters*, 628(1):L53, 2005. URL http://stacks.iop.org/1538-4357/628/i=1/a=L53.

[41] Tod E. Strohmayer and Anna L. Watts. Discovery of fast x-ray oscillations during the 1998 giant flare from SGR 1900+14. *The Astrophysical Journal Letters*, 632(2):L111, 2005. URL http://stacks.iop.org/1538-4357/632/i=2/a=L111.

[42] D. Huppenkothen et al. Quasi-periodic oscillations in short recurring bursts of the soft gamma repeater J15505418. *The Astrophysical Journal*, 787(2):128, 2014. URL http://stacks.iop.org/0004-637X/787/i=2/a=128.

[43] D. Huppenkothen, L. M. Heil, A. L. Watts, and E. G. Quasi-periodic oscillations in short recurring bursts of magnetars SGR 180620 and SGR 1900+14 observed with rxte. *The Astrophysical Journal*, 795(2):114, 2014. URL http://stacks.iop.org/0004-637X/795/i=2/a=114.

[44] Alessandra Corsi and Benjamin J Owen. Maximum gravitational-wave energy emissible in magnetar flares. *Physical Review D*, 83(10):104014, 2011.

[45] Y. Levin and M. van Hoven. On the excitation of f modes and torsional modes by magnetar giant flares. *Monthly Notices of the Royal Astronomical Society*, 418:659–663, November 2011. doi: 10.1111/j.1365-2966.2011.19515.x.

[46] B. Zink, P. D. Lasky, and K. D. Kokkotas. Are gravitational waves from giant magnetar flares observable? *Physical Review D*, 85(2):024030, January 2012. doi: 10.1103/PhysRevD.85.024030.

[47] P. M. Woods et al. The prelude to and aftermath of the giant flare of 2004 December 27: Persistent and pulsed x-ray properties of SGR 1806-20 from 1993 to 2005. *The Astrophysical Journal*, 654(1):470, 2007. URL http://stacks.iop.org/0004-637X/654/i=1/a=470.

[48] David M. Palmer. Personal Communication, June 7, 2017.

[49] B. P. Abbott et al. Search for transient gravitational-wave signals associated with magnetar bursts during Advanced LIGO's second observing run. *The Astrophysical Journal*, 874(2):163, April 2019. doi: 10.3847/1538-4357/ab0e15. URL https://doi.org/10.3847%2F1538-4357%2Fab0e15.

[50] F Acernese et al. Advanced Virgo: a second-generation interferometric gravitational wave detector. *Classical and Quantum Gravity*, 32(2):024001, 2015. URL http://stacks.iop.org/0264-9381/32/i=2/a=024001.

[51] B. S. Sathyaprakash and Bernard F. Schutz. Physics, astrophysics and cosmology with gravitational waves. *Living Reviews in Relativity*, 12(1):2, Mar 2009. ISSN 1433-8351. doi: 10.12942/lrr-2009-2. URL https://doi.org/10.12942/lrr-2009-2.

[52] Kunihito Ioka. Magnetic deformation of magnetars for the giant flares of the soft gamma-ray repeaters. *Monthly Notices of the Royal Astronomical Society*, 327(2):639–662, 2001.

[53] Ryan Quitzow-James. *Search for Long-Duration Transient Gravitational Waves Associated with Magnetar Bursts during LIGO's Sixth Science Run*. PhD thesis, University of Oregon, 2016. URL https://dcc.ligo.org/LIGO-P1600095/public.

[54] Sutton, Patrick J. et al. X-Pipeline: an analysis package for autonomous gravitational-wave burst searches. *New Journal of Physics*, 12(5):053034, 2010. URL http://stacks.iop.org/1367-2630/12/i=5/a=053034.

[55] Abbott, B. P. et al. Search for gravitational waves associated with gamma-ray bursts during the first Advanced LIGO observing run and implications for the origin of GRB 150906B. *The Astrophysical Journal*, 841(2):89, 2017. URL http://stacks.iop.org/0004-637X/841/i=2/a=89.

[56] B. Abbott et al. Search for gravitational wave radiation associated with the pulsating tail of the SGR $1806-20$ hyperflare of 27 december 2004 using LIGO. *Phys. Rev. D*, 76:062003, Sep 2007. doi: 10.1103/PhysRevD.76.062003. URL https://link.aps.org/doi/10.1103/PhysRevD.76.062003.

[57] Abadie, J. et al. Search for gravitational wave bursts from six magnetars. *The Astrophysical Journal Letters*, 734(2):L35, 2011. URL http://stacks.iop.org/2041-8205/734/i=2/a=L35.

[58] B. P. Abbott, R. Abbott, R. Adhikari, P. Ajith, B. Allen, et al. Stacked search for gravitational waves from the 2006 sgr 1900+14 storm. *The Astrophysical Journal Letters*, 701(2):L68, 2009. URL http://stacks.iop.org/1538-4357/701/i=2/a=L68.

[59] B. P. Abbott, R. Abbott, R. Adhikari, P. Ajith, B. Allen, et al. Search for Gravitational-Wave Bursts from Soft Gamma Repeaters. *Phys. Rev. Lett.*, 101:211102, Nov 2008. doi: 10.1103/PhysRevLett.101.211102. URL https://link.aps.org/doi/10.1103/PhysRevLett.101.211102.

[60] E Thrane, S Kandhasamy, C D Ott, et al. Long gravitational-wave transients and associated detection strategies for a network of terrestrial interferometers. *Physical Review D*, 83:083004, 2011.

[61] Eric Thrane and Michael Coughlin. Searching for gravitational-wave transients with a qualitative signal model: Seedless clustering strategies. *Physical Review D*, 88, 08 2013. doi: 10.1103/PhysRevD.88.083010.

[62] Eric Thrane and Michael Coughlin. Seedless clustering in all-sky searches for gravitational-wave transients. *Phys. Rev.*, D89(6):063012, 2014. doi: 10.1103/PhysRevD.89.063012.

[63] Michael Coughlin, Patrick Meyers, Shivaraj Kandhasamy, Eric Thrane, and N. Christensen. Prospects for searches for long-duration gravitational-waves without time slides. *Phys. Rev. D*, 92:043007, Aug 2015. doi: 10.1103/PhysRevD.92.043007. URL https://link.aps.org/doi/10.1103/PhysRevD.92.043007.

[64] S. L. Detweiler. A variational calculation of the fundamental frequencies of quadrupole pulsation of fluid spheres in general relativity. *The Astrophysical Journal*, 197:203–217, 03 1975. doi: 10.1086/153504.

[65] Nils Andersson and Kostas D Kokkotas. Towards gravitational wave asteroseismology. *Monthly Notices of the Royal Astronomical Society*, 299(4): 1059–1068, 1998.

[66] Neil J Cornish and Tyson B Littenberg. Bayeswave: Bayesian inference for gravitational wave bursts and instrument glitches. *Classical and Quantum Gravity*, 32(13):135012, June 2015. doi: 10.1088/0264-9381/32/13/135012. URL https://doi.org/10.1088%2F0264-9381%2F32%2F13%2F135012.

[67] BP Abbott, R Abbott, TD Abbott, F Acernese, K Ackley, C Adams, T Adams, P Addesso, RX Adhikari, VB Adya, et al. Gw170817: Measurements of neutron star radii and equation of state. *arXiv preprint arXiv:1805.11581*, 2018.

[68] P. B. Demorest et al. A two-solar-mass neutron star measured using Shapiro delay. *Nature*, 467:1081–1083, October 2010. doi: 10.1038/nature09466.

[69] Manuel Linares, Tariq Shahbaz, and Jorge Casares. Peering into the dark side: magnesium lines establish a massive neutron star in PSR J2215+5135. *The Astrophysical Journal*, 859(1):54, 2018.

[70] Ben Margalit and Brian D Metzger. Constraining the maximum mass of neutron stars from multi-messenger observations of gw170817. *The Astrophysical Journal Letters*, 850(2):L19, 2017.

[71] Brian D. Metzger. Kilonovae. *Living Reviews in Relativity*, 20(1):3, May 2017. ISSN 1433-8351. doi: 10.1007/s41114-017-0006-z. URL `https://doi.org/10.1007/s41114-017-0006-z`.

[72] M. Nicholl et al. The electromagnetic counterpart of the binary neutron star merger LIGO/virgo GW170817. III. optical and UV spectra of a blue kilonova from fast polar ejecta. *The Astrophysical Journal*, 848(2):L18, oct 2017. doi: 10.3847/2041-8213/aa9029. URL `https://doi.org/10.3847%2F2041-8213%2Faa9029`.

[73] R. Chornock et al. The electromagnetic counterpart of the binary neutron star merger LIGO/virgo GW170817. IV. detection of near-infrared signatures of r-process nucleosynthesis with gemini-south. *The Astrophysical Journal*, 848 (2):L19, oct 2017. doi: 10.3847/2041-8213/aa905c. URL `https://doi.org/10.3847%2F2041-8213%2Faa905c`.

[74] G. A. Wynn, P. T. O'Brien, and B. P. Gompertz. Magnetar powered GRBs: explaining the extended emission and X-ray plateau of short GRB light curves. *Monthly Notices of the Royal Astronomical Society*, 438(1):240–250, 12 2013. ISSN 0035-8711. doi: 10.1093/mnras/stt2165. URL `https://doi.org/10.1093/mnras/stt2165`.

[75] Feryal Özel and Paulo Freire. Masses, radii, and the equation of state of neutron stars. *Annual Review of Astronomy and Astrophysics*, 54:401–440, 2016.

[76] Hou-Jun Lü, Bing Zhang, Wei-Hua Lei, Ye Li, and Paul D Lasky. The millisecond magnetar central engine in short grbs. *The Astrophysical Journal*, 805(2):89, 2015.

[77] Vikram Ravi and Paul D Lasky. The birth of black holes: neutron star collapse times, gamma-ray bursts and fast radio bursts. *Monthly Notices of the Royal Astronomical Society*, 441(3):2433–2439, 2014.

[78] B. P. Abbott et al. Search for post-merger gravitational waves from the remnant of the binary neutron star merger GW170817. *The Astrophysical Journal*, 851(1):L16, dec 2017. doi: 10.3847/2041-8213/aa9a35. URL `https://doi.org/10.3847%2F2041-8213%2Faa9a35`.

[79] Maurice HPM van Putten and Massimo Della Valle. Observational evidence for extended emission to gw170817. *Monthly Notices of the Royal Astronomical Society: Letters*, 482(1):L46–L49, 2018.

[80] Miquel Oliver et al. Matched-filter study and energy budget suggest no detectable gravitational-wave'extended emission'from gw170817. *arXiv preprint arXiv:1812.06724*, 2018.